Diffusion Controlled Processes in Amorphous Si-C-N and Related Materials

Habilitationsschrift
zur Erlangung der venia legendi für das Fachgebiet

Materialphysik

Fakultät für Natur- und Materialwissenschaften
der Technischen Universität Clausthal

vorgelegt von

Dr. rer. nat.
Harald Schmidt

aus Hof/Saale

Juni 2005

Für ASTRID und GREGOR

List of Abbreviations

CVD	Chemical Vapour Deposition
EDX	Energy Dispersive X-ray Analysis
FTIR	Fourier Transform Infrared Spectroscopy
JMAK	Johnson-Mehl-Avrami-Kolmogorov
LSW	Lifshitz-Sylozov-Wagner
n-RBS	Non-Rutherford Backscattering Spectrometry
NRRA	Nuclear Resonant Reaction Analysis
PAS	Positron Annihilation Spectroscopy
PECVD	Plasma Enhanced Chemical Vapour Deposition
SAED	Selected Area Electron Diffraction
SIMS	Secondary Ion Mass Spectrometry
SNMS	Secondary Neutral Mass Spectrometry
SRIM	Stopping and Range of Ions in Matter
TEM	Transmission Electron Microscopy
XRD	X-ray Diffractometry

Abstract

The thermal stability, the microstructure formation, and the long term durability of high temperature materials of the system Si-C-N depend sensitively on diffusion controlled atomic re-arrangement processes. In this study, experimental investigations were carried out on that topic in various polymer-derived bulk ceramics (precursor ceramics) and magnetron sputtered films at high temperatures (up to 1900 °C). The results are described by phenomenological models and numerical calculations, which enabled to understand these processes on a fundamental level and to obtain process parameters in order to tailor multi-component composite materials.

The first part of this work deals with the investigation of self-diffusion in amorphous Si-(B-)C-N precursor ceramics and Si_3N_4 films, using stable isotopes, and Secondary Ion (Neutral) Mass Spectrometry and Resonant Nuclear Reaction Analysis. High dose ion implantation, isotope exchange from the gas phase, and isotope heterostructures were applied in order to obtain self-diffusivities in these complex materials where conventional methods of tracer deposition are not successful. The determined low self-diffusivities (about 10^{-18} m^2/s at 1700 °C) are in the same order of magnitude for different materials, different thermodynamic states, and for the major constituents. A thermally activated migration of atoms via point defects and high activation enthalpies of about 5 to 7 eV are observed in the amorphous and crystalline state. Possible diffusion mechanisms are discussed and the results are compared to other categories of materials (metals, semiconductors, metallic glasses, silicates).

A second central theme of the present thesis is the characterization of hydrogen motion in amorphous Si-(B-)C-N, SiC, and Si_3N_4 as a function of composition, hydrogen content, and thermodynamic state. Hydrogen is present in these materials up to 1000 °C in the percent range and is important for the compensation of electronic defects and for stress relaxation. A wide range of activation enthalpies (0.3 - 4 eV) and pre-exponential factors (10^{-14} - 10^{-2} m^2/s) are found to obey a compensation law, which can be explained with a model based on a temperature dependent hydrogen chemical potential and on the temporary trapping of diffusing hydrogen atoms at Si, C, and N dangling bonds.

In the final part of the work, the formation kinetics of SiC/Si_3N_4 nano-composites from an amorphous Si-(B-)C-N matrix is studied by X-ray Diffractometry and additional Transmission Electron Microscopy. It is shown that crystalline phase formation is governed by several superimposed processes, which are: crystallization, mediated by nucleation and diffusional growth, a special solid state reaction, and diffusion controlled coarsening. The data are modelled on the basis of the underlying diffusion processes and the reasons for the enormous thermal stability of these materials are discussed. The results are compared to sputtered SiC and Si_3N_4 films, where an interface-reaction controlled transformation from amorphous to crystalline state was found to be also strongly influenced by the self-diffusion properties. Tremendous differences occur for the thermal stability and the crystallization behaviour of SiC films deposited on different substrates, which are explained by a point defect-mediated growth process and defect equilibration between film and substrate.

1. Introduction

One of the tasks of modern materials science is the development of advanced materials, which can be used at high temperatures up to 2000 °C (ultra high temperature stable materials). Basic requirements for such materials, which may become interesting for industrial objectives, are a low density, a high melting or dissociation temperature, a good thermal shock resistance, a good oxidation behaviour, interesting mechanical properties, and of course tuneable functional properties like e.g. electrical conductivity. During the last years, a growing research interest is devoted to non-oxide materials of the system Si-C-N, which show such favourable properties. Here, bulk materials as well as coatings and thin films are of interest. Two stable binary crystalline compounds are known in this system, silicon carbide (SiC) and silicon nitride (Si_3N_4), which can be produced by conventional sintering or hot pressing of powders, and which were extensively studied during the last decades [Ril00, Ham94, Kom94, Sch94]. Since the 1970's a high interest exists also in amorphous and crystalline films as part of electronic or optoelectronic components or surface coatings. In addition, efforts were made to combine the properties of both types of materials by synthesizing SiC_xN_y compounds in order to produce materials with optimised properties. Using chemical vapour deposition [Lav04, Ben97, Che96, Gom96, Bad98], reactive magnetron sputtering [Lut98, Lut01, Kom90, Xia00, Lin02, Wu02], ion implantation [Lik99, Usl96], and laser deposition [Zeh94, Mac98, Par03] thin films in the nanometer or micrometer range, deposited on various types of substrates, can be realized. Applications as hard coatings [Bad98, Pen03, Che99, Vlc02], as tribological coatings [Ber01], and as optoelectronic wide band gap materials [Lav04, Bad98, Che98, Che99] are under discussion.

A relatively new synthesis route for high purity Si-C-N based compounds as bulk materials, powders, coatings, or fibres is the usage of organo-elemental precursors, which are transformed into inorganic materials by solid state thermolysis [Rie92, Ald98, Bil96, Bil99, Bil00, Zie99, Kro00, Wei01, Jan97]. The underlying aim of this processing route is to tailor ceramics on the basis of molecular units in order to control the structure and properties of such a material on an atomic scale. Especially, the incorporation of several atomic percent of boron and the formation of Si-B-C-N materials resulted in ultra high temperature stable ceramics with a dissociation temperature of about 2200 °C in inert gas [Bal94b, Bal97, Jan97, Rie96, Ald98, Kro00, Bil96, Bil01].

In general, all these materials are in a non-equilibrium, amorphous state after deposition or thermolysis. This enables the possibility to produce a wide range of amorphous/crystalline composite materials with a tailored microstructure by in-situ crystallization. The production of nano-composites in order to make materials with superior mechanical properties, like superplasticity, or with high strength and fracture toughness [Wak90] can be exemplarily quoted to show the enormous possibilities. In order to design such materials, an understanding and quantitative description of the microstructural changes governing phase formation have to be achieved on a fundamental level. All these processes

are controlled by the diffusion of the constituting elements. Thus, the knowledge of self-diffusivities and diffusion mechanisms in these materials is indispensable for an understanding of these processes.

A further possible application of theses amorphous systems might be found in optoelectronic devices with a tuneable band gap (e. g. thin film transistors [Rob94], light emitting diodes [Fot01, Lav04], or solar cells [Bul96, Gha99]) and as tuneable electrical conductors [Her01, Ali02, Tra02]. Here, the incorporation of hydrogen into the amorphous structure in order to form Si-C-N-H materials is of high importance. Since for polymer-derived Si-C-N, hydrogen is present in the per cent range after thermolysis, these materials are of interest for such applications. The thermal stability of hydrogen passivated dangling bonds plays a crucial role for the defect passivation of electronic defects and for stress relaxation in order to establish a homogeneous amorphous phase and thus to improve the quality of components. Especially, the connection between the migration of hydrogen and the interaction with dangling bonds is of high interest [Fot01]. As obvious from these remarks, the understanding of self-diffusion and of processes governed by this phenomenon are very essential for the synthesis, the functional properties, and the high temperature stability of Si-C-N based materials.

The self-diffusion in metals is relatively well understood due to an intense research on that topic during the last decades [Heu92, Meh90]. This statement is also true, however to a lesser extent, for intermetallic compounds [Meh90] and for oxides [Atk94]. In contrast, relatively little is known for non-oxide ceramic materials and semiconductors (Nitrides, Borides, Carbides [Lan98]), especially for complex multinary systems with high melting or dissociation temperatures, like the present Si-C-N materials. Here, the investigation of self-diffusion is connected with a variety of analytical problems: (1) for nearly all the constituting elements B, N, Si, C, and H no or no suitable radioactive tracers are available for the performance of extensive diffusion measurements. This fact prevents the use of the standard radiotracer technique, which is state-of-the-art in diffusivity determination in metals and intermetallics due to its high detection sensitivity [Meh90]. To circumvent this problem, it is necessary to use rare stable isotopes which decreases the detection sensitivity of the tracer. (2) Diffusion experiments have to be carried out at relatively high temperatures of 0.7 T_m (T_m: melting point) due to the low atomic motilities. This makes it necessary to work with specially designed furnace systems which reach at least 1700 °C in a controlled atmosphere at a defined partial pressure (N_2, Ar, H_2). (3) Due to the difficult commercial availability of sufficient quantities of tracer isotopes in a non-oxidized form, special methods, like ion implantation, sputter deposition, and gas exchange are necessary, which entail advanced requirements for the analytical equipment. (4) Surface oxidation may influence the tracer deposition and the diffusion process substantially, especially for long-time annealing. Consequently, the tracer has to be introduced beyond the sample surface, so that diffusion may take place in the interior of the sample. (5) The existence of very low diffusivities even at high temperatures, the geometry of thin films limited to the (sub-)micrometer range, and the metastability of the materials necessitates the application

of analytical methods with an excellent vertical depth resolution, like Secondary Ion Mass Spectrometry (SIMS), far beyond the lapping and grinding method normally used for serial sectioning. These problems lead to the fact that nearly no reliable self-diffusion data exist for Si-C-N or Si-N materials at present, neither for bulk materials nor for thin films. Consequently, the study presented here was launched to improve this situation. Starting from these introductory remarks, the main tasks of the present work are: (1) Investigation of (self-)diffusion of the elements B, C, N, Si, and also H, in Si-(B-)C-N materials and Si_3N_4, and identification of the diffusion mechanisms. (2) Investigation of the diffusion controlled formation kinetics of crystalline precipitations in a supersaturated amorphous Si-(B-)C-N matrix during high temperature annealing in order to form SiC/Si_3N_4 nano-composites. (3) Comparative study of the interface-reaction controlled crystallization of SiC and Si_3N_4. (4) Explanation of the kinetic processes appearing during phase formation on the basis of the self-diffusion data.

The work is organized in the following way: in section 2 the materials which were investigated during this study are presented. A brief description of the fundamental properties of polymer-derived Si-B-C-N ceramics and magnetron sputtered SiC and Si_3N_4 films is given. Experimental details on the synthesis of the materials, and on the analytical methods used, are described in section 3. The first self-diffusion experiments in amorphous Si-(B-)C-N carried out with ion implanted isotopes are presented in section 4. The application of isotope heterostructures for successful self-diffusivity determination in amorphous and crystalline Si_3N_4 is given in section 5. The experiments and numerical calculations concerning the trap-limited diffusion of hydrogen in Si-C-N based materials are discussed in section 6. In section 7, a detailed analysis on the kinetics of crystalline precipitate formation in amorphous Si-(B-)C-N is presented and, finally, in section 8 the polymorphous transformation from amorphous to polycrystalline state in SiC and Si_3N_4 is discussed. The work is closed with a summary and an appendix.

2. Si-C-N and Related Materials

2.1. Polymer-Derived Si-(B-)C-N Ceramics

During the last years a growing research interest has been given to inorganic materials synthesized from pre-ceramic polymers (precursor ceramics). Especially, ceramics of the systems Si-C-N [Rie92, Bil98, Zie99, Bil00] and Si-B-C-N [Bil96, Bil01, Rie96, Jan97, Ald98, Mul00, Mul01] are attractive because of their high temperature stability (up to 2200 °C) [Rie96, Bil96, Jan97, Mul01], their good oxidation resistance [Raj98, Bha04, But00, But01], their mechanical properties [Rie98, An98, Chr00, Chr01a, Chr01b, Bau01, Zim02], and their electrical properties [Her01, Tra02]. Annealing of these amorphous materials at high temperatures in an inert atmosphere leads to complete or partial crystallization of silicon carbide and silicon nitride, yielding different types of nano-composites. Si-(B-)C-N materials are produced by the conversion of organo-elemental precursors (polymers) into inorganic ceramics by a complex transformation process which is illustrated in section 3.1.

The main characteristics of precursor-derived materials are:

- It is possible to design metastable amorphous materials as well as novel composite materials and multinary ceramics which are not available by conventional technologies [Bil96].
- Nearly impurity free material with a homogeneous elemental distribution, with an adjustable microstructure, and with completely clean grain boundaries can be produced [Pen02].
- The design of ceramics on the basis of molecular units becomes possible in order to control the structure and properties of such a material on an atomic scale [Bil96].
- Well established processing techniques for polymers can be applied at relatively low temperatures (1000 °C) to produce ultra high temperature stable materials (up to 2200°C).
- The synthesis of a variety of materials is possible, like powders, bulk materials, fibres, coatings, and membranes [Kro00].

In principle, two types of materials have to be distinguished, Si-C-N and Si-B-C-N, which are different mainly in their chemical and structural stability at high temperatures. The most important physical and chemical properties are summarized in the following. For further reading it is referred to Refs. [Bil98, Bil99, Kro00].

Si-C-N ceramics form an amorphous non-equilibrium state after thermolysis, which is stable up to about 1500 °C [Bil98]. Investigations with small and wide angle X-ray and neutron diffractometry [Bil00, Sce98, Dur97, Dur98, Hau04a] as well as nuclear magnetic resonance [Scu01] proved a phase separation of the material on the sub-nanometer scale, where amorphous $Si_{3+0.25x}C_xN_{4-x}$ (x = 0 - 4) domains and graphite-like amorphous carbon

domains with sp^2 hybridised structural units coexist [Hau04a, Bil00]. Typical diameters of the amorphous domains after thermolysis are about 0.7 nm [Bil98]. Annealing leads to a growth in domain size, and for temperatures above 1500 °C crystallization of SiC and Si_3N_4 occurs, leading to the formation of multiphase composite material which is extensively discussed in section 7. The overall high temperature stability of the material is limited by the decomposition reaction

$$Si_3N_4 + 3\ C \leftrightarrow 3\ SiC + 2\ N_2, \tag{2.1}$$

where Si_3N_4 reacts with carbon to SiC and nitrogen. Nitrogen leaves the material in gaseous form which leads to a considerably mass loss [Pen02].

The incorporation of several percent of boron into Si-C-N, using boron modified polymers or monomers, results in the formation of quaternary Si-B-C-N ceramics, which greatly retard decomposition. The thermal stability is increased to about 2000 - 2200 °C. The as-thermolyzed ceramics are also phase separated in an amorphous $Si_{3+0.25x}C_xN_{4-x}$ (x = 0 - 4) phase and an amorphous graphite-like BNC_x phase [Hau04b]. Here, BN-rings are incorporated in a graphite-like phase resulting in amorphous or turbostratic BNC_x. Possible reasons for the increased high temperature stability are (1) turbostratic BNC_x layers segregated at grain boundaries act as diffusion barriers for N and C, preventing the decomposition of Si_3N_4 [Sei98]. (2) The encapsulation of Si_3N_4 crystallites with BNC_x leads to an enhancement of the local N_2 pressure at the grain surface, which increases the decomposition temperature significantly (internal pressure effect) [Sei98]. (3) In BNC_x the C activity is decreased in comparison to elemental carbon, which also might enhance the decomposition temperature. (4) The structural disorder of the amorphous state leads to an enhanced activation enthalpy of the decomposition reaction [Wan01]. A clear experimental evidence does not exist for any of these possibilities.

For amorphous Si-C-N, Vickers hardness values are determined which are comparable to reaction bonded Si_3N_4 (10 GPa), and which can be enhanced by a reduction of porosity up to 16 GPa [Kro00]. Exceptionally high viscosities were measured at high temperatures, up to six orders of magnitude higher than those of fused silica [An98, Rie98]. The deformation rate is composed of two components, a stress independent component due to shrinkage and a stress dependent component due to viscous flow, which can be described by the free volume model [Chr00, Chr01a, Chr01b, Zim02]. Nano-composite ceramics crystallized at 1900 °C [Kum04] are still in the primary stage of the creep process, which is interpreted as viscous flow of the matrix. An improvement of the creep resistance at high loads up to 100 MPa is attributed to the presence of large elongated crystallites embedded in the amorphous matrix which reinforce the ceramic [Kum04].

The oxidation resistance of Si-C-N is remarkably enhanced in comparison to that of conventional Si_3N_4 based ceramics and is as good as for Chemical Vapour Deposition

(CVD) derived SiC and Si_3N_4 materials, or even better [Raj01]. During oxidation a cristobalite layer of some µm thickness is formed on the surface of the ceramics during annealing in air [Rie95] which prevents further oxidation. A parabolic growth law is observed [Bha04]. For Si-B-C-N, extremely thin oxide scales are found for experiments at 1500 °C [But01], however, difficulties due to bubble formation arise [But00, But01]. Other authors found an indication for protecting $BN(O)/SiO_2$ double layers [Bal94a]. An anomalously high resistance against oxidation is found for recently synthesized Si-Al-C-N ceramics, where a steady state oxidation rate is observed, indicating a modified oxidation mechanism [An04]. The rate constants are about one order of magnitude lower than those of CVD SiC, which is probably due to oxide layers composed of Si and Al containing oxides [An04]. Similar results were found for Si-B-C-N-Al ceramics, where the addition of Al significantly improves the oxide scale quality with respect to adhesion, cracking, and bubble formation [Mul04].

The electrical properties of Si-(B-)C-N materials can be characterized by a semiconducting electrical behaviour which strongly depends on chemical composition, on microstructure, and on thermal treatment [Her01, Ram01]. The dc-conductivity at room temperature can be varied between 1 and 10^{-15} Ω^{-1} cm^{-1}, which is a much broader range than for doped silicon, indicating the potential of this material as a tuneable electrical conductor [Kro00]. The electric conductivity behaviour is consistent with a variable-range-hopping mechanism at low temperatures and seems to be strongly connected with the property of hydrogen to bind to carbon atoms and the ratio of sp^2/sp^3 hybridisation, which influences the energy barrier of charge transport [Her01].

Several of the above mentioned properties of Si-B-C-N materials are strongly connected with atomic re-arrangement processes which depend on long range diffusion in the solid state. The most important ones are the de-mixing and crystallization process of amorphous materials which leads to nano-composite materials, creep processes in the amorphous state which determine the mechanical properties, and finally the mobility of hydrogen in the Si-C-N network triggering the electronic and also possible optoelectronic properties. From the viewpoint of fundamental science, Si-(B-)C-N precursor ceramics are a new form of a glassy-like state with an enormous stability range up to 1700 °C. Interesting investigations on the elementary process of diffusion in covalently bound multinary amorphous materials become possible, which could not be carried out in the limited stability range of e. g. CVD derived amorphous silicon, where crystallization occurs around 600 °C [Spi98].

2.2. Magnetron Sputtered Films

A further promising method to produce metastable amorphous materials of the system Si-C-N in form of layers or films is reactive magnetron sputtering. The possibility to synthesize layers with a low impurity content makes these materials well suited for an investigation of the thermodynamic stability, of the crystallization behaviour, and of atomic transport properties. In the present study, the transformation from amorphous to

polycrystalline films is investigated for silicon carbide and silicon nitride. Since the nucleation and growth process during crystallization may affect significantly the microstructure of the films, these data are very important for an adequate use as high temperature stable coatings and amorphous semiconductors. The results are also used as reference data for Si-C-N precursor ceramics. Silicon nitride is used as a model system in order to study the self-diffusion in covalent materials in the amorphous and crystalline state in direct comparison. In addition, measurements on the diffusion of hydrogen are carried out, which is important for electronic and optoelectronic applications.

2.2.1. SiC Films

Silicon carbide (SiC) is the mostly used high temperature stable non-oxide hard material, obeying an excellent high temperature creep resistance, a high thermal conductivity, and an excellent oxidation/corrosion resistance with classical applications as abrasive coatings, as heating elements, and in engine parts [Kom94, Sch94]. Since the beginning of the 1980's a high interest exists also in amorphous and crystalline SiC films as part of electronic or optoelectronic components [Pow88]. Due to the combination of its physical properties, SiC is one of the most appropriate semiconductor material for applications at high temperatures, high powers and high frequencies [Pow88, Dav93, Rea96, Har01]. SiC has a covalent bonding character, a decomposition temperature of about 2500 °C and occurs in form of various polytypes (6H, 4H, 3C etc.) [Kom94]. Films or coatings of SiC can be produced by chemical vapour deposition and liquid phase deposition [Pow88, Bru85, Gol92], molecular beam epitaxy [Fis02, Fuy89], polymer thermolysis [Mue02, Col97], pulsed laser deposition [Urb02, Rei98], ion beam synthesis [The99], and also magnetron sputter deposition [Sal02, Wah95]. Here, single crystalline films of high purity, defined polytypes, and tailored doping can be produced as well as amorphous and polycrystalline layers. For amorphous hydrogenated films, applications as solar cells [Gha99, Bul96, Pla95, Li92, Amb02, Fuj98, Taw82, Mah85], as light emitting diodes [Pat03, Fot01, Kru98, Lee96, Ham88], as photo receptors [Nis83, Kak83], and as phototransistors [Hon92] are possible. Further, protective surface coatings [Ord00, Riv98, Hir79], X-ray masks [Sil97, Hag90], and microelectro-mechanical systems (MEMS) [Ric03] made of SiC are realized or under development. Up do now, systematic studies on the thermally stability of amorphous films and on the crystallization behaviour are relatively scare and only carried out for films deposited on Si substrates [Ino87, Cal01].

2.2.2. Si_3N_4 Films

Thin films of amorphous and crystalline silicon nitride (Si_3N_4) exhibit also a variety of attractive properties, like high hardness, chemical stability, a high dissociation temperature, high thermal shock resistance, a good creep behaviour, and a good oxidation resistance. In addition, the material is also a wide band gap semiconductor usable for electronic applications in form of thin films. These properties suggest mechanical, optical and electronic applications in various branches of technology. An overview on the general

properties and technological applications of bulk silicon nitride and amorphous silicon nitride films can be found in Refs. [Bon89, Ham94, Ril00, Agn00, Hab94]. The crystal structure of Si_3N_4 is formed by tetrahedral coordinated silicon atoms, where the nitrogen atoms are connected to a three dimensional amorphous or crystalline structure [Ril00]. Amorphous hydrogenated Si_3N_4 films can be used as a versatile dielectric for device passivation, as a gate dielectric in a-Si:H thin film transistors, and as a charge storage medium in non-volatile memories [Lus98, Arn93, Rob94, Sta99].

Various methods of preparation of silicon nitride films have been used during the last decades, like chemical vapour deposition at low gas pressure (LPCVD), plasma-enhanced chemical vapour deposition (PECVD), and related methods, as well as magnetron sputtering [Hab94]. Up to now, several publications on amorphous silicon nitride films can be found in literature, dealing with synthesis, microstructure, optical properties, electronic properties, and mechanical properties [Mog75, Sei84, Ste94, Loe98, Kim98, Pat02]. However, no systematic studies were carried out on the thermal stability, on the crystallization behaviour, and on the diffusion properties of these amorphous films as a function of temperature and annealing time in order to understand the underlying kinetic process.

2.2.3. Si_2CN_4 Films

Si_2CN_4 is a material where nominally one silicon atom is replaced by a carbon atom. For Si_3N_4, tetrahedral coordinated silicon atoms are present, where the nitrogen atoms are connected to a three dimensional amorphous network structure [Ril00]. For Si_2CN_4, corner-linked Si_3N_4 layers are connected via carbodiimide bridges (N=C=N) to form the crystal structure [Rie97, Ama99]. Up to now, the synthesis of this compound was only successful by thermolysis of polyorganosilylcarbodiimides [Rie97, Gre97] in form of powders. Recently, such a structure was also verified by Fourier Transform Infrared Spectroscopy (FTIR) and Raman spectroscopy in isotope substituted ($^{14}N/^{15}N$) thin films deposited by reactive r. f. magnetron co-sputter deposition [Lut01] or by ion beam synthesis [Lik99].

3. Experimental Details

3.1. Synthesis

3.1.1. Polymer-Derived Si-(B-)C-N Ceramics

The polymer-derived bulk ceramics under investigation in this study were produced by uni-axial hot-pressing and subsequent thermolysis of cross-linked pre-ceramic polymers in an argon atmosphere at the Max-Planck-Institut für Metallforschung in Stuttgart, Germany. Different types of amorphous Si-C-N and Si-B-C-N ceramics were synthesized (see Tab. 3.1). The ternary Si-C-N ceramics were derived from polyvinylsilazane (VT50, Hoechst AG, Germany) and polyhydridomethylsilazane (NCP200, Nichimen Corporation, Japan). Three different types of amorphous Si-B-C-N ceramics were synthesized, referred as AM26, T21, and MW33. The Si-B-C-N ceramics T21 and MW33 were produced from different boron modified polysilazanes, on different reaction pathways. The T21 precursor [Rie96] was obtained by hydroboration of dichloromethylvinylsilane and subsequent ammonolysis (monomer route) while the MW33 polymer (*1P* in Ref. [Wei00]) was prepared via ammonolysis of dichlorovinylsilane followed by hydroboration (polymer route). The AM26 precursor was derived from bis(trivinylsilyl)carbodiimide by complete hydroboration of the vinyl groups (polymer 5 in Ref. [Mul02a]). After synthesis, the polymers were cross-linked at temperatures between 200 °C and 400 °C in vacuum (10^{-3} mbar). Bulk amorphous ceramics were produced by grinding and shaping the cross-linked polymers into cylinders with a diameter of 18 mm and a thickness of about 0.5 - 5 mm by uni-axial hot-pressing at pressures between 40 - 50 MPa and temperatures between 200 - 400 °C. The specimens were then thermolyzed in a quartz or an alumina tube. The AM26 samples were heated up with a rate of 1 °C/min to 500 °C, were isothermally annealed at this temperature for 12 hours and then heated with 10 °C/min up to 1000 °C and annealed at this temperature for 4 hours. For the other materials T21, MW33, VT50, and NCP200, a one step thermolysis was carried out with a heating rate of 25 °C/min up to the thermolysis temperature, and then holding at this temperature for 4 hours in argon. Thermolysis resulted in nearly crack-free homogeneous amorphous bulk ceramics, which were cut in about 5 x 5 x 2 mm^3 slaps and polished with SiC grinding paper (1200, 2400, 4000 mesh) and with diamond paste (grain size: 6, 3, and 1 μm). The samples were cleaned with ethanol after polishing in an ultrasonic bath. Details of the preparation procedure are given in the cited references in Tab. 3.1. The chemical composition of the samples was detected by Non-Rutherford Backscattering Spectrometry (n-RBS), Energy Dispersive X-ray Analysis (EDX), and chemical analysis. In addition to the constituting elements Si, C, N, and B, amounts of O (2 - 3 at.%), are present and also of H (4 - 7 at.%) as measured with additional Nuclear Resonant Reaction Analysis (NRRA). The chemical composition of the investigated samples is given in Tab. 3.1 and is illustrated in the phase tetrahedron of Fig. 3.1. The exact hydrogen concentration for the different types of materials is given in Tab. B.4 in the Appendix.

Table 3.1 Overview on the polymer-derived ceramics investigated in this study. Given are the materials short name, the chemical composition in the as-thermolyzed state, the thermolysis temperature, and references to more detailed work on synthesis

Materials name	Chemical composition (at.%)	Thermolysis temperature (°C)	Reference
VT50	$Si_{26}C_{41}N_{33}$	1050	[Bil98]
NCP200	$Si_{38}C_{23}N_{39}$	1050	[Bil98]
T21	$Si_{29}B_{10}C_{42}N_{19}$	1400	[Rie96]
MW33	$Si_{24}B_9C_{43}N_{24}$	1050	[Wei00]
AM26	$Si_{13}B_{13}C_{60}N_{14}$	1000	[Mul02a]

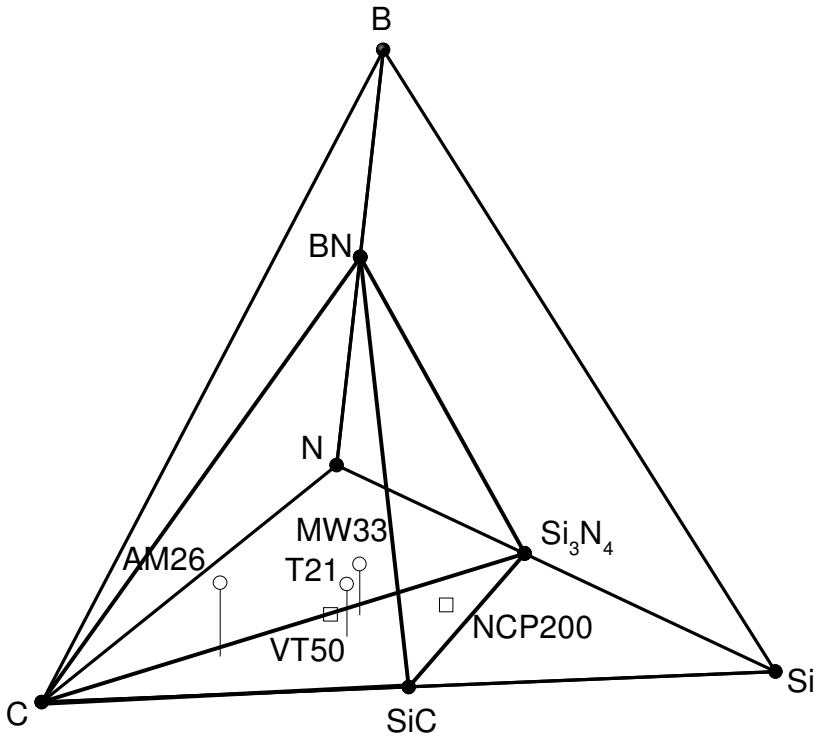

Figure 3.1 Chemical composition of the as-thermolyzed amorphous ceramics; ○: Si-B-C-N and □: Si-C-N; also shown are important binary compounds.

3.1.2. Magnetron Sputtered Films

The preparation of 1 - 2 µm thick films was carried out by r. f. magnetron sputtering in co-operation with Dr. M. Bruns from the Forschungszentrum Karlsruhe. Deposition was achieved using a 3 inch US GUN low profile planar magnetron source (AP&T, Nürtingen,

Germany) mounted on a standard DN 150 CF double-cross recipient equipped with pre-sputter shutter and sample positioner. Deposition rates of 2 - 5 nm/min are achieved, using an operating pressure of (1 – 5) x 10^{-3} mbar and a sputtering power of 80 - 160 W. The silicon nitride films were produced by reactive sputtering using a gas mixture of 50 vol. % Ar and 50 vol. % N_2 and a silicon target (99.999%, Norwegian Talc, Germany) at a substrate temperature of 400 °C. SiC based films were made by co-sputtering of silicon and carbon stripes of 5 x 25 mm^2 (99.99%, Goodfellow, Germany) in argon at a substrate temperature of 200 °C. Films with nominal composition Si_2CN_4 were produced by a combination of both methods [Lut98]. As substrates, single crystalline Si <111> wafers (CIS, Germany), polycrystalline SiC (BCS, Germany), and glassy carbon (Sigradur G, HTW, Germany) were used. The substrates (platelets of 10 x 10 x 2 mm^3) were polished with diamond paste down to a surface roughness smaller than 5 nm and cleaned with ethanol in an ultrasonic bath before sputter deposition.

The chemical composition and the elemental depth distribution of all films were determined by n-RBS and the subsequent simulation of the n-RBS spectrum with the computer code RUMP [Doo86]. Homogenously distributed stoichiometric films were obtained for all types of materials with an impurity concentration of 1.5 at. % argon and 0.1 - 0.5 at.% oxygen. A hydrogen concentration between 0.2 and 0.6 at.% (see Appendix/Tab. B.4) is determined by additional NRRA measurements at a depth of about 500 nm.

3.1.3. Other Types of Materials

In addition to the magnetron sputtered films, about 3.5 µm thick layers made of B-N-C were investigated, which were supplied by Mrs. S. Stöckel and Prof. Dr. G. Marx from the Institut für Physikalische Chemie at the TU Chemnitz. The films with an approximate nominal composition of $B_{50}N_{28}C_{22}$ were produced by plasma enhanced chemical vapour deposition (PECVD), and contain about 1 at.% of oxygen and about 2.6 at.% of hydrogen impurities. The films remain amorphous during annealing up to at least 1000°C.

Investigations were also carried out on glassy carbon, which is a commercial product obtained from HTW, Germany (Sigradur G). Glassy carbon is produced by a thermolytic method [Due84] similar to that one used for polymer-derived ceramics as explained in section 3.1.1. In this material, sp^2 hybridised graphite-like planes are present, which are not three dimensional ordered, but polymer-like arranged.

3.2. Experimental Determination of Self-Diffusivities

As already discussed in section 1, the investigation of self-diffusion in the present Si-C-N based and related systems raises numerous analytical problems. To overcome these problems, the rare stable isotopes ^2H, ^{10}B, ^{13}C, ^{15}N, ^{30}Si are used as tracers. As tracer deposition methods, ion implantation, sputter deposition, and isotope exchange from the

gas phase are applied and SIMS, SNMS, and NRRA are utilized as depth profiling methods. The diffusion measurements were carried out in the following way:

- Deposition of the stable tracer isotopes on the sample surface or into the sample
- Diffusion annealing at high temperatures
- Analysis of the isotope distribution as a function of depth (depth profile analysis) and comparison with the unnealed sample
- Determination of the diffusivities by least-squares fitting of the experimental data to analytical or numerical solutions of phenomenological models.

3.2.1. Tracerdeposition

The easiest way to deposit stable tracer isotopes on the surface of a sample is to solute it in an organic solvent, like acid, and to drop a small amount of it on the sample surface with a special pipette. This method is widely used for oxide ceramics, however, for non-oxide materials it is in general not applicable. A further problem is that oxide-free tracers like ^{30}Si are not commercially available in sufficient quantities. A chemical reduction of oxides (e. g. of $^{30}SiO_2$) is difficult to achieve and generally not very successful [Wel00]. To overcome these problems, the following special methods of tracer deposition were tested on functionality during this work: ion implantation, isotope exchange from the gas phase, and magnetron sputter deposition.

(a) Ion implantation

A well suited method for tracer deposition of nearly all elements which have stable isotopes is the method of ion implantation. Using this technique, a ion beam of the respective element with natural isotope composition (e. g. ^{28}Si: 92.2 %, ^{29}Si: 4.7 %, ^{30}Si: 3.1 %) is produced from a solid state or gas target. To extract the required positively charged isotopes, the ions are accelerated to energies in the keV range (10 - 50 keV), than the isotope is separated in a magnet, scanned and implanted in the sample several nanometers beyond the surface. Advantages of the present method are: (1) due to the deposition of the tracer several tens of nanometers in the interior of the sample, surface effects (thin oxide layers, dissociation effects etc.) are omitted. (2) The deposition of tracers with concentrations higher than the solubility limit is enabled. (3) The low straggling of the implantation profile between 10 - 50 nm (depending on the energy of the implanted ion, the sample density, and the atoms present in the material) allow the determination of low diffusivities, which are expected in the Si-C-N compounds. On the other hand, the main disadvantage of ion implanted tracers is the generation of extended defect areas due to the interaction of the high energy implantation ions with the sample atoms. These defects may have an extensive effect on diffusion profiles. A problem that is addressed in this work in sections 4 and 6.

With a special designed multiuse ion implanter located at the Institut für Kernphysik (J. W. von Goethe-Universität Frankfurt, Germany) several types of stable isotopes were implanted for use in this study. An overview on the implanted ions, the used targets, the samples, the energies, and the fluence are shown in Tab. 3.2. The boron implantations were carried out at the Centre de Spectrométrie Nucléaire et de Spectrométrie de Masse (Université de Paris-Sud 11, Orsay, France).

Table 3.2 Overview on the implanted ions, the targets, the energies, and the fluence used for the implantation process.

Implanted isotope	Ion	Target	Energy (keV)	Fluence (ions/m^2)
^{2}H	H_3^+	^{2}H gas	20	2×10^{19}
^{10}B	B^+	$^{10}BF_6$ gas	30	1×10^{20}
^{13}C	C^+	^{13}CO gas	30	2×10^{20}
^{15}N	N^+	$^{15}N_2$ gas	30	2×10^{20}
^{30}Si	Si^+	Si solid	30	8×10^{19}

(b) Magnetron sputtered isotope heterostructures

A method of tracer deposition in order to investigate impurity diffusion is the deposition of a thin tracer layer (10 - 100 nm) on the sample surface with CVD, magnetron sputtering, or pulsed laser deposition. A requirement for these methods is the existence of a target or a gas source enriched with the necessary tracer isotope. For self-diffusion experiments, such targets made of rare stable isotopes are generally badly available and very expensive so that only a limited amount of diffusion samples is available for experiments.

In the present work, the self-diffusion of Si and N in silicon nitride is investigated using isotope enriched layers of the form $^{28}Si_3{}^{14}N_4/Si_3{}^{15}N_4/^{28}Si_3{}^{14}N_4$ with dimensions in the nanometer range (isotope heterostructures). Such a heterostructure is schematically sketched in Fig. 3.2. Here, the tracer is introduced into the system in-situ during synthesis by reactive r. f. magnetron sputter deposition. A mixture of 50 vol. % argon and 50 vol. % nitrogen, either nitrogen with natural isotope ratio ($^{14}N_2/^{15}N_2$ = 99.63 %/0.37 %) or isotopically enriched nitrogen ($^{14}N_2/^{15}N_2$ = 0.5 %/99.5 %) was used in combination with different isotope enriched silicon targets. Three different layers of silicon nitride are deposited on a substrate with different isotope combinations. For layer II a normal Si target with a natural abundance of the Si isotopes (^{28}Si: 92.2 %, ^{29}Si: 4.7 %, ^{30}Si: 3.1 %) is used with ^{15}N enriched sputter gas. In contrast, for layer I and II a ^{28}Si enriched Si target is used

with ^{14}N gas. The commercially available ^{28}Si target (Isonics Corp., U.S.A.) has a thickness of only 30 µm and is mounted on a conventional Si target. Consequently, only a very limited amount of deposition runs and also diffusion experiments could be carried out using this method. During annealing, layer II serves as a tracer layer and the diffusion of the isotopes in the silicon nitride layers I and II is investigated. The deposition parameters are given in section 3.1.2. As substrates, polycrystalline SiC was preferred to Si wafers to ensure a high temperature stability of the system over 1400 °C and to enable an in-situ crystallization of the heterostructures in order to investigate diffusion also in the crystalline state.

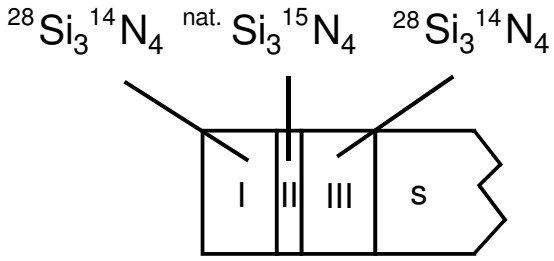

Figure 3.2 Schematic sketch of a silicon nitride isotope heterostructure deposited on a substrate (s). For details see text.

(c) Isotope exchange from the gas phase

This method, shortly termed as gas exchange, can be applied for tracer deposition of gaseous species and is used in the present case for the isotope combination of $^{1}H/^{2}H$ and $^{14}N/^{15}N$. For these elements the concentration of the rare isotope in the sample is very low (1.5×10^{-2} % for ^{2}H and 0.366 % for ^{15}N) so that the sample can be considered as composed of only one isotope (^{1}H or ^{14}N). During diffusion annealing in an atmosphere enriched with the rare isotope, an exchange process of the isotope in the sample and the isotope in the gas takes place, resulting in a penetration of the tracer into the sample without changing the chemical composition of the sample. A disadvantage of this method is that the exchange process at the sample surface, which describes the dissociation of the gas-molecule, the adsorption at the surface, and the subsequent incorporation of the tracer atom into the lattice, often leads to problems, especially at low temperatures. An example for this effect is given in section 5.3 in case of silicon nitride. Experiments concerning hydrogen diffusion are carried out in a gas mixture composed of 6 % $^{2}H_2$ and 94 % naturally N_2 (further termed N_2 - 6 % $^{2}H_2$), where the enrichment with deuterium was sufficient enough to realize the expected gas exchange. Prior to diffusion annealing the bulk samples are pre-annealed in N_2 - 6 % $^{1}H_2$ gas in order to establish a defect equilibrium. The combination of gases was used to ensure a nitrogen partial pressure close to 1000 mbar during annealing.

3.2.2. High Temperature Annealing

In order to achieve diffusion, annealing is carried out in the temperature range between 600 and 1700 C° using three different furnace systems:

(1) A modified commercial high temperature furnace system (XERION, Germany), was utilized to carry out anneals from 1 to 10 h at very high temperatures (1500 – 2000 °C). The system is equipped with a tungsten heating element and operates in high vacuum ($<10^{-5}$ mbar at 2000 °C) or high purity inert atmosphere (Ar, N_2, N_2 - 6 % H_2), obtaining a maximum heating rate of 30 °C/min. Temperature controlling was carried out with a W/Re thermocouple located close to the sample.

(2) In a special designed muffel furnace in which an Al_2O_3 tube or alternatively a quartz glass tube is mounted, experiments up to 1700 °C or 1200 °C, respectively, are carried out for annealing times from 10 min to several days. A special mechanical transfer unit was constructed which enables a transfer of the sample under vacuum or inert gas without getting contact to air. The samples can be placed inside the hot zone of the furnace in inert gas within 5 min. Consequently, this furnace was used for experiments where very short heating times were required. Temperature controlling was carried out with a calibrated Pt/Rh (type B) thermo couple with an accuracy of ± 2 °C at 1700 °C.

(3) For long time anneals of several weeks a simple Al_2O_3 tube furnace with a SiC heating element was used operating in nitrogen or argon atmosphere. Here the sample was placed in the cold furnace and heated up to a maximum temperature of 1250 °C in about 2 - 4 hours. Here, the ramping time can be neglected in comparison to the annealing time of some weeks. Temperature controlling was again achieved with a conventional Pt/Rh (type B) thermo couple.

These systems were build up to enable anneals at distinct temperatures and times under controlled atmosphere in a complementary way. If not otherwise indicated, the samples were placed in a crucible and were embedded in powder of the same material to avoid decomposition and contamination with oxygen during annealing. The annealing process was carried out in high purity argon (4.8), nitrogen (4.8) or hydrogen enriched nitrogen atmospheres.

3.2.3. Isotope Depth Profile Analysis

Isotope depth profile analysis was carried out with SIMS, SNMS, and NRRA. These methods are discussed in details in section 3.4.

3.2.4. Determination of Self-Diffusivities

In general, diffusivities were determined by least-squares fitting the experimental data to an appropriate analytical solution of the diffusion equation (Fick's second law)

$$\frac{\partial c(x,t)}{\partial t} = D\frac{\partial^2 c(x,t)}{\partial x^2}, \tag{3.1}$$

under consideration of the corresponding initial and boundary conditions. Here, D is the diffusivity and $c(x, t)$ is the space and time dependent concentration of the tracer. A compilation of useful solutions can be found in Ref. [Cra75]. For ion implanted tracers the starting profile (initial condition) can be approximated very well by a Gaussian function

$$c(x,t) = \frac{A}{\sqrt{2\pi\,\Delta R_{\mathrm{p}}{}^2}}\exp\left(-\frac{(x-R_{\mathrm{p}})^2}{2\,\Delta R_{\mathrm{p}}{}^2}\right), \tag{3.2}$$

where, A is the fluence of the implanted tracer, R_{p} is the projected range, and ΔR_{p} is the profile width. After diffusion annealing we obtain

$$c(x,t) = \frac{A}{\sqrt{2\pi\,(\Delta R_{\mathrm{p}}{}^2 + 2Dt)}}\exp\left(-\frac{(x-R_{\mathrm{p}})^2}{2\,\Delta R_{\mathrm{p}}{}^2 + 4Dt}\right), \tag{3.3}$$

with t as the annealing time. For samples where a relatively high amount of tracer leaves the sample during the diffusion process, the assumption of a sink at the sample surface is useful, leading to

$$c(x,t) = \frac{A}{\sqrt{2\pi\,(\Delta R_{\mathrm{p}}{}^2 + 2Dt)}}\left[\exp\left(-\frac{(x-R_{\mathrm{p}})^2}{2\,\Delta R_{\mathrm{p}}{}^2 + 4Dt}\right) - \exp\left(-\frac{(x+R_{\mathrm{p}})^2}{2\,\Delta R_{\mathrm{p}}{}^2 + 4Dt}\right)\right]. \tag{3.4}$$

If a tracer layer of thickness h is located in the interior of the sample, like for isotope heterostructures (Fig. 3.2) , the solution of Eq. (3.1) is given by

$$c(x,t) = c_\infty + \frac{(c_0 - c_\infty)}{2}\left[\mathrm{erf}\left(\frac{x-l}{R}\right) + \mathrm{erf}\left(\frac{h+l-x}{R}\right)\right], \tag{3.5}$$

where c_∞ is the concentration in layer I and III, c_0 in layer II, respectively, and l is the thickness of the top layer. The quantity R, which describes the broadening of the tracer profile is treated as a fitting parameter. The self-diffusivity D at time t is determined from the difference in R of the diffusion profile and of the starting profile according to $D = (R^2(t) - R^2(0))/4t$.

Assuming an infinite tracer source at the surface, like for annealing in isotopically enriched gases (gas exchange), the diffusion depth profile is given by

$$c(x,\mathrm{t}) = c_0 \mathrm{erfc}\left(\frac{x}{2\sqrt{Dt}}\right). \tag{3.6}$$

Here, c_0 is the atomic fraction or concentration of the tracer at the sample surface. Under the assumption that the incorporation of the tracer atoms from the gas phase is governed by a first-order surface exchange process, a more complicate solution is achieved which is given by

$$c(x,t) = c_{\mathrm{g}}\left[\mathrm{erfc}\left(\frac{x}{2\sqrt{Dt}}\right) - \exp\left(2\frac{x}{2\sqrt{Dt}}\sqrt{\frac{k_{\mathrm{s}}{}^2 t}{D}} + \frac{k_{\mathrm{s}}^2 t}{D}\right)\mathrm{erfc}\left(\frac{x}{2\sqrt{Dt}} + \sqrt{\frac{k_{\mathrm{s}}{}^2 t}{D}}\right)\right], \tag{3.7}$$

where c_{g} is the concentration of the tracer in the gas phase and k_{s} is the surface exchange coefficient, which is used as a second fitting parameter.

Diffusion profiles which could be not described by the simple diffusion equation were calculated numerically by solving modified diffusion equations with computer calculations (for an example see the trap-limited diffusion of hydrogen in section 6). These calculations were carried out on a commercial personal computer using a home made C++ program code based on finite differences.

3.3. Investigation of Crystalline Phase Formation

Investigations on the formation of nano- and micro-crystalline precipitations in an amorphous matrix were examined mainly by X-ray Diffractometry (XRD). Here, an ex-situ method was preferred to an in-situ method because of the easier handling of the material in an oxide-free atmosphere at very high temperatures up to 1900 °C and because of the long annealing times up to typically 100 h. For a detailed understanding of the crystallization process, XRD studies were carried out as a function of annealing time. The following systematic procedure was applied: first, the amorphous material was isothermally annealed at a distinct temperature in the range between 1400 and 1900 °C in high temperature furnaces for a given time (see section 3.2) Then the material was characterized by XRD and afterwards annealed again. Certain Bragg peaks were numerically fitted with a Lorentzian function, from which the integrated peak area $I(t)$ and the full width at half maximum $\beta(2\theta)$ of the corresponding peak were determined. From these quantities information on the average crystallite size and the fraction of crystallized phase can be determined. Further details are given in section 7. In addition, investigations with Transmission Electron Microscopy (TEM) and also SIMS were performed to obtain the necessary information.

3.4. Analytical Methods of Sample Characterization

3.4.1. Secondary Ion Mass Spectrometry (SIMS)

During this study, isotope depth profiles were mainly measured by Secondary Ion Mass Spectrometry (SIMS). Here a ion beam (O_2^+, O^-, Cs^+) is accelerated to the keV range, focused to the µm range, and rastered over an area of about 250 x 250 μm^2 of the sample surface. The interaction of the high energy primary ions with the sample surface leads to the ejection of positive and negative charged species from the surface. The ejected species may include atoms, clusters of atoms, and molecular fragments. These ions are energy filtered, mass analysed, and afterwards detected with a Faraday cup or an electron multiplier. From the sputtered area about 20 % in the centre were gated for further signal processing. During sputtering, a crater evolves at the sample surface and a element depth profile can be provided, where the intensity of secondary ions I_i is plotted against the sputtering time. The crater depth is measured with a mechanical profilometer (TENCOR, Alphastep 500) with a tungsten tip and the time scale is converted into a depth scale under the assumption of a constant sputter rate. One of the big advantages of the SIMS technique is that it is isotope sensitive over nearly the whole periodic system of elements. Thus it provides an unique possibility to investigate self-diffusion with stable isotopes. As the probability of ionisation in SIMS is highly variable, it is difficult to quantify SIMS data. For the present self-diffusion measurements a quantification of the isotope concentration is obtained by measuring the intensity of all stable isotopes of an element and calculating the fraction, X_i, of a special isotope according to

$$X_i = \frac{I_i}{\sum I_i}. \tag{3.8}$$

Here from the concentration of isotope i, c_i, can be calculated with the knowledge of the element concentration, c, according to $c_i = X_i\, c$, which was determined by other methods like EDX or n-RBS. For ion implanted samples, the isotope concentration can also be calculated using the known fluence of the implanted isotope for calibration. The fluence is given by the integrated area, J, of the implantation profile after subtracting the background

$$J = \int_0^\infty c_i(x,t)\ \mathrm{d}x. \tag{3.9}$$

The present experiments were carried out with three different SIMS machines, which are characterized in Tab. 3.3. The CAMECA IMS-3F system that works with an O^- ion primary beam was used to prevent electrical charging during the measurement of insulating samples. Here, the samples were additionally coated with a thin layer of gold before SIMS analysis. More detailed information on depth profiling with SIMS can be found in Refs. [Bri83, Ben87, Vic90].

Table 3.3 Different types of secondary ion mass spectrometers used in this work.

SIMS machine	Primary ion	Primary energy (keV)	Primary current (nA)	Secondary ions	Mass separation
CAMECA IMS-3F	O^-	15	20 - 150 nA	H^+, B^+, C^+, N^+, Si^+	double focusing
CAMECA IMS-5F	Cs^+	14	5- 30 nA	H^-, N^+, Si^+	double focusing
VG SIMS/SNMS LAB	O_2^+	7	20 - 300 nA	B^+, Si^+, CN^-	quadrupole

3.4.2. Secondary Neutral Mass Spectrometry (SNMS)

With SNMS, neutral atoms which were produced during the sputter process are used instead of ions to obtain information on the elements and isotopes present in a the sample. For analysis, an electron beam SNMS apparatus (VG SIMS/SNMS Lab.) with an Ar^+-ion primary beam (7 keV, 0.3 - 1μA) was used, which is located at the Ecole des Mines de Nancy (France). Here the neutrals produced during the sputter process were past-ionisized, mass separated with a quadrupole mass spectrometer, and detected with a channeltron. The major advantages of this method compared to SIMS are: (1) it is possible to sputter isolators without deposition of a gold layer on the surface and (2) a low matrix-effect enables a good element quantification. A big disadvantage of this method is the generation of only low secondary ion intensities during analysis. The SNMS method is used in a complementary way to the SIMS method.

3.4.3. Nuclear Resonant Reaction Analysis (NRRA)

The basic principle of measuring isotope depth profiles with NRRA is the use of induced nuclear reactions. This technique is especially sensitive to light isotopes with atom numbers below 20. During this study, the isotopes ^1H and ^{15}N were detected with NRRA. Both isotopes have a strong resonance in the cross section of nuclear reactions, induced by ions with energies in the MeV range. For the detection of ^1H, the nuclear reaction $^1H(^{15}N, \alpha\gamma)^{12}C$ at a resonance energy of 6.4 MeV [Kha89] and for the detection of ^{15}N, the reaction ^{15}N (^1H, $\alpha\gamma)^{12}C$ at a resonance energy of 429 keV [Rol74] were used. The high cross section of the later reaction of σ_0 = 300 mb and the narrow width of the resonance reaction of only 120 eV [Rol74, Lan78, Hor88] makes it well suited for isotope depth profiling. On their way through the sample a specific energy loss occurs for particles above the resonance energy. Depth profiling is achieved by varying the energy of the incoming beam. The energy loss is calculated with the program package “Stopping and Range of Ions in Matter“

(SRIM-2003) for specific sample compositions. The detection of ^{1}H was mainly carried out in order to determine the hydrogen concentration of a sample in a defined depth beyond the sample surface. One of the most interesting features of this method is that a direct quantification of the isotope concentration in a matrix of known composition is possible using a standard. Since this method is non-destructive it is well suited for additional investigations with other methods in direct comparison. More details are given in Refs. [Tes95, Kha89].

The measurements were carried out with the 2.5 and 7 MeV Van-de-Graaff accelerators at the Institut für Kernphysik (J. W. von Goethe-Universität Frankfurt, Germany). The particle energy was varied in steps of 500 eV. The depth resolution at the surface is about 4 nm at a tilt angle of 65 ° between the sample normal and the analysing beam, deteriorating with depth due to energy straggling. The nuclear reactions were detected due to the emerging gamma rays with a 5"x 5" NaI(Tl) scintillation detector at an energy of 4.43 MeV.

3.4.4. (Non-)Rutherford Backscattering Spectrometry (n-RBS)

Elemental composition determination of Rutherford Backscattering Spectrometry is based on the elastic scattering of monochromatic $^{4}He^{+}$ (or $^{4}He^{++}$) ions with an energy of typically 1-2 MeV at the coulomb potential of a solid target material, where two completely unscreened nuclear point charges are assumed. Elemental depth profiles are detected measuring the energies and the number of the backscattered ions from the target. The backscattered He particles are energy analysed by a Si surface barrier detector positioned at a backscattering angle of 171 ° with respect to the incident ion beam. The energy of the backscattered He ions is given by the conservation of energy and momentum between the incident ion and the scattering atom and can be related to the depth and mass of the target. The number of backscattered ions from any given element is proportional to its concentration. The simulation of the RBS spectrum with the computer code RUMP [Doo86] enables to determine the chemical composition of a sample. During this study RBS was used for the detection of B, C, N, Si, Ar, and O. When the collision diameter of the particles is very small and becomes comparable to the sum of the nuclear radii of the He and the target atom, the finite sizes of the nuclei and the nuclear force interactions lead to an enhancement of the Rutherford scattering cross section. Such non-Rutherford backscattering (n-RBS) at an energy of about 3.2 MeV was used to enhance the sensitivity in the detection of ^{15}N and ^{16}O. The measurements were also carried out with the 7 MeV Van-de-Graaff accelerator at the Institut für Kernphysik in Frankfurt. More details on RBS and n-RBS can be found in Refs. [Chu78] and [Tes95], respectively.

3.4.5. X-Ray Diffractometry (XRD)

X-ray diffractometry was used for phase analysis in order to determine the structural state of a sample (amorphous, micro- and nano-crystalline) and also to monitor the time

evolution of crystallization, growth, or transformation processes. A Siemens D 5000/Kristalloflex diffractometer with CoK_α tube radiation (40 keV, 40 mA) was used. As standard analysis, measurements in Bragg-Brentano geometry ($\theta/2\theta$ modus) were performed with a scintillation detector. In addition, for thin film analysis a gazing incidence set-up at a fixed angle of 1° was used for a better sensitivity. Besides standard XRD data collections [Vil91], the program POWDERCELL for WINDOWS 2.3 (PCW) was used for data analysis [Kra96]. For bulk material, an adjustable sample holder was constructed to position the sample surface reproducibly in the incidence plane of the X-rays. Coarse grained SiC and Si_3N_4 powder were used as a reference material to discarded any relevant influence of instrumental broadening on crystallite size analysis. More information on XRD analysis can for example be found in Ref. [Klu74].

3.4.6. Transmission Electron Microscopy (TEM)

Transmission electron microscopy (TEM) is an imaging technique where a beam of high energy electrons is focused on a thin layer. The transmitted electrons are used to obtain enlarged images of the specimen under investigation. The spatial resolution is in the nm range. Additional Selected Area Electron Diffraction (SAED) patterns can be used to get information on the local structure of the material.

Investigations with TEM were carried out in collaboration with different project partners. Characterizations of the system Si-B-C-N were enabled at the Max-Planck-Institut für Metallforschung, Stuttgart with a ZEISS EM912 microscope equipped with an Omega energy-filter operating at 120 kV. Investigation on the SiC system were made in cross sectional configuration, using a Hitachi microscope at an acceleration voltage of 100 kV and a field emission gun electron microscope (JEOL 2010F) operating at 200 kV, located at the Université de Bourgogne (Dijon, France). The chemical composition of the films was determined by EDX analysis (ISIS EDX Spectrometer, Oxford). Sample preparation for TEM analysis was carried out by gluing two sandwiched SiC films in a brass tube holder with a diameter of 3 mm and cutting this arrangement into discs of 0.5 mm thickness. The usual grinding, polishing and dimpling method (Dimple Grinder Model 656, Gatan) followed by ion beam milling (PIPS Model 691, Gatan) was used to obtain a film thickness which is transparent to high energy electrons. More details can be found in [Fot05].

3.4.7. Fourier Transform Infrared Spectroscopy (FTIR)

In order to detect bonds present in the investigated materials, experiments with Fourier Transform Infrared Spectroscopy (FTIR) were carried out in co-operation with the Institut für Kernphysik (J. W. von Goethe-Universität Frankfurt). The FTIR transmission spectra were recorded with a Nicolet Magna-IR 550 spectrometer with a spectral resolution of 4 cm^{-1}.

4. Self-Diffusion in Polymer-Derived Amorphous Si-(B-)C-N Ceramics

The investigation of self-diffusion in polymer-derived amorphous Si-(B)-C-N ceramics (precursor ceramics) is motivated by the fact that thermally induced atomic re-arrangement processes, occurring during the formation of crystalline phases or in the amorphous state due to phase separation, are controlled by self-diffusion of the constituting elements. In order to get insight into the reasons for the metastability of Si-(B)-C-N materials and in order to obtain process parameters for the production of tailor-made microstructures for applications, it is necessary to quantify reliable diffusion data. Self-diffusivities are also necessary for an understanding of high temperature creep and oxidation processes. From the viewpoint of fundamental science, Si-(B-)C-N precursor ceramics are a new form of a glassy-like state. The high crystallization temperature above 1500 °C offers the possibility to carry out investigations on the elementary process of diffusion in covalently bound multinary amorphous materials, which could not be undertaken in the limited stability range of e. g. CVD derived amorphous silicon, where crystallization occurs around 600 °C [Spi98]. The possibility to obtain high quality amorphous bulk ceramics from our co-operation partner at the Max-Planck-Institut für Metallforschung in Stuttgart, enabled to carry out the first self-diffusion measurements in these new materials. For an overview on the fundamental properties of self-diffusion in the solid state it is referred to the following elementary textbooks [Phi91, She86, Meh90, Fly72, Heu89].

In section 1 various analytical problems were discussed, which complicate tracer self-diffusion measurements in non-oxide ceramic materials. Si-(B)-C-N is a good example for such a kind of material. These ceramics are covalently bound and have extremely high dissociation temperatures up to 2200 °C, so that low diffusivities are expected to be present. Temperatures of at least 1500 °C are necessary to carry out successful diffusion anneals. Because of the lack of suitable radioactive tracers, the diffusion measurements have to be carried out with stable isotopes and SIMS. Due to a difficult commercial availability of sufficient quantities of oxide-free tracer isotopes, ion implantation of Si, B, C, and N is used as the preferred method of tracer deposition (see section 3.2). The natural isotope background necessitates a fluence of implanted ions in the order of 1 x 10^{20} ions/m^2, which is expected to result in a considerable implantation damage, whose influence on diffusion has to be taken into account.

4.1. Characterization of the Diffusion Samples

For the diffusion experiments, two different types of Si-(B)-C-N ceramics with strongly differing high temperature properties are used: (1) boron free Si-C-N ceramics of type VT50 and (2) boron containing Si-B-C-N ceramics of type T21. The chemical compositions are given in Tab. 3.1 and Fig. 3.1. A heat treatment of 2 h was carried out in nitrogen prior to diffusion, to allow a relaxation of the samples to take place and to establish a metastable

equilibrium state as well as to remove the damage which may occur during polishing. A pre-annealing temperature of 1720 °C was chosen for T21 ceramics and of 1460 °C or of 1350 °C for VT50 ceramics, respectively, as a compromise between the following two criteria: (1) the samples should be mainly X-ray amorphous and (2) the metastable equilibrium should be established at a temperature as close as possible to the crystallization temperature in order to use the data for the modelling of the formation kinetics of crystalline phases in section 7. The influence of pre-annealing on diffusion was investigated exemplarily for VT50 ceramics in case of silicon diffusion.

The results of the X-ray analysis of the samples, as discussed in detail in section 7, show that pre-annealed Si-C-N samples do not reveal any individual Bragg peaks of crystalline phases. This indicates that the sample is still amorphous at these temperatures as determined by TEM investigations [Bil98] and neutron diffractometry [Hau04a] for as-thermolyzed Si-C-N. For Si-B-C-N pre-annealed at 1720 °C, the main part of the sample volume is still amorphous, however, a small amount of crystalline SiC (~ 15 %) is precipitated with an average crystallite diameter of about 5 nm[*]. These precipitates do not disturb the motion of atoms in the amorphous phase significantly because no percolation path is formed. This high pre-annealing temperature of the Si-B-C-N material was chosen with respect to the fact that diffusion is very slow and no systematic data could be obtained at temperatures below 1500 °C.

4.2. Depth Profile Analysis

Investigations on self-diffusion in Si-(B)-C-N ceramics were carried out with the ion implanted stable isotopes ^{10}B, ^{13}C, ^{15}N, and ^{30}Si (for details see section 3.2). Here, depth profile analysis and self-diffusivity determination in Si-(B)-C-N material of type T21 is exemplarily discussed in detail for nitrogen. Fig. 4.1 shows the ^{15}N concentration depth profile for an as-implanted sample as obtained by SIMS detecting $^{12}C^{15}N^-$ secondary molecule ions. The ^{15}N concentration is determined from the intensity of the secondary ions using the implanted dose of 2×10^{20} ions/m^2 as a calibration standard (see section 3.2). As shown in Fig. 4.1 the concentration of implanted ^{15}N tracer can be approximated very well with a Gaussian distribution with a projected range of $R_p = 74$ nm and a width of $\Delta R_p = 33$ nm (see Eq. (3.2)). The projected range is in good agreement with the profile simulation of the SRIM-2003 program package [Zie03, Zie85] for a density of 2.3 g/cm^3 ($R_p = 74$ nm), which is based on Monte Carlo simulations. However, the width is slightly enhanced in comparison to the theoretical value of $\Delta R_p = 28$ nm, which can be attributed to profile broadening occurring during the SIMS sputtering process due to surface roughness and ion beam mixing. For an exact analysis, the SIMS secondary ion signal $I(x)$ recorded as a function of sputter depth has to be expressed as the convolution integral [San84]

[*] This state is further termed amorphous for simplicity.

$$I(x) = \kappa \int_{-\infty}^{\infty} R(x - x')\ C(x')\ \mathrm{d}\,x', \tag{4.1}$$

where κ is an instrumental factor, $R(x)$ is the resolution function of the SIMS apparatus and $C(x)$ is the original tracer distribution. Generally, the resolution function $R(x)$ can be approximated well with a Gaussian function with a width of ΔR_R. From probability theory it is known (see e. g. Ref. [Fel66]) that the convolution of two Gaussian functions of width ΔR_p and ΔR_R results also in a Gaussian function of width $\Delta R_M^2 = \Delta R_p^2 + \Delta R_R^2$, where ΔR_M is the width measured with SIMS and ΔR_p is the width of the original tracer distribution. Thus the width of the resolution function of Si-B-C-N ceramics can be assessed to ΔR_M = 17 nm, by comparison of the measured data with the SRIM-2003 calculations. Now, the diffusion profiles can be corrected using this value. However, since for the diffusion profiles $\Delta R_M^2 >> \Delta R_R^2$ is valid, the resulting error in the diffusivity is lower than 10 % which can be neglected in comparison to other sources of errors, like, e. g., the correct crater determination due to surface roughness.

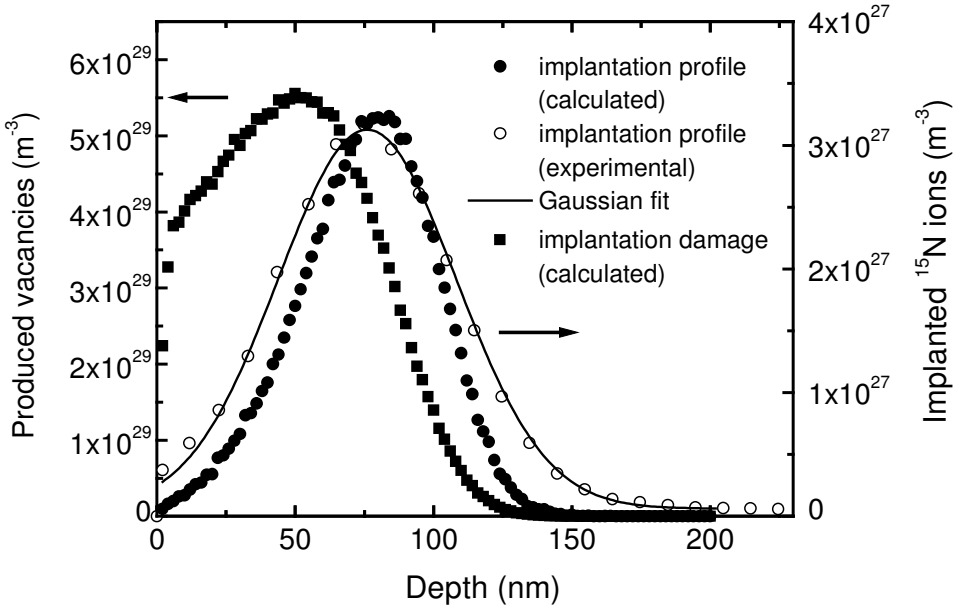

Figure 4.1 Depth profiles of ^{15}N ions implanted in amorphous Si-B-C-N (T21). The experimentally determined SIMS depth profile, the Gaussian fit to the experimental data, and the data calculated with SRIM-2003 are shown. Also included is the damage profile created by the implantation process (fluence: 2 x 10^{20} ions/m^2) as calculated by SRIM-2003, expressed as produced vacancies.

In Fig. 4.2 the ^{15}N depth profiles of a T21 sample which was diffusion annealed at 1700 °C for 1 h and 5 h, respectively, are compared to the implantation profile. If a diffusion process can be described by Fick's second law (Eq. 3.1), diffusion annealing of a Gaussian starting profile should lead to a profile broadening according to Eq. (3.3) as indicated in Fig. 4.2 as a solid line. For the present case, the experimental depth profiles of the diffusion annealed samples exhibit a strongly different behaviour. The profiles in Fig. 4.2 can be separated into two regions. For depths smaller than 120 nm, the width of the Gaussian

profile is nearly unchanged ($\Delta R_p = 33 \pm 6$ nm) during annealing. In contrast, for depths larger than 120 nm appreciable profile broadening occurs for a small amount of tracer with increasing annealing time, which can be attributed to diffusion. These observations can be explained qualitatively with the following model: it is assumed that only a small fraction of the implanted ^{15}N ions is mobile (about 5 %) which takes part in the diffusion process. The rest of the ^{15}N ions are immobilized, forming the static part of the profile. The presence of the high amount of immobile atoms can be explained with the formation of extended defect areas (e. g. agglomerates of vacancies) produced by the high-dose implantation process of 30 keV ^{15}N ions. During this process the ion beam interacts with the sample atoms by elastic and inelastic scattering, which leads to the production of displaced atoms and vacancies. These vacancies, located mainly in a region slightly narrower than the projected range (see Fig. 4.1), can agglomerate if the implanted dose is high enough, and may act as a sink for the diffusion species and immobilize them by trapping. This is in strong contrast to the behaviour of point defects like single vacancies or interstitials which may enhance diffusion, like, e. g., in case of transient enhanced diffusion (TED) in semiconductors (see e. g. Ref. [Gil98]). The observed decrease in the implanted dose of about 50 % indicates a superimposed strong outward diffusion of the implanted tracer to the sample surface. This has the consequence that the diffusion profile cannot be detected anymore for very long annealing times (see section 5.1)

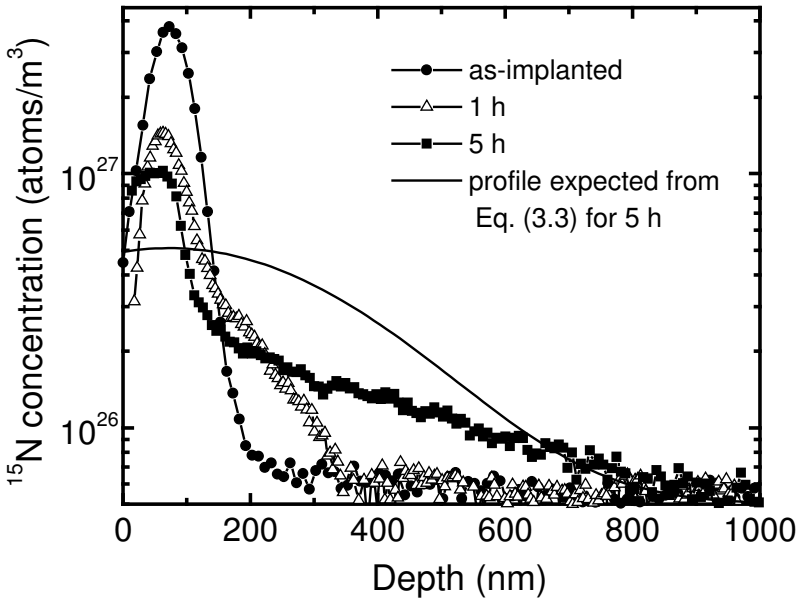

Figure 4.2 ^{15}N isotope depth profiles for implanted T21 ceramics (pre-annealed at 1720 °C) before and after annealing for 1 h and 5 h at 1700 °C in nitrogen as measured with SIMS. The expected behaviour according to Eq. (3.3) is also indicated.

In the present case, it is necessary to modify the diffusion equation (3.1) for a determination of the self-diffusivities by a term that includes the interaction of the tracer with the implantation damage and to solve this equation numerically by computer calculations. Here, a model is used where the diffusion of implanted ^{15}N atoms is

influenced by the formation of immobile complexes of the form NR_e at implantation induced trapping centres R_e according to

$$N + R_e \leftrightarrow NR_e. \tag{4.2}$$

The corresponding differential equations can be formulated using Fick's second law and a source and a sink term. Under the assumption that the total concentration of traps remains constant over the diffusion time, the motion of nitrogen is then given by

$$\begin{aligned}
\frac{\partial [N]}{\partial t} &= D_N \frac{\partial^2 [N]}{\partial x^2} - k\,[N][R_e] + \nu\,[NR_e], \\
\frac{\partial [NR_e]}{\partial t} &= k\,[N][R_e] - \nu\,[NR_e], \\
\frac{\partial [R_e]}{\partial t} &= -\frac{\partial [NR_e]}{\partial t},
\end{aligned} \tag{4.3}$$

where [N] is the concentration of freely migrating ^{15}N tracer, $[NR_e]$ is the concentration of tracer trapped to the implantation damage, $[N_{tot}] = [NR_e] + [N]$ is the total amount of tracer as measured by SIMS, $[R_e] = [R_e](x)$ is the depth dependent concentration of trapping sites, D_N is the nitrogen diffusivity, k is the trapping rate, and ν is the dissociation rate of NR_e complexes. As shown in Fig. 4.1 the initial concentration of implanted ^{15}N tracer, $[N]_0$, can be approximated with a Gaussian distribution. The initial depth dependent concentration of traps introduced by the implantation process $[R_e]_0$ is in principle unknown. For the present purpose this quantity is modelled theoretically with the SRIM-2003 program, which calculates the vacancy depth distribution (damage events) produced by an implantation process. These damage data are used as starting conditions for the present system of differential equations. As can be seen in Fig. 4.1 the centre of the implantation damage zone is about 30 nm closer to the surface than the projected range, indicating that the maximum trapping events are expected in that area. However, the nature of these traps and their concentration are unknown. Annealing of the samples may lead to a recovery process and to the formation of defect clusters which reduces the concentration of traps[*]. Therefore, the factor $[R_e]_0$ is used only as "shape factor" describing the depth dependence of traps and not as an absolute value, so that the product $[R_e] \cdot k$ adequately describes the experimentally obtained depth profile as a fitting parameter. The only constrain is that $[R_e]_0 > [N_{tot}]_0$. As boundary conditions all concentration values at the surface are set to zero, which accounts for the observed outward diffusion of the tracer.

[*] This process is assumed to take place during the very first time of annealing, where no profile broadening due to diffusion occurs.

In Fig. 4.3 the results of the numerical calculations are compared to the experimental data of Fig. 4.1, using the values for the parameters k and ν, which are given in the caption of the figure. Diffusivities of $D_N = (1.7 \pm 0.7) \times 10^{-18}$ m^2/s and of $D_N = (2.3 \pm 0.9) \times 10^{-18}$ m^2/s are determined for the two annealing times, proving that no time dependence of the tracer diffusivities is observed within experimental errors. The simulations show also that the parameters k and ν (but not D_N) are strongly correlated, which means that the system is overdetermined. A good agreement between measured diffusion profiles and numerical calculations is obtained only for the conditions $\nu/k \approx 1 \times 10^{29}$ m^{-3}. It resulted also from the calculations that the condition $\nu/(k\,[R_e](x)) < 1$ has to be fulfilled for a significant immobilization of the tracer and the condition $\nu/(k\,[R_e](x)) > 1$ to observe diffusion broadening of the depth profiles. The limiting condition $\nu/(k\,[R_e](x)) = 1$ is present at a depth of about 110 - 120 nm where both phenomena are separated. In order to draw further conclusions on the trapping and de-trapping behaviour, investigations with high resolution TEM or Positron Annihilation Spectroscopy (PAS) would be necessary in order to quantify the defect clusters, which is beyond the scope of this work, because the aim of the numerical calculations is only to determine the correct diffusivities.

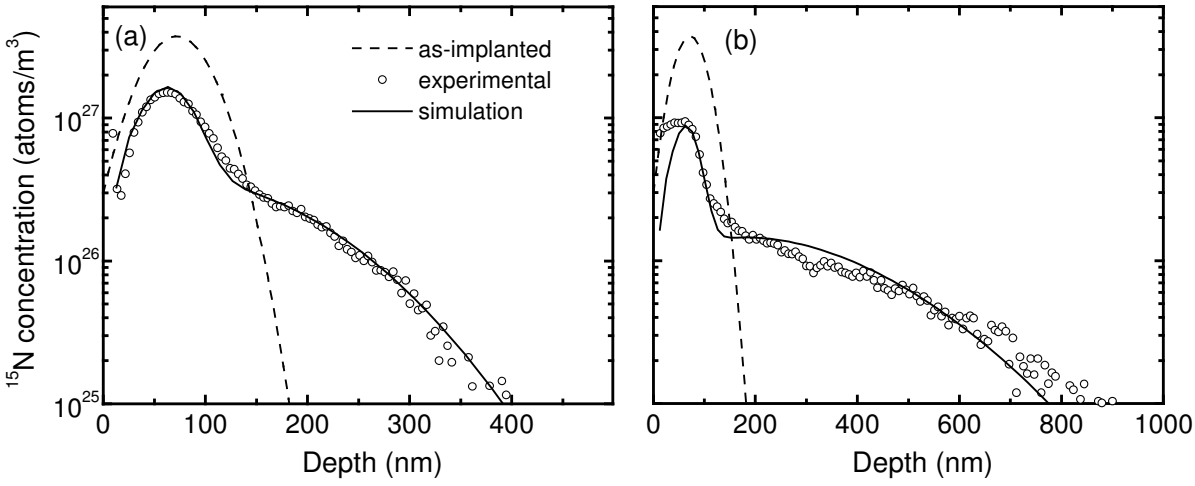

Figure 4.3 ^{15}N isotope depth profiles for implanted T21 ceramics after annealing at 1700 °C for **(a)** 1 h and **(b)** 5 h. The solid line corresponds to a numerical simulation of the profiles according to Eq. (4.3) with the parameters $k = 3 \times 10^{-27}$ m^3/s and $\nu = 3 \times 10^2$ s^{-1}. The background is subtracted for clarity.

For further analysis, a least-squares fit of the experimental data to the analytical solution of Fick's second law given in Eq. (3.4) was carried out in the depth range > 120 nm with A and D as fit parameters. This procedure leads to approximately the same diffusivities as obtained here by numerical calculations. This demonstrates that for the present case the implantation damage influences the form of the depth profiles drastically, but the determined diffusivities not significantly. The results demonstrate that the use of the analytical solution is a reliable way to determine diffusivities without carrying out time-

consuming numerical calculations, an assumption which was often presupposed but not proven up to now.

Using the stable isotopes ^{10}B, ^{13}C, and ^{30}Si, analogous experiments with ion implanted tracers were carried out in T21 material and the isotopes ^{15}N and ^{30}Si in VT50 material. An example for ^{30}Si depth profiles as obtained by measurements on VT50 ceramics is given in Fig. 4.4. A similar behaviour is found as for ^{15}N in T21, however, the isotope profiles at depths below 75 nm indicate a slightly weaker trapping of the implanted atoms in this material. More examples of depth profiles can be found in Refs. [Sch01, Sch02a].

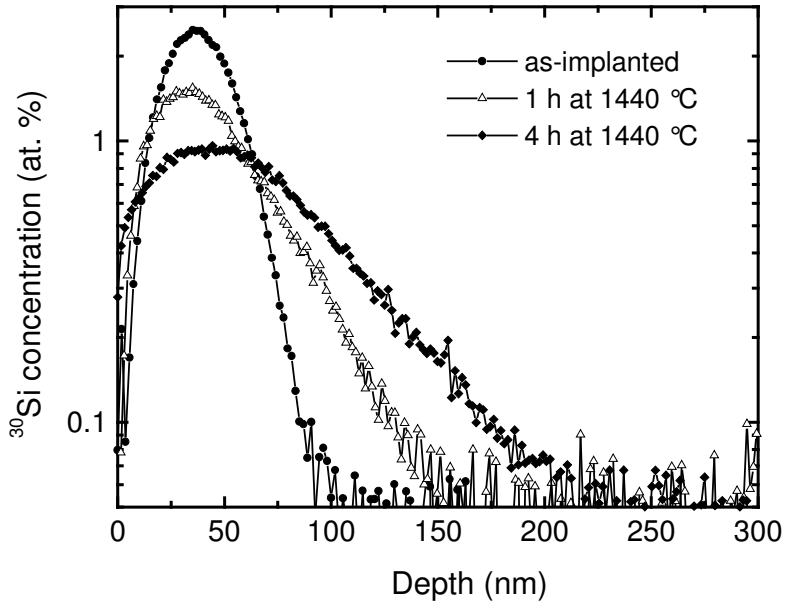

Figure 4.4 ^{30}Si isotope depth profiles for implanted VT50 ceramics (pre-annealed at 1460 °C) before and after annealing for 1 h and 4 h at 1440 °C in nitrogen as measured with SIMS. The background is subtracted for clarity.

4.3. Diffusivities and Activation Enthalpies

The determined self-diffusivities are plotted as a function of reciprocal temperature in Fig. 4.5. The B, C, N, and Si self-diffusivities in Si-B-C-N ceramics of type T21 do not show much variation and are in the same order of magnitude. This means that diffusion controlled atomic arrangement processes like crystallization or crystallite growth are not dominated by one type of element but are influenced by all elements rather equally. For B, N, and Si a thermally activated behaviour is observed in analogy to crystalline materials [Phi91] which can be described by an Arrhenius equation

$$D = D_0 \exp\left(-\frac{\Delta H^{\mathrm{D}}}{k_{\mathrm{B}} T}\right) \tag{4.4}$$

where D is the diffusivity of the corresponding element, ΔH^D is the activation enthalpy of diffusion, D_0 is the pre-exponential factor, T is the annealing temperature, and k_B is the Boltzmann constant. In case of C diffusion, only a single diffusivity was measured at 1700 °C which coincides with the data of boron. Very high activation enthalpies between 5.7 and 7.3 eV and pre-exponential factors between 1 x 10^{-3} and 5 m^2/s are obtained by least-squares fitting (see Appendix/Tab. B.1). Since the self-diffusivities of Si and N are very close together, the data can also be fitted with a unique Arrhenius straight line, which is also indicated in Fig. 4.5. Relatively large errors* of ΔH^D and D_0 are present here (see Appendix/Tab. B.1), which resulted mainly from the lack of accuracy in determining the exact crater depth during SIMS analysis due to the relatively high surface roughness of the samples (root mean square roughness (RMS) ≈ 500 nm, crater depth ~ 2-3 µm; error ≈ 20 %). Consequently, the activation enthalpies of the elements investigated coincide roughly within estimated errors and an average value of about 6.5 eV can be given, which indicates a typical activation enthalpy of self-diffusion for all elements.

For the VT50 ceramics, the diffusivities of silicon were measured as a function of annealing temperature and of pre-annealing temperature (Fig. 4.5). The self-diffusivities determined for samples pre-annealed at 1460 °C and 1350 °C can be fitted with a unique Arrhenius line. This indicates that diffusion is independent of pre-annealing in the temperature range investigated. Possible structural relaxation occurring during pre-annealing normally results in a decrease of free volume, which is defined as the difference between the actual volume of a sample and the volume of a sample with optimum packing. Such changes in free volume, if present, seem to influence the self-diffusion in Si-C-N not significantly, meaning that the defect concentration and the energetic processes governing diffusion are unchanged (at least approximately). For the Si diffusion in VT50 ceramics a similar activation enthalpy of 6.3 eV is obtained as for T21 ceramics. However, the diffusivities are about one order of magnitude higher than those of T21 in the whole temperature range investigated. The similarity of the activation enthalpies is reflected in a nearly parallel shift of the VT50 data to higher values. Due to the estimated errors attributed to the data it is not possible to decide which of the two parameters, D_0 or ΔH^D, is responsible for the shift of the data. Also measured was the self-diffusivity of N in VT50 ceramics at 1440 °C, which is lower by a factor of four than the corresponding value of Si but still in the same order of magnitude. Using the lowest diffusivities measured in Si-C-N and in Si-B-C-N, a maximum difference of a factor of eight occurs for these materials. This indicates that the assumption of a reduced element mobility in Si-(B)-C-N, compared to Si-C-N, as the reason of the enhanced high temperature stability of the first material (see Sec. 2.1) is in principle supported by the present data. For a further discussion see section 7.4.

Since the diffusion measurements in Si-(B-)C-N ceramics are extremely time consuming, further measurements for C in T21 and N in VT50 were omitted, because no drastic new results were expected. The self-diffusivity of C in VT50 ceramics could not be

* The errors of the activation enthalpy and of the pre-exponential factor resulted from a error weighted linear regression of the diffusivities.

quantified due to a strong outward diffusion of the tracer. In conclusion, it is found that the self-diffusivities in two selected Si-(B)-C-N materials do not vary drastically for the constituting elements and for different compositions.

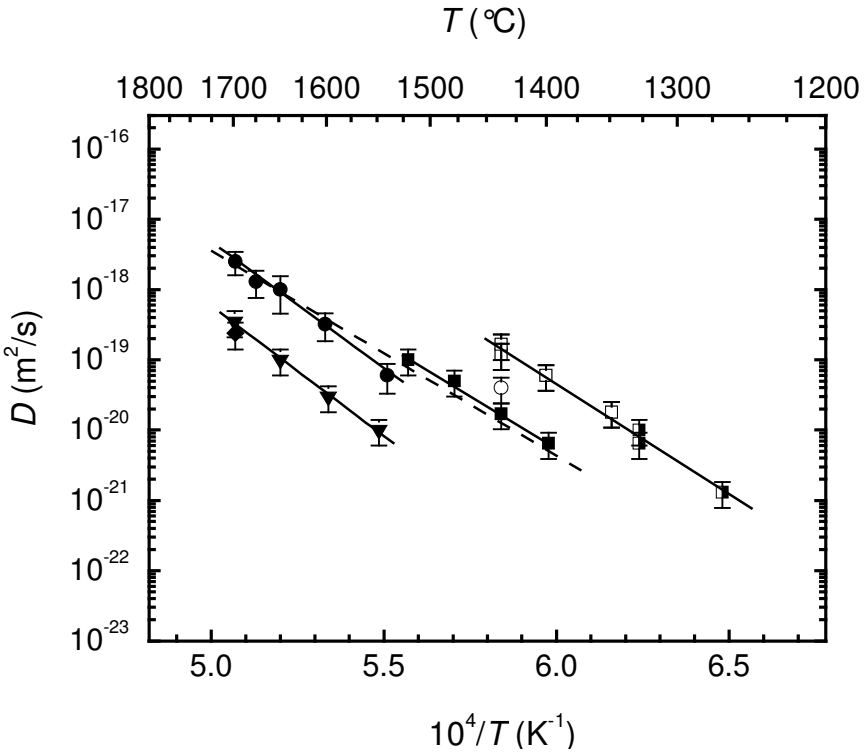

Figure 4.5 Self-diffusivities of the constituent elements as a function of reciprocal temperature for T21 ceramics pre-annealed at 1720 °C (filled symbols), VT50 ceramics pre-annealed at 1460 °C (open symbols), and VT50 ceramics pre-annealed at 1350 °C (half-filled symbols): ^{30}Si (square), ^{15}N (circle), ^{13}C (diamond), and ^{10}B (triangle).The dashed line corresponds to a common fit of Si and N diffusivities.

4.4. Diffusion Mechanisms

For materials in an amorphous or glassy state it is reliable to compare the measured diffusivities to those which were calculated from the viscosity, η, of the material according to the Stokes-Einstein relation*

$$D = \frac{k_B T}{6\pi\eta R} \tag{4.5}$$

where $R \approx 0.1$ nm is the atomic radius of the diffusing species. Using the experimentally determined viscosity for Si-B-C-N of $\eta \approx 10^{13}$ - 10^{14} Pa s at 1500 °C [Rie98, Chr00], a diffusivity in the order of $D \approx 10^{-24}$ - 10^{-25} m^2/s is expected, which is at least four orders of

* The Stoke-Einstein relation is often used to describe diffusion controlled crystallization processes in oxide glasses (see e. g. [Zan85] and references cited therein), where the validity of this relation is assumed.

magnitude lower than the experimentally determined value (see Fig. 4.5). For Si-C-N a similar difference is found at 1450 °C, a temperature where the viscosity reaches the value of 10^{12} Pa s [Rie98] and where the glass transition temperature is commonly defined, which separates a supercooled liquid from a glass. This invalidity of the Stokes-Einstein relation points to the fact that hydrodynamic flow does not govern the atomic transport in the amorphous state of Si-(B-)C-N and that diffusivity and viscosity are not mediated by the same kind of defects. At the temperatures investigated the amorphous matrix can be assumed to be rigid between consecutive diffusion jumps (the characteristic diffusion time is much smaller than the matrix relaxation time) and diffusion proceeds via thermally activated hopping. Consequently a diffusion mechanism in amorphous Si-(B)-C-N is proposed which is based on vacancy- or interstitial-like defects (quasi-defects) similar to crystalline solids. In crystalline solids, self-diffusion is realized by the mutual exchange of a vacancy (vacancy mechanism) or of a self-interstitial (indirect interstitial mechanism) with a regular lattice atom. In amorphous materials, a vacancy-like defect can for example be described as a point defect, where an atom is absent in the local short range order of the amorphous structure, e. g. the lack of an N atom in the tetrahedral coordination of silicon. Investigations with Positron Annihilation Spectroscopy (PAS) enable to determine free volumes (nano-voids, vacancies, double vacancies) present in solids. Recent measurements on Si-(B-)C-N ceramics [Rei03] show that in the amorphous state free volumes exist, which correspond to the lack of about 10-15 atoms. For Si-B-C-N a second type of free volumes is found between 1400 and 1600 °C, corresponding to the lack of 3 - 6 atoms. These large free volumes, which can be termed “nano-voids”, can hardly be identified as the defects governing diffusion.

For further discussion it should be kept in mind that the amorphous ceramics are phase-separated on the (sub-)nanometer scale in $Si_{3+0.25x}C_xN_{4-x}$ domains and in BNC_x domains for Si-B-C-N, and in Si_3N_4 domains and in C domains for Si-C-N (VT50), respectively [Hau04a, Hau04b]. Consequently, a homogeneous amorphous state does not exist, but a nano-structured inhomogeneous two-phase state. Since the two amorphous phases exist approximately in equal proportions, percolation paths very likely exist and both phases can serve as a diffusion path. In order to identify this path, a comparison of the Si and N self-diffusivities of precursor-derived Si-C-N to those of amorphous Si_3N_4 is useful. The self-diffusion in amorphous Si_3N_4 is discussed in detail in section 5. In Fig 4.6 the diffusivities of Si and N in amorphous Si_3N_4 (pre-annealed for 2 h at 1200 °C) are compared to those in Si-C-N. The diffusivities of both types of materials can be described with a unique Arrhenius line for each element. Values of ΔH^D = 5.6 eV and D_0 = 2 x 10^{-3} m^2/s are obtained for Si and of ΔH^D = 4.9 eV and D_0 = 1 x 10^{-5} m^2/s for N. A common fitting of Si and N diffusivities together results in an activation enthalpy of 5.5 eV, while the Arrhenius straight line in Fig. 4.6 is nearly identical with that formed by the Si diffusivities only (see also Appendix B.2). These findings imply that the diffusion process in VT50 ceramics is taking place via phase-separated amorphous Si_3N_4 domains, which form a percolation path through the amorphous material. The data also suggest that the same is true for the Si and N diffusion in T21, where diffusion is taking place along $Si_{3+0.25x}C_xN_{4-x}$ domains. The lower

diffusivities for T21 can be explained by the fact that additional carbon is partially substituted for N in this phase [Hau04b]. The small SiC crystallites (~ 5 nm) which are present in the T21 material at 1700 °C (see section 4.1) can most probably not serve as a transport path for diffusion because the amount of about 15 % of crystallized phase is not sufficient to establish a percolation path. Further, it is eye-catching that the self-diffusivities of Si and N are nearly identical for each element in amorphous Si-C-N, Si-B-C-N, and Si_3N_4 within the measured temperature range (see Fig. 4.5 and Fig. 4.6). This phenomenon and conclusions which can be drawn from it are discussed in section 5.

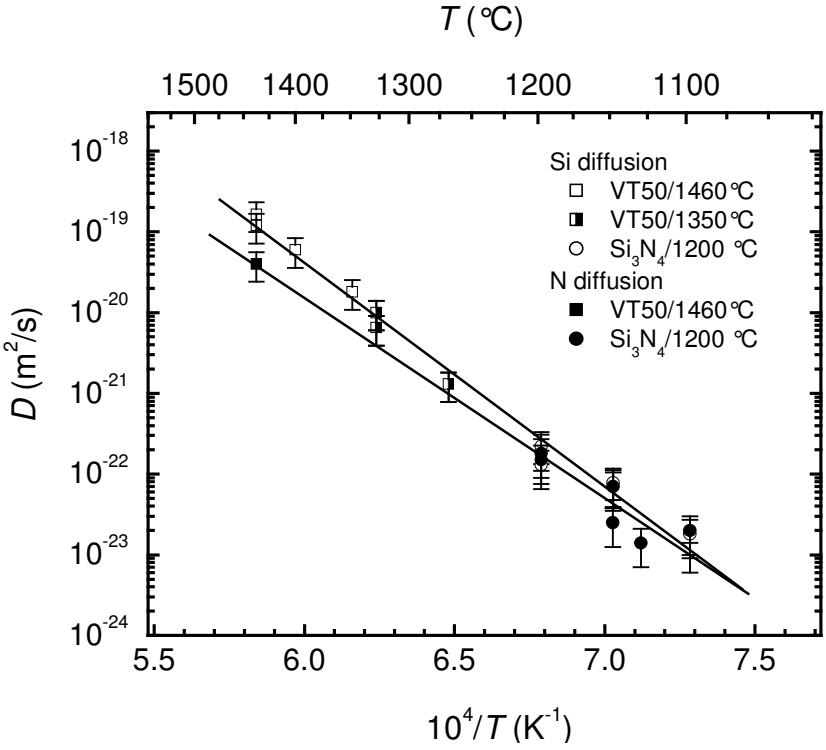

Figure 4.6 Diffusivities of Si and N as a function of reciprocal temperature for VT50 ceramics in comparison to magnetron sputtered amorphous Si_3N_4 films (see section 5). The pre-annealing temperatures are indicated.

Considering the boron diffusion, a modified interpretation is necessary. The only material where B diffusion data exist and which is comparable to Si-B-C-N in the broadest sense is crystalline SiC. Here, B is diffusing via the kick-out mechanism [Rus01], and is faster than Si diffusion by at least three orders of magnitude in contradiction to the findings here. This might be an indication that in case of amorphous Si-B-C-N, B is not diffusing via the $Si_{3+0.25x}C_xN_{4-x}$ phase, but via the BNC_x phase. For carbon no clear conclusion can be drawn from the present data.

In literature, investigations on the diffusion, and especially on the self-diffusion, in amorphous Si-(B)-C-N ceramics are extremely limited. In addition to the data presented here, there exist impurity diffusivities of Ge [Mat00] and Au [Mat01] in VT50, which are considerably faster and range between the self-diffusivities (section 4.2) and the

diffusivities of hydrogen (section 6). They also show an Arrhenius behaviour with activation enthalpies between 4.7 and 5.5 eV. Voss et al. [Vos03] carried out measurements on the self-diffusion of Si and C in T21 ceramics (pre-annealed at 1600 °C) using the ion implanted radioactive isotopes ^{31}Si and ^{11}C with a very short half-life period of less than 2 hours. Due to the experimental set-up [Vos02] the data are limited to diffusivities higher than 10^{-19} m^2/s. They found identical diffusivities for both elements obeying an Arrhenius behaviour with an activation enthalpy of 4.7 eV and a pre-exponential factor of 2.3 x 10^{-5} m^2/s. Astonishingly, these diffusivities are more than two orders of magnitude higher than those obtained in the present work. This can be explained under the assumption that diffusion takes place via different domains in the phase-separated amorphous structure. Using the radiotracer technique, a significantly lower fluence of only 10^{14} ions/m^2 has to be implanted to obtain reliable measurement data, because of the higher sensitivity of this method. This means that the diffusion process observed by Voss et al. is very probably not be detected with the method used in this study. The natural background concentration of stable ^{30}Si isotopes of 3.1 at. % will mask this process. It has also to be noted, that the experiments of Voss et al. were carried out at a reduced pressure of 10^{-6} mbar [Vos03]. Since the dependence of diffusion on the nitrogen activity in the surrounding gas atmosphere is still not investigated up to now, this might be an additional source for the differences.

For further analysis of the measured diffusivities, the equation

$$D_0 = f a^2 \nu_0 \exp\left(\frac{\Delta S^{\mathrm{D}}}{k_{\mathrm{B}}}\right) \tag{4.6}$$

is used, where f is the correlation factor, a the jump distance between two adjacent atoms, and ν_o the effective attempt frequency. From Eq. (4.6) the entropy of self-diffusion can be assessed from the pre-exponential factor. Using $a = 0.26$ nm, $f = 1$, and $\nu_o = 10^{13}$ s^{-1}, an entropy between $\Delta S^{\mathrm{D}} = 7$ and 16 k_{B} can be derived for Si-(B-)C-N materials. These values are much higher than those found for metals and intermetallic compounds of 1 - 5 e V [Phi91], but they are not uncommon for covalent semiconducting materials, like single crystalline Si [Bra98], Ge [Fuc95], GaAs [Wan96, Pal81], and SiC [Rus04, Lin04, Hon79, Hon80a, Hon80b, Hon81], where values in the order of 5 - 25 k_{B} were derived. For these semiconductors the high entropy of diffusion is explained by the presence of non-localized point defects extended over several neighbouring lattice sites [Fra91, Fra92, See68, See71]. This extended defect configuration may be realized by many microscopically different states with a high configuration entropy. The same is true for potential diffusion paths. Whether such a mechanism is present for Si-(B-)C-N ceramics, or not, cannot be decided unambiguously from the present results, especially if it is kept in mind that according to Zener [Zen52, Bej97] the entropy and the enthalpy of diffusion are related by $\Delta S^{\mathrm{D}} \sim \Delta H^{\mathrm{D}}/T_{\mathrm{m}}$ (T_{m}: melting temperature). This means that a high entropy of diffusion is connected with a high enthalpy of diffusion, which is also fulfilled here.

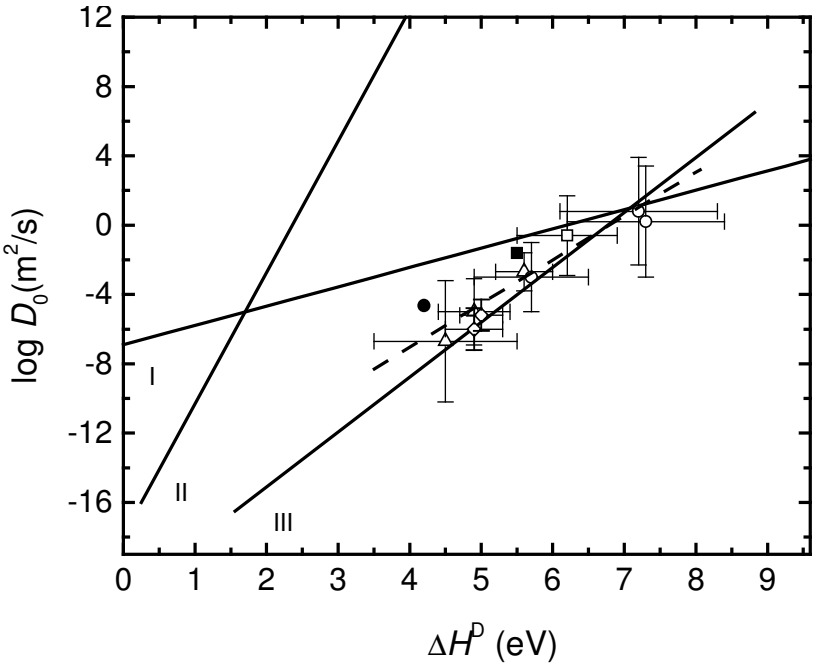

Figure 4.7 Plot of ΔH^D vs. log D_0 for self-diffusion in amorphous Si-(B-)C-N ceramics and amorphous Si_3N_4 films, as obtained in this study: Si, N, B in T21 (○), Si in VT50 (□), and Si, N in Si_3N_4 (△) as well as Si, N in crystalline Si_3N_4 (◇). Also given are the literature data of Si, C in T21 (●) [Vos03] and Ge, C in VT50 (■) [Mat01]. For comparison, schematic lines outlining the data of crystalline materials (including typical metals [Fau03, Heu92] and the semiconductors Si [Bra98], Ge [Fuc95], and SiC [Mat89]) (line I), of bulk metallic glasses [Fau03] (line II), and of crystalline silicates (Si-diffusion) [Bej97] (line III) are given. The dashed line indicates a possible correlation between materials based on SiN_4 tetrahedra.

An overview on the self-diffusivities in amorphous Si-(B)-C-N ceramics in context with literature data of other materials is given in Fig. 4.7, where the activation enthalpy of diffusion is plotted versus the logarithm of the pre-exponential factor. The data obtained for crystalline metals (0.5 - 3 eV) form straight line I, illustrating the validity of the Zener relation between ΔS^D and ΔH^D in this kind of materials. Also located on that line are the data for the crystalline semiconductors Si (4.8 eV), Ge (3.1 eV), and SiC (7.3 – 9.5 eV) within an estimated error of log $D_0 = \pm 1$. (Note that more recent measurement data obtained for self-diffusion in SiC [Rus04, Jan04] are located about four orders of magnitude below this line, indicating an unclear role of this material). The data of Si-(B)-C-N with high activation enthalpies (ΔH^D = 6 - 7.3 eV) are located very close to line I, however, at lower values of ΔH^D = 4.5 – 6 eV, log D_0 is considerably smaller for some orders of magnitude. A dashed line indicates a possible linear relation between D_0 and ΔH^D which might be valid for these materials, including the data of amorphous and crystalline silicon nitride, as determined in this work in section 5. This relation might be an indication for a unique or similar diffusion mechanism in materials with structures based on SiN_4 tetrahedra. For further discussion see also section 5. Also given in Fig 4.7 is the straight line III, which results for Si diffusion in crystalline silicates [Bej97] and which is very close to the data for Si-(B)-C-N. Here the basic structure element is a SiO_4 tetrahedron, which is quite similar to a SiN_4 tetrahedron, however with a more ionic bonding. Completely

different are the data for bulk metallic glasses (line II), where a typical collective diffusion mechanism is observed [Fau03, Zum00]. Here, several atoms participate in the jump process and very high values of D_0 (and also ΔS^D) occur for relatively low values of ΔH^D in contradiction to the present results.

4.5. Diffusion and Creep Behaviour

A fundamental process which is important for the application of Si-(B-)C-N as a structure ceramic is the high temperature creep behaviour. Creep is defined as the time dependent plastic deformation at constant stress. In ceramics, this phenomenon is often controlled by self-diffusion [Bar97]. The central quantity of this process is the deformation rate $\dot{\varepsilon}$, which is the response of a material on applied uni-axial stress σ. For amorphous materials or glasses creep is often governed by viscous flow, where a Newton viscosity can be defined as $\eta = \sigma/(3\dot{\varepsilon})$. The high temperature creep data of amorphous Si-B-C-N ceramics of type T21 between 1350 and 1500 °C consist of a stress dependent and a stress independent component of deformation, which is explained by shrinkage and by viscous flow, respectively [Chr00]. The latter component can be described very well by the free volume model [Spa77] where plastic deformation occurs due to the superposition of shear on localized groups of atoms referred as "flow defects". According to this model the viscosity becomes time and temperature dependent and can be described as

$$\eta = a(T) + bTt \tag{4.7}$$

with the abbreviation

$$a(T) = cT\exp\left(\frac{\Delta H^{fl}}{k_B T}\right), \tag{4.8}$$

where b and c are constants and ΔH^{fl} is the activation enthalpy of flow defect migration, which is often assumed to be identical to the activation enthalpy of flow defect annihilation. The time dependence of Eq. (4.7) can be explained by the annihilation of flow defects during annealing (structural relaxation) and the corresponding decease of free volume. As described in Ref. [Chr00], pre-annealing of the ceramics before creep-testing at 1400 or 1600 °C leads to a decrease of the deformation rate but not to a modification of the time dependence. Least squares-fitting of the experimental determined viscosity [Chr00] to Eq. (4.7) results in an activation enthalpy for the motion of flow defects of $\Delta H^{fl} = 6.2 \pm 1.0$ eV [Chr00]. Astonishingly, this value is in accordance with the activation enthalpy of self-diffusion. If this accordance is not accidental, it implies that both phenomena may be governed by the same activation process. However, as stated in section 4.4 diffusion and viscous flow are not mediated by the same kind of defects because the Stokes-Einstein

relation is not valid in the present case. Due to this finding, it can be speculated that the movement of flow defects is a superposition of several atomic re-arrangement steps, whose activation enthalpy correspond approximately to an atomic jump.

In order to interpret the observed time dependent viscosity to be a result of structural relaxation, investigations with PAS are very helpful, which give an insight into the presence of defects and free volumes. PAS measurements on amorphous Si-(B)-C-N ceramics carried out at 1400 °C revealed a significant decrease of free volumes during the creep process [Rei03]. However, experiments on samples which were only isothermally annealed in an unstrained state show that the average life-time of positrons trapped at free volumes remains constant at temperatures between 1400 and 1600 °C. This implies, that structural relaxations, and consequently a time dependent viscosity, are stress induced and not thermally induced. In addition, at temperatures above 1350 °C no significant time dependence of self-diffusion is observed during isothermal annealing, which is an argument against thermally induced structural relaxations. However, the impurity diffusivities of Ge in Si-B-C-N measured in the as-thermolyzed state are lower than the diffusivities measured on samples pre-annealed at 1600 °C [Vos03] which might be a hint for structural relaxation. In order to solve this puzzle, further detailed investigations on the time and stress dependence of diffusion and free volume annihilation are necessary.

5. Self-Diffusion in Magnetron Sputtered Si_3N_4 Films

The compound silicon nitride (Si_3N_4) is a further (also technologically) important model system that requires advanced experimental methods to determine reliable diffusion data. The special problems arising for Si_3N_4 and the strategies to overcome these problems are summarized here: (1) for both constituting elements no suitable radioactive tracers are available for the performance of extensive measurements. Consequently, the stable isotopes (^{14}N, ^{15}N) and (^{28}Si, ^{29}Si, ^{30}Si) have to be used as tracers. (2) The lack of large bulk Si_3N_4 single crystals and the presence of glassy, often impurity contaminated, intergranular phase in sintered or hot-pressed polycrystalline material considerably complicates self-diffusion measurements in bulk material. This problem is overcome by the use of magnetron sputtered Si_3N_4 thin films, which are nearly impurity free. (3) The existence of low diffusivities even at high temperatures and the geometry of thin films limited to the sub micrometer range necessitates the application of analytical methods with an excellent vertical depth resolution, like SIMS or NRRA. (4) Surface effects, such as oxidation, may influence the tracer deposition and the diffusion process substantially. Here, the deposition of the tracer beyond the surface, in the interior of the sample is to prefer. The existence of these problems is also reflected in the fact that in literature only a very limited number of publications on self-diffusion in silicon nitride exist [Kij76, Kun88] whose results are hardly convincing.

In this study, various methods were applied to overcome the described problems and to quantify the self-diffusivities in silicon nitride, namely ion implantation, isotope heterostructures, and isotope exchange from the gas phase. As will be shown, only the measurements with isotope heterostructures were fully successful. As a diffusion medium, magnetron sputtered films of about 0.5 - 1 μm thickness were used, which were deposited on a SiC substrate. As will be shown in section 8.1, the as-deposited films are amorphous and can be transformed into the polycrystalline state via controlled crystallization. Thus, diffusivities of the two elements nitrogen and silicon can be determined in the amorphous and polycrystalline state on the same material. This is a unique possibility to learn details on diffusion in different thermodynamic states, a task which is commonly difficult to realize. More details on the characterization of the films are given in section 8.1.

5.1. Measurements with Ion Implanted Isotopes

In contrast to the self-diffusion measurements in Si-B-C-N, which were discussed in section 4, ion implantation of stable tracers is not a successful tool for diffusivity determination in Si_3N_4. This is illustrated in Fig. 5.1 for the element silicon. Annealing of a Si_3N_4 film at a temperature of 1700 °C, which was implanted with ^{30}Si ions beforehand, shows no detectable broadening of the implantation profile. This can be explained with the fact that the fraction of diffusing ^{30}Si atoms is very small (below 3.1 %). Consequently the profile change due to diffusion is masked by the natural background concentration of ^{30}Si

isotopes in the sample of about 3.1 %. The diffusing atoms are hidden in the background and cannot be used to quantify diffusivities. The question why this phenomenon is not observed in Si-C-N is still unclear at the moment. However, a strong decrease of the implanted dose is observed with increasing annealing time, while the profile width remains constant at $\Delta R_p = 21 \pm 2$ nm. Annealing for about 5 h at 1700 °C leads to a complete vanishing of the implantation profile. The decrease of the implanted dose is due to a strong outward diffusion of the tracer close to the surface mediated by non-thermal point defects, left from the implantation process.

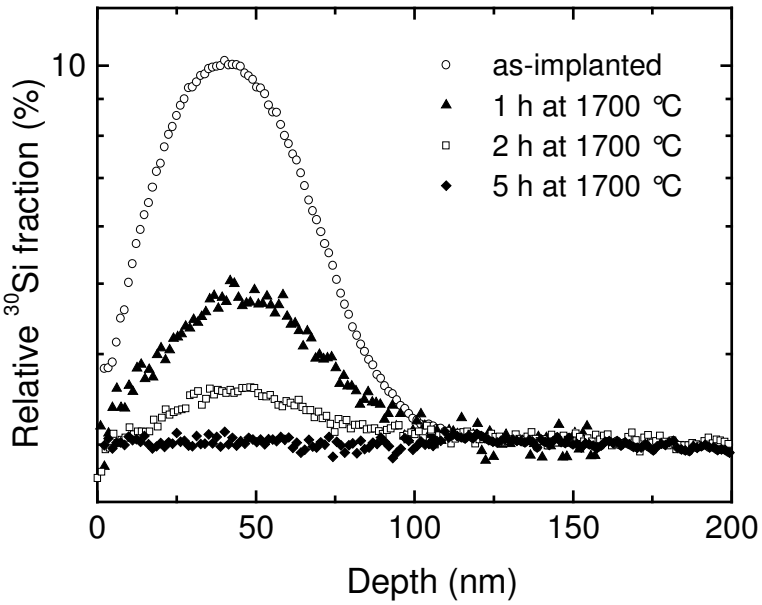

Figure 5.1 ^{30}Si isotope depth profiles for implanted polycrystalline Si_3N_4 films before and after annealing for 1 h, 2 h, and 5 h at 1700 °C in nitrogen as measured with SIMS.

5.2. Measurements with Isotope Heterostructures

Due to the less convincing results of the last section, other straightforward experimental methods were applied in order to quantify self-diffusivities. Successful experiments became possible with isotope heterostructures. The production of such a layer system is explained in section 3.2 and a schematic sketch is shown in Figs. 3.1 and 5.2. Four different types of heterostructures were produced, which are given in Tab. 5.1. Type A and type B heterostructures are of the form $Si_3{}^{14}N_4/Si_3{}^{15}N_4/Si_3{}^{14}N_4$. They contain silicon with a natural isotope composition over the whole film thickness, while the middle layer II is enriched with the rare nitrogen isotope ^{15}N. Type C and D heterostructures of the form $^{28}Si_3{}^{14}N_4/Si_3{}^{15}N_4/^{28}Si_3{}^{14}N_4$ are additionally enriched with ^{28}Si in layer I and III. Here, the layer with the natural isotope concentration (layer II) is used as the tracer layer. During annealing, diffusion of the isotopes from layer II into the layers I and III is occurring. After deposition, the heterostructures are amorphous. In order to perform diffusion experiments in polycrystalline films, the as-deposited heterostructures were annealed for 2 h at 1500 °C, which leads to in-situ crystallization of the heterostructures (type A and C). This serves as a

starting state to investigate diffusion in polycrystalline Si_3N_4. Up to now, self-diffusion experiments with isotope heterostructures were carried out only on a very limited number of materials, namely Si [Bra98], Ge [Fuc95], SiC [Rus04, Jan04], and GaAs [Wan96] and related materials [Amb98, Bra99a, Bra99b, Bra00, Bra01]. In all cases, the structures were produced by molecular beam epitaxy or gas phase epitaxy, since the aim of these investigations was the investigation of diffusion in the single crystalline state. For amorphous or polycrystalline isotope heterostructures there exist only sporadic publications on FeZr [Gup04a, Gup04b], NiZr [Spe96], boron [Bak96], and TiB_2 [Sch03][*].

Table 5.1 Different types of Si_3N_4 isotope heterostructures on SiC substrates used in this study.

Type	Form	State	Layer thickness
A	$Si_3{}^{14}N_4/Si_3{}^{15}N_4/Si_3{}^{14}N_4$	polycrystalline: 70 % α + 30 % β phase	350 nm/60 nm/600 nm
B	$Si_3{}^{14}N_4/Si_3{}^{15}N_4/Si_3{}^{14}N_4$	amorphous	125 nm/30 nm/300 nm
C	$^{28}Si_3{}^{14}N_4/Si_3{}^{15}N_4/^{28}Si_3{}^{14}N_4$	polycrystalline: α phase	280 nm/22 nm/500 nm
D	$^{28}Si_3{}^{14}N_4/Si_3{}^{15}N_4/^{28}Si_3{}^{14}N_4$	amorphous	280 nm/22 nm/500 nm

Elemental and isotope composition of the as-sputtered heterostructures was measured with n-RBS, as illustrated for a type A heterostructure in Fig. 5.2. The simulation of the n-RBS profile with the computer code RUMP [Doo86] demonstrates that the film consists of stoichiometric Si_3N_4. The homogeneous depth distribution of Si and the alternating distribution of ^{14}N and ^{15}N film components are clearly visible. After crystallization, a mixture of the polymorphic modifications α–Si_3N_4 (~ 70 vol. %) and β–Si_3N_4 (~ 30 vol. %) are formed for type A heterostructures (see section 8.1). In contrast, for type C heterostructures nearly pure α–Si_3N_4 crystallizes, with a β–Si_3N_4 fraction below 3 %. The higher amount of the α modification which is formed during the crystallization process can be attributed to a higher amount of oxygen to be present in the heterostructures of type C compared to type A (only 0.1 at.%, as measured by n-RBS), which stabilizes the α modification as known from literature [Ril00].

Fig. 5.3(a) shows ^{15}N isotope depth profiles in the vicinity of layer II, as obtained from SIMS analysis of a type A heterostructure in the as-deposited state, after annealing for 2 h at 1500 °C (crystallization), and after additional diffusion annealing at temperatures of 1330 and 1700 °C. A clear broadening of the starting profile is observed. Assuming a step function for the interfaces in the as–deposited structure, profiles broadened after annealing can be described by Eq. (3.5). Diffusivities in the range between 1200 and 1700 °C are

[*] The measurements on TiB_2 were realized also by the present author.

obtained by least-squares fitting. In Fig. 5.3(b) depth profiles obtained with NRRA are shown for comparison. Here, also a clear broadening of the starting profile is observed due to diffusion, but with an asymmetric profile shape which is caused by a decrease of the depth resolution of the NRRA method with increasing depth as a result of energy straggling of the proton beam. Least-squares fitting of the NRRA data leads to a deviation of the fit from the experimental data for depths larger than 450 nm. For diffusivity determination only the left-hand part of the curves is used. In order to quantify also Si diffusivities, analogous measurements were carried out on isotope heterostructures of type C. The determined Si and N self-diffusivities are given in Fig. 5.6 and 5.7.

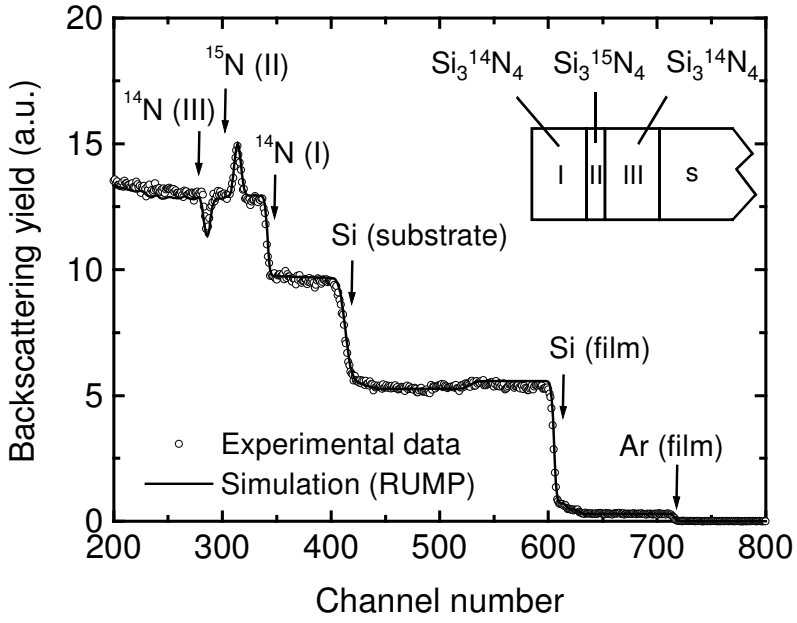

Figure 5.2 n-RBS spectrum of an as-deposited $Si_3{}^{14}N_4/Si_3{}^{15}N_4/Si_3{}^{14}N_4$ isotope heterostructure (type A) deposited on a Si substrate (s). Arrows indicate the film surface and the substrate interface for Si and the sequence of ^{14}N (I), ^{15}N (II), and ^{14}N (III) film components, as illustrated in the inset. The simulation of the spectrum with the computer code RUMP [Doo86] is also shown. High channel numbers correspond to high energies of the scattered helium ions.

In addition to the diffusion measurements on polycrystalline samples, experiments on amorphous samples were carried out. Here, the depth profile in the as-deposited state is used as starting profile. The presence of the amorphous state was checked before and after diffusion annealing with XRD. All samples were pre-annealed for 2 h at 1200 °C prior to the diffusion anneals. In Fig. 5.4 the broadening of a ^{30}Si depth profile is exemplarily illustrated for a type D heterostructure in the as-deposited state and the same structure annealed at 1200 °C for 143 h. Since for the depth profiles in the amorphous state very small diffusion lengths between 9 and 20 nm occur, the measured profiles were deconvoluted for diffusivity determination, using the MRI program of S. Hofmann [Hof00].

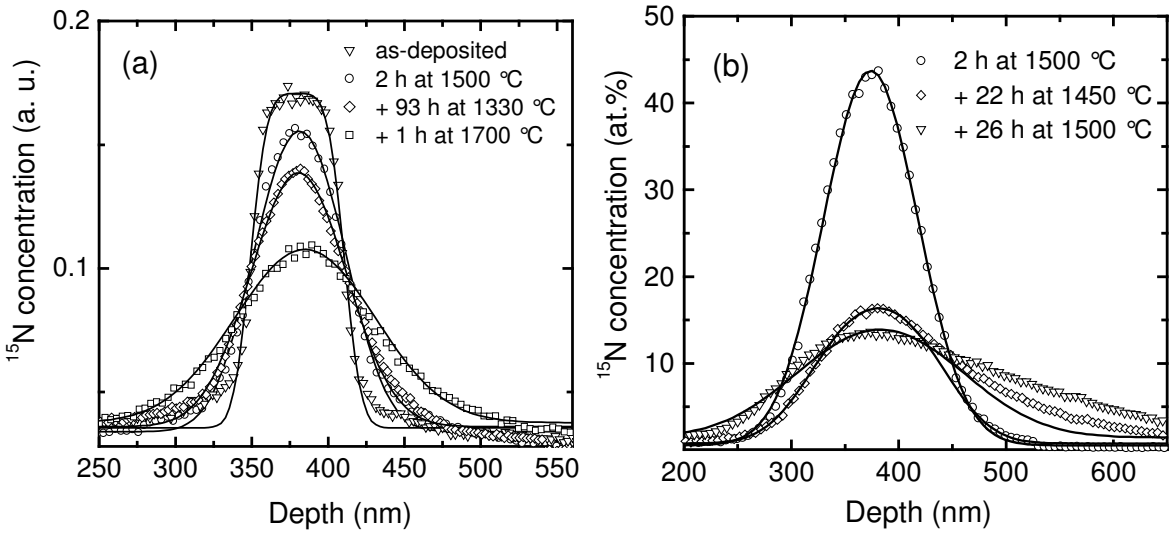

Figure 5.3: ^{15}N depth profiles for $Si_3{}^{14}N_4/Si_3{}^{15}N_4/Si_3{}^{14}N_4$ isotope heterostructures of type A after pre-annealing for 2 h at 1500 °C (crystallization) and after additional diffusion annealing, as obtained by **(a)** SIMS and **(b)** NRRA. The lines correspond to a fit of the experimental data to Eq. (3.5).

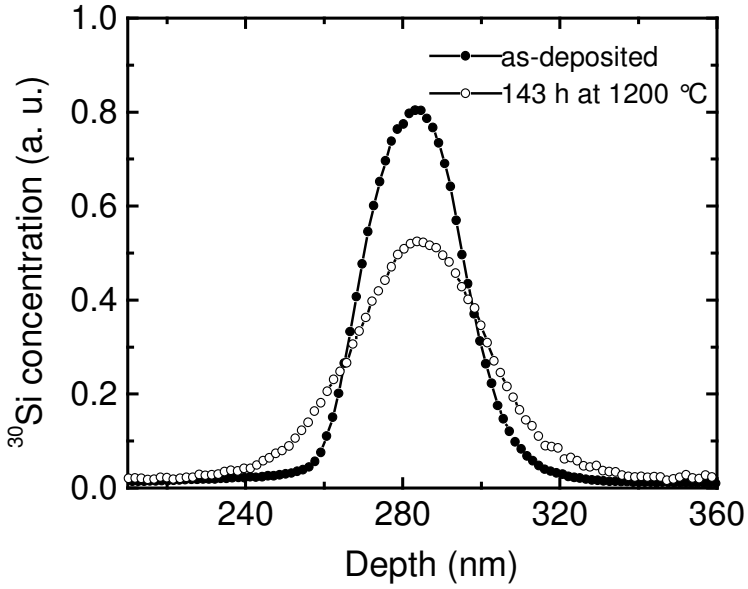

Figure 5.4: ^{30}Si SIMS depth profiles of an as-deposited $^{28}Si_3{}^{14}N_4/Si_3{}^{15}N_4/^{28}Si_3{}^{14}N_4$ isotope heterostructure (type D) and the same structure annealed for 143 h at 1200 °C in N_2, respectively.

5.3. Measurements with the Gas Exchange Method

In order to determine N self-diffusivities, complementary experiments were carried out in silicon nitride films with the gas exchange technique. Here, tracer deposition is achieved by annealing isotopically enriched homogeneous $Si_3{}^{15}N_4$ films in a $^{14}N_2$ atmosphere. In Fig. 5.5 the depth profiles of ^{14}N, ^{15}N, and ^{30}Si, as obtained by SNMS, are shown for an as-crystallized film and the same film additionally diffusion annealed at 1700 °C for 4 h. The

mutual exchange of both nitrogen isotopes is clearly visible, whereby the concentration of Si is unchanged. The diffusivities are extracted by fitting the nitrogen depth profiles to Eq. (3.7). In addition to the diffusivities, also the so-called surface exchange coefficients, k_s, are determined, which are a measure for the adsorption and dissociation of the N_2 molecule at the film surface, and the incorporation of N into the lattice. Data were obtained in the temperature range between 1600 and 1700 °C and are also given in Fig. 5.6.

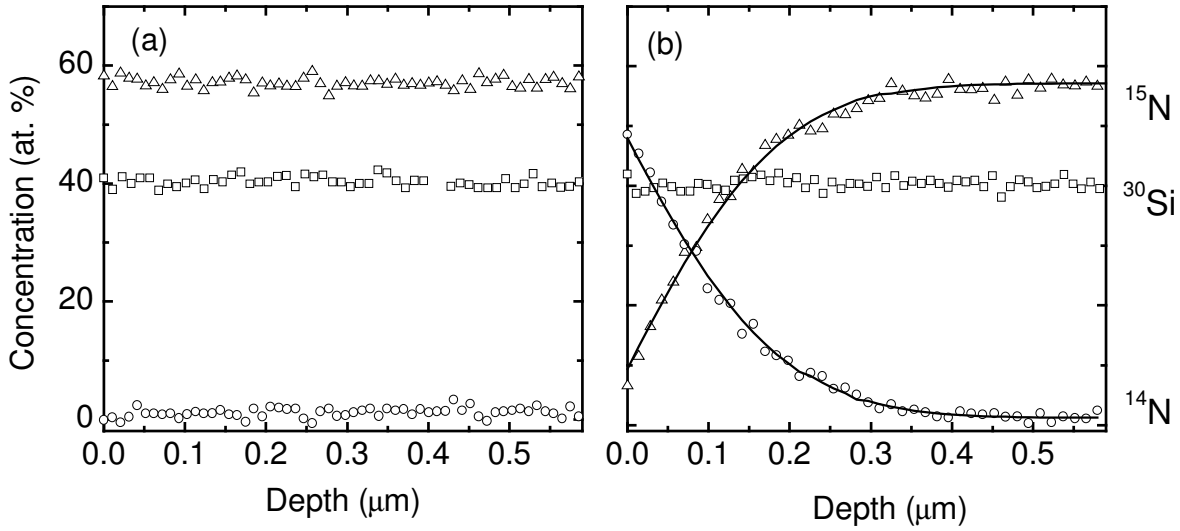

Figure 5.5 ^{14}N, ^{15}N, ^{30}Si depth profiles as obtained by SNMS on a polycrystalline $Si_3{}^{15}N_4$ film after **(a)** crystallization at 1500 °C and **(b)** additional diffusion annealing for 4 h at 1700 °C in an $^{14}N_2$ atmosphere. The lines correspond to a fit of the experimental data to Eq. (3.7).

5.4. Temperature Dependence of the Self-Diffusivities

In Fig. 5.6 the nitrogen self-diffusivities in polycrystalline films as obtained from the analysis of all experiments are presented as a function of reciprocal temperature. The experimental error of the diffusivities was determined to be about 50 % and is mainly caused by the accuracy of the depth measurement of the SIMS crater and by the averaging of several measurements carried out on one sample (typically 2-3). Very low diffusivities down to 10^{-23} m^2/s are obtained in the temperature range between 1200 and 1700 °C. These values are typically several orders of magnitude lower than for metals [Phi91] (e. g. the self-diffusivity of vanadium is about five orders of magnitude higher than the constituents of silicon nitride at 1700 °C, while the melting and decomposition temperature of both materials coincide at 1900 °C). The data obtained by different methods of tracer deposition (gas exchange, isotope heterostructures) and methods of depth profiling (SIMS, SNMS, NRRA) coincide within estimated errors. Only small differences were observed for the diffusivities obtained from heterostructures of type A (mixture of α–Si_3N_4 and β–Si_3N_4) and of type C (pure α–Si_3N_4) at high temperatures. Both datasets can be described by Arrhenius equations (Eq. 4.3) with a single activation enthalpy of $\Delta H^D = (4.9 \pm 0.4)$ eV and of $\Delta H^D = (5.2 \pm 0.4)$ eV. The corresponding pre-exponential factors are determined to be

D_0 = 1 x 10^{-6} m^2/s and D_0 = 2.5 x 10^{-5} m^2/s, respectively. The error attributed to D_0 is about one order of magnitude (see Appendix/Tab. B.2). These results imply that the presence of two polymorphic phases is reflected only weakly in the diffusion data, as indicated by only five times higher diffusivities for the films composed of pure α–Si_3N_4, which is close to the limit of estimated errors. However, theoretical calculations on the formation enthalpy of neutral nitrogen vacancies in Si_3N_4 of 3.1 eV (β-Si_3N_4) and 3.8 eV (α-Si_3N_4) [Tan02] support a slightly higher activation enthalpy of self-diffusion in α-Si_3N_4, if a vacancy mechanism is assumed. The question whether the small differences in the diffusion data are due to the presence of different modifications or due to a different oxygen impurity level has to be clarified with further experiments.

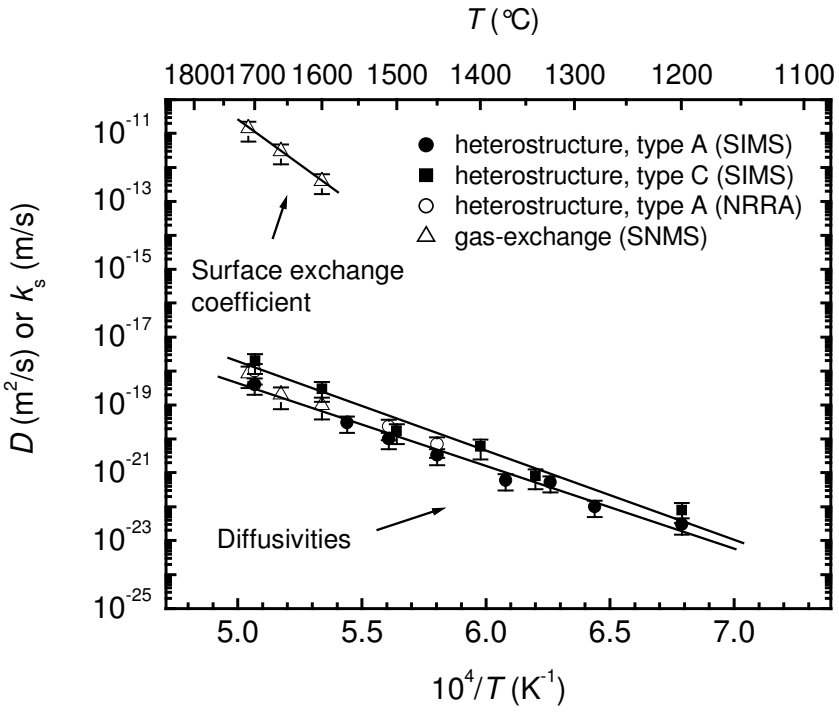

Figure 5.6 N Diffusivities in polycrystalline Si_3N_4 films as a function of reciprocal temperature. Also shown are surface exchange coefficients as obtained by the gas exchange experiments.

Both successful tracer methods used in this study (isotope heterostructures and gas exchange) differ mainly in the attainable temperature range. Using isotope heterostructures, diffusivities can be determined in a wider temperature range (1200 - 1700 °C). Without additional excitation of the dissociation of the N_2 molecule (e. g. by glow discharge) the gas exchange method enables a measurement only in a narrow temperature range from 1600 - 1700 °C. Gas exchange annealing of the films at temperatures below 1600 °C (e. g. 63 h at 1400 °C) did not result in a measurable enrichment of the ^{14}N isotope in the film. This is reasoned by the fact that surface exchange and diffusion are two successive processes, where the slowest one is rate limiting. At high temperatures the diffusion process is rate limiting so that a measurable diffusion depth profile is formed. With decreasing temperature the process of surface exchange slows down faster than the diffusion process

due to the higher activation enthalpy (about 10 eV compared to about 5 eV), as illustrated in Fig. 5.6. At temperatures well below 1600 °C a crossover from diffusion to surface exchange as the rate limiting process takes place. As obvious from Eq. (3.7), a sufficiently low ratio of the quantity $k_s^2\, t/D$ results in the disappearance of the diffused ^{14}N atoms in the ^{14}N background concentration of the $Si_3{}^{15}N_4$ film. These findings clearly show that an isotope heterostructure provides an excellent opportunity to measure N diffusivities over a large temperature range, because no surface exchange effects are present.

The isotope heterostructures of type C and D enabled the simultaneous determination of Si and N diffusivities during the a single measurement. The results for the polycrystalline and for the amorphous state are shown in Fig. 5.7. The Si and N diffusivities are identical within error limits. Least-squares fitting of a unique Arrhenius straight line to the diffusivities in polycrystalline Si_3N_4 leads to an activation enthalpy of $\Delta H^D = (5.0 \pm 0.3)$ eV and a pre-exponential factor of $D_0 = 6 \times 10^{-6}$ m^2/s, which are identical (within errors) with the parameters obtained from fitting of the N diffusivities only. Using Eq. (4.6), the entropy contribution to self-diffusion, ΔS^D, can be estimated from the pre-exponential factors. A value of about $\Delta S^D \approx 0 - 4\ k_B$ is found for the diffusion in polycrystalline Si_3N_4. These values are in the same range as those found for metals and intermetallic compounds [Phi91], but it is smaller, or at least at the lower limit of the values found for semiconductors like Si, Ge and GaAs in the order of 5 - 10 k_B [Bra98, Fuc95, Wan96, Fra84, Pal81]. For these semiconductors the high entropy values are explained by the presence of point defects extended over several neighbouring lattice sites [See68, Fra92]. From these findings it can be concluded that nitrogen is diffusing in polycrystalline Si_3N_4 films conventionally via localized point defects like vacancies or interstitials. For further discussion see also section 4.4.

The present results on N diffusion in polycrystalline material are in contrast to the data reported by Kijima and Shirasaki [Kij76] in 1976 on reaction bonded silicon nitride powders, which are also shown in Fig. 5.7 for comparison. They used a gas-solid exchange method and measured the uptake of ^{15}N gas in α-Si_3N_4 and β-Si_3N_4 powders in a relatively limited temperature range between 1200 and 1400 °C. Volume diffusivities were determined by re-scaling the data on powders with different particle size. Unexpected combinations and extremely large differences between the activation enthalpies (2.4 and 8.1 eV) and pre-exponential factors (1.2×10^{-16} and 1.9×10^2 m^2/s) were found for the two Si_3N_4 polymorphs. The present results are in contradiction to these data. We tentatively attribute the differences between the data of Kijima and ours to a different kind of material investigated (with slightly different composition) and to different levels of impurities present in the samples. This is again supported by theoretical calculations of the formation enthalpy of neutral nitrogen vacancies in Si_3N_4, ΔH^V, which were carried out by Tanaka et al. in the N-rich and in the Si-rich limit [Tan02]. A strong variation of ΔH^V between 6.5 eV and 3.8 eV for α-Si_3N_4 and between 5.5 eV and 3.1 eV for β-Si_3N_4 was obtained for the N-rich and the Si-rich limit, respectively. This indicates a strong dependence of the diffusivities on the exact chemical composition and the chemical environment of the whole

system, if it is assumed that the diffusion process is based on a vacancy mechanism. The relatively low value for the activation enthalpy of diffusion $\Delta H^D = \Delta H^V + \Delta H^M \approx 5$ eV (ΔH^M: enthalpy of migration) found in this study indicates a chemical composition of Si_3N_4 at the Si-rich limit.

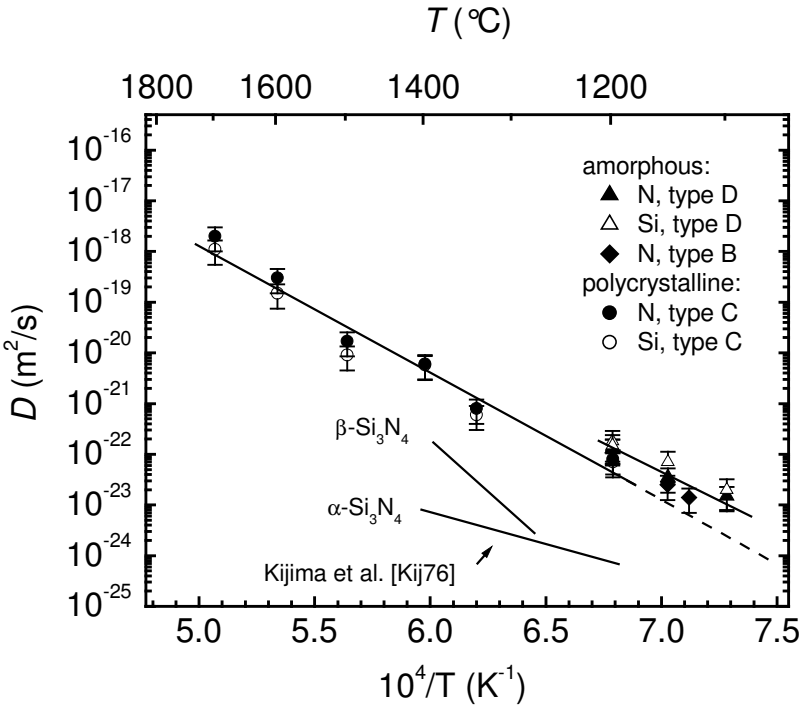

Figure 5.7 Diffusivities of N and Si in Si_3N_4 as a function of reciprocal temperature for polycrystalline and amorphous isotope heterostructures, as measured with SIMS. The type of heterostructure is indicated. Also shown are the N diffusivities measured by Kijima and Shirasaki [Kij76].

The Si and N diffusivities in amorphous Si_3N_4 are also given in Fig. 5.7 and can be also fitted with a unique Arrhenius line with $\Delta H^D = (4.5 \pm 1.0)$ eV and $D_0 = 4 \times 10^{-7}$ m^2/s. Nevertheless, it was possible to quantify Si and N diffusivities in the amorphous state only in a limited temperature range between 1100 and 1200 °C. For higher temperatures the films crystallize and for lower temperatures diffusivities below 10^{-23} m^2/s are present, which cannot be determined reliably with the present method. In order to measure those lower diffusivities, investigations with neutron reflectometry might be a useful approach [Gup04a]. As obvious from Fig. 5.7, the diffusivities in the amorphous state are higher only by a factor of five than the diffusivities in the polycrystalline state at 1200°C (and also at extrapolated lower temperatures), while only a slightly smaller value of ΔH^D (4.5 eV instead of 5 eV) is present. This points to a similar diffusion mechanism in the crystalline and amorphous state via point defect-like vehicles like e. g. quasi-vacancies. Indications for a collective motion of atoms are not found. The enhanced diffusion in the amorphous state might be reasoned by the fact that additional free volume is present in comparison to the crystalline state, making the motion of atoms more easy. Such free excess volume may be produced by the deposition procedure of the amorphous films with magnetron sputtering.

The slightly lower activation enthalpy of the diffusivities in the amorphous state might be an indication for excess free volume. However, this interpretation should not be overestimated, because the experimental data were measured in a small temperature range and consequently have large errors. Note that a common fitting of the diffusivities of silicon nitride and of Si-C-N ceramics as carried out in section 4.2 leads to higher values of ΔH^{D}. However, the error limits attributed to each data point allow both interpretations.

It has also to be noted that the experimental results on amorphous Si_3N_4 obtained in this study exhibited a N diffusivity which is about eleven orders of magnitude lower compared to theoretical values calculated with molecular dynamics by Matsunaga and Iwamoto [Mas01, Iwa01], emphasizing the importance of further (theoretical and experimental) investigations in this system. Through the present investigations on Si_3N_4, it was possible to realize one of the very first experiments which was successful in determining the self-diffusivities in amorphous and polycrystalline covalent materials in direct comparison.

In order to search for a reliable self-diffusion mechanism in silicon nitride, it should be kept in mind that similar or identical diffusivities in binary compounds indicate a common diffusion mechanism for both elements. Assuming a vacancy mechanism, a statistical motion of a vacancy via nearest neighbour jumps between the sub-lattices formed by the two types of elements is very unrealistic, because each moving vacancy would leave behind a tail of anti-site defects. In order to enforce the equality of the diffusivities, migration via the same defect is a possibility, while the long range order is being restored. For instance, one could think of vacancy pairs ($V_N V_{Si}$). However, it should be kept in mind that the present knowledge of point defects in crystalline Si_3N_4 is extremely poor [Ril00]. Consequently, a further discussion is suspended until sufficient theoretical and experimental data are available on what is the dominating defect in Si_3N_4.

5.5. Influence of Grain Boundaries

In order to address the transport along grain boundaries, which are present in polycrystalline films and which might influence the diffusion process, the following comments are made. Due to the relatively small penetration depth of the diffusion profiles of less than 50 nm and due to an average grain diameter of about 100 nm, grain boundary transport does not contribute to the observed broadening of layer II. Possible grain boundary diffusion profiles are masked by the natural background of ^{15}N and ^{30}Si isotopes in layers I and III. However, the influence of grain boundaries is indirectly reflected in the depth profiles at high temperatures (> 1500 °C). In Fig. 5.8(a) SIMS ^{15}N depth profile of a type C heterostructure, which was annealed at 1600 °C for 37 min, is plotted over the whole film thickness. In addition to the broadened isotope enriched layer, a strong increase of the ^{15}N concentration is observed close to the surface. Similar observations were made using SNMS or NRRA for depth profiling, and also for the ^{30}Si tracers. A plausible explanation of this observation can be found if it is assumed that diffusion along grain boundaries takes place with a diffusivity much higher than volume diffusivity. Consequently, during

annealing a significant amount of ^{15}N tracer can be transported along the grain boundaries from the tracer layer to the sample surface. There, the adsorbed tracer atoms are homogeneously distributed over the surface due to fast surface diffusion. From this reservoir the tracer can now penetrate again into the grains of the film by volume diffusion. In principle, the tracer reservoir at the surface is a continuous source which is supplied from the ^{15}N reservoir in the interior of the heterostructure. The depth profile can be fitted with a combination of Eqs. (3.5) and (3.7) using the same volume diffusivity, D, as a fitting parameter. The obtained values of D are identical within errors to those derived by the conventional fitting procedure as explained in section 5.3. The number of tracer atoms, which is obtained by integrating the diffused isotope profile over depth, is identical to that one obtained for the implantation profile. Using an average grain diameter of 100 nm and a width of the grain boundary of 1 nm, grain boundary diffusivities of $D_g \approx 10^4 D_V$ can be assessed from $A_g D_g^{1/2} \approx A_V D_V^{1/2}$, which is reasonable. Here, A_V and A_g are the cross-section areas of a grain and of a grain boundary, respectively.

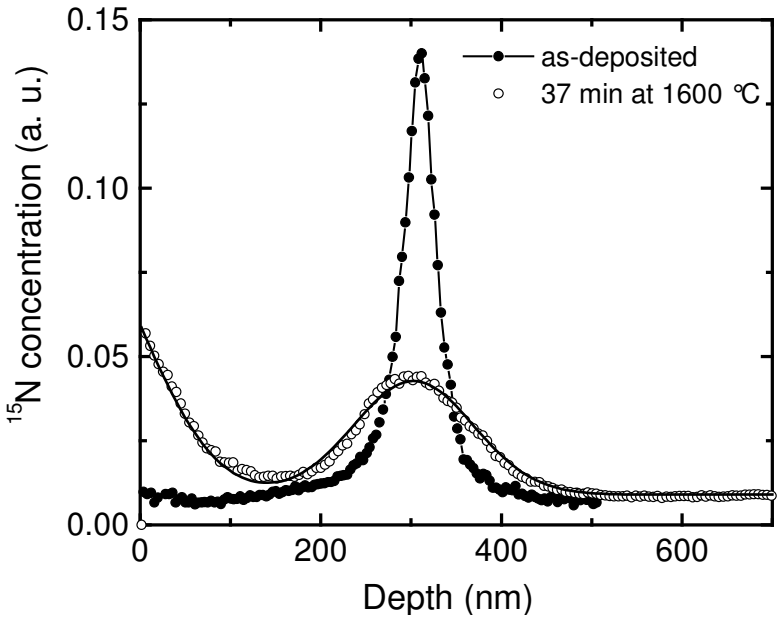

Figure 5.8 ^{15}N depth profile of a type C isotope heterostructure after annealing for 37 min at 1600 °C as obtained by SIMS. The lines correspond to a fit of the experimental data to a combination of Eqs. (3.5) and (3.7). For more details see text.

6. Atomic Motion and Defect Interaction of Hydrogen in Hydrogenated Si-C-N Based Materials

During the last years, there arose a considerable experimental and theoretical interest in the migration behaviour of hydrogen in hydrogenated* amorphous and polycrystalline silicon [Bey03, Car78, Pea91, Brn99, Che94, Van95, Jac92, Str87, Yu03, Fed02, Bis98] and related materials [Shi99, Arn93, Cau78, Cau93]. This interest is motivated mainly by two reasons: (1) hydrogen is an essential constituent of the amorphous network structure of these materials, responsible for reduction of stress and the formation of a metastable equilibrium state. Since hydrogen diffuses at relatively low temperatures compared to the other elements, its dynamic behaviour is very important for the thermal stability of the material. (2) Intrinsic defects of the material like dangling bonds play a decisive role for the application of these materials as electronic and optoelectronic components and limit their performance as devices. Hydrogen is able to passivate these defects and thus improves the quality of devices. Since the defect densities are strongly correlated with the atomic mobility of hydrogen, investigations of the diffusion properties of hydrogen in these materials may reveal information on the defect physics which is of crucial importance for any technological application. For reviews on that topic see Refs. [Bey03, Str91].

In contrast to silicon, quantitative measurements on hydrogen diffusion in related compounds, like SiC or Si_3N_4 are extremely limited [Yu02, Arn93], despite of their growing importance in semiconductor technology (see section 2.2). A relatively new material in this framework is amorphous Si-C-N, which is hoped to combine the properties of SiC and Si_3N_4. For electronic applications, Si-C-N is investigated due to its adjustable band gap for possible applications as a wide band gap semiconductor [Che98, Par03, Lin97] in thin film transistors [Lav04] and in field emission displays [Lin02]. Also under investigation is the material as tuneable electrical conductor due to the variation of the electrical resistance over 15 orders of magnitude [Her01, Ali02, Tra02]. Each of the mentioned properties depend on the presence and the mobility of hydrogen and its interaction with defects.

In order to get insight into the atomic transport properties of hydrogen in multi-component Si-C-N based materials, systematic investigations of hydrogen tracer diffusion were carried out in various materials: magnetron sputtered amorphous and crystalline Si_3N_4 films, magnetron sputtered amorphous SiC and Si_2CN_4 films, and precursor-derived amorphous Si-C-N and Si-B-C-N. In addition, reference experiments are done on CVD derived B-N-C films and glassy carbon, in order to explain the diffusion mechanism in Si-B-C-N. A model is presented which may account for the hydrogen diffusion in all these materials.

* The term “hydrogenated” means that several atomic per cent of hydrogen are incorporated in the amorphous network structure by binding to the host atoms.

6.1. Diffusion of Hydrogen in Si_3N_4 Films

About 1 μm thick amorphous and polycrystalline films of Si_3N_4 were extensively investigated as a model system for the diffusion of hydrogen in a two component material. Measurements as a function of temperature, pre-annealing state, and hydrogen content were carried out to explain the basic features of hydrogen motion. For studying the hydrogen diffusion, two different methods of tracer deposition were applied and compared, ion implanted ^2H isotopes and $^1H/^2H$ gas exchange. Isotope depth profile analysis was carried out by SIMS, detecting H^+ ions. Several different types of samples were investigated in this study: amorphous films in the as-deposited state, amorphous films pre-annealed for 2 h at 1000 °C or for 2 h at 1200 °C in N_2 (980 mbar), amorphous films pre-annealed for 2 h at 1000 °C in a mixture of N_2 - 6 % H_2 , and polycrystalline films pre-annealed for 2 h at 1500 °C in N_2 (980 mbar). The pre-annealing processes were carried out in order to allow a relaxation of the as-produced amorphous state and to establish a metastable equilibrium, to charge the films with hydrogen, or to crystallize the films. The hydrogen content was determined by NRRA to be between 0.2 and 0.5 at.% for the films pre-annealed in N_2 (low concentration) and 2.6 at.% for films pre-annealed in N_2 - 6 % H_2 (high concentration), respectively (see Appendix/Tab. B.3).

6.1.1. Amorphous Si_3N_4 Films

Fig. 6.1 shows typical SIMS depth profiles of ^2H implanted in amorphous Si_3N_4 before and after annealing at different temperatures. The concentration which is measured by SIMS is given as $[^2H_{tot}]$ and $[^1H_{tot}]$. The implantation profile exhibits a nearly Gaussian shape with a projected range of $R_p = 101$ nm and a width of $\Delta R_p = 38$ nm. For the annealed films a broadening of the profile is observed corresponding to diffusion. For profiles with a large broadening, like for the film annealed at 1000 °C, a stationary cusp is superimposed on the Gaussian profile around 100 nm, similarly to the observations of N diffusion in Si-B-C-N, as explained in section 4.2. This cusp can again be attributed to an immobilization of the tracer due to the implantation damage. Only a fraction of the tracer is mobile and diffuses into the sample (Gauss-like diffusion profile). In contrast to ion implanted nitrogen, the trapping effect is less pronounced here for the light hydrogen ions, since a smaller number of defects is created during implantation.

The diffusivity determination and interpretation of the measurements are carried out under the assumption that a trap-limited diffusion mechanism is operating[*], where the motion of interstitial-like mobile H atoms is connected with the formation of immobile complexes of the form HR_i at trapping centres R_i intrinsic to the solid (e. g. dangling bonds) and subsequent dissociation of these complexes. These intrinsic traps should not be confused with extrinsic traps R_e, which are additionally present and result from the implantation damage. An outline of the theory adapted to the special experimental

[*] A justification for that assumption is given later on.

conditions of this study is given in Appendix A. Diffusivity determination is achieved in two different ways:

(a) The diffusivities were determined by a comparison of the experimental data to computer calculations based on the framework of trap-limited diffusion of ion implanted deuterium tracers as given in Eqs. (A.2).

(b) The diffusivities were determined by a least-squares fit of the experimental data to the analytical solution of the diffusion equation (A.4), assuming a moderately high dissociation rate and a sink at the surface, which is given by Eq. (3.4). Here, the fitting procedure is limited to a depth range larger than 170 nm, which means that the part of the profile where the influence of the implantation damage is reflected in the depth profiles, is neglected.

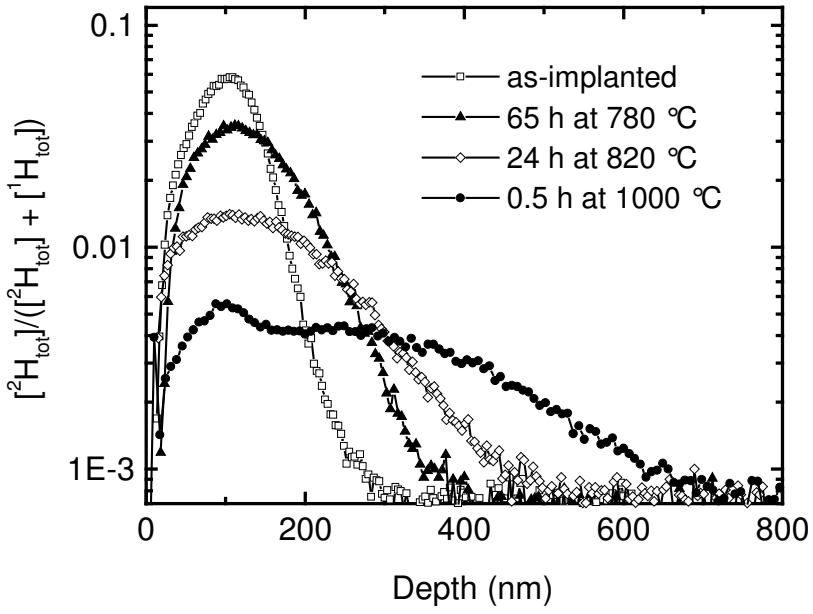

Figure 6.1 Typical diffusion profiles of ion implanted ^{2}H tracer in amorphous Si_3N_4 (pre-annealed at 1200 °C in N_2) after annealing at elevated temperatures, as measured by SIMS.

In case of amorphous Si_3N_4, only one type of intrinsic trap R is necessary to understand the diffusion process. Diffusivity determination is illustrated in the case of a sample annealed at 1000 °C (Fig. 6.2). As initial concentrations ($t = 0$) the following parameters are used: $[^1HR]_0 = 5 \times 10^{26}$ atoms/m^3 is the hydrogen concentration measured with NRRA, $[^1H]_0 = 1.3 \times 10^{24}$ atoms/m^3 is the concentration of free hydrogen which is formed for a constant number of given traps $[R]_0 = R_0 = 5 \times 10^{25}$ atoms/m^3. The values for $[^1HR_e]_0$, $[^2HR_e]_0$, and $[^2HR]_0$ are zero at the beginning of the diffusion process. As for implanted N in Si-B-C-N (section 4.1), the initial concentration of implanted deuterium is approximated with a Gaussian distribution, however, with $R_p = 101$ nm and $\Delta R_p = 38$ nm. The initial depth dependent concentration of extrinsic traps $[R_e]_0$ is again modelled theoretically with the program package SRIM-2003 as described in section 4.1, using $^2H^+$ ions implanted with

6.67 keV in Si_3N_4 with a density of 3.4 g/cm^3 (corresponding to $^2H_3^+$ molecule ions implanted with 20 keV).

In Fig. 6.2 a typical SIMS isotope depth profile, for a sample diffusion annealed for 6 and 30 min at 1000 °C is plotted together with the computer simulations. It is obvious that an excellent agreement between measured diffusion profiles and numerical simulations is obtained using values for the capture radius k, the dissociation rate of traps ν, the intrinsic diffusivity D_H, and the trap concentration R_0 which are given in the caption of Fig. 6.2, and which correspond to the limiting case of moderately high dissociation rates of the intrinsic traps ($0 << \nu/(k\ R_0) << 1$). For more details see Appendix A. For depth values larger than about 160 nm also a very good agreement between the measured profile and the analytical fitting curve is obtained. Thus, the hydrogen motion in amorphous Si_3N_4 can be described as a trap-limited process governed by an effective diffusivity, as defined by Eq. (A.5). A value of D_{eff} = 1.5 x 10^{-17} m^2/s is obtained with both methods. This demonstrates that the extrinsic traps have here again an significant influence on the form of the depth profiles, but not on the determination of the effective diffusivities and that the usage of the analytical solution is an adequate method to determine the correct diffusivities. A significant time dependence of the diffusivities was not observed for the temperatures and annealing times used in this study.

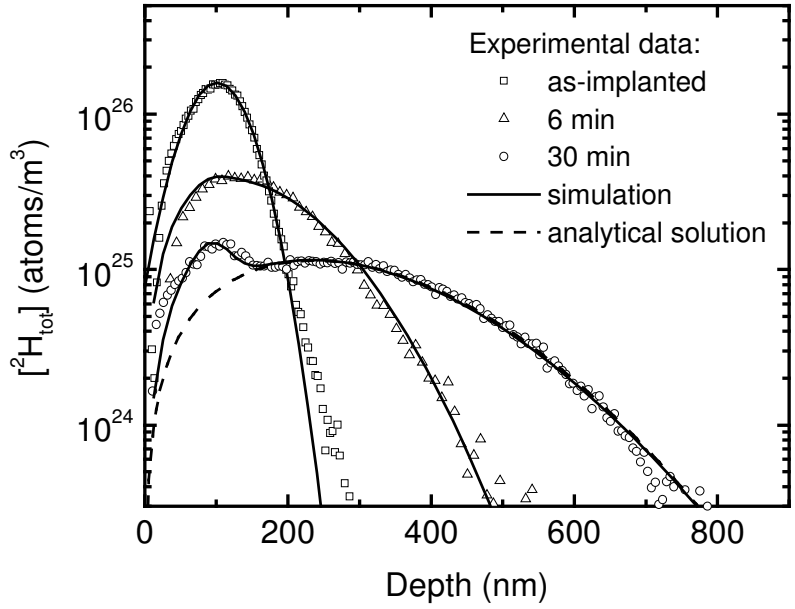

Figure 6.2 Typical diffusion profiles of ion implanted ^{2}H tracers in amorphous Si_3N_4 (pre-annealed at 1200 °C in N_2) before and after annealing for 6 and 30 min at 1000 °C in N_2. The ^{2}H background concentration was subtracted from the experimental data for a better comparison. The solid lines represent computer calculations based on the numerical solution of Eqs. (A.2), using the parameters R_0 = 5.0 x 10^{25} traps/m^3, k = 7.5 x 10^{-24} m^3/s, k_e = 2.5 x 10^{-29} m^3/s, ν = 1.0 s^{-1}, and D_H = 5.3 x 10^{-15} m^2/s.

Nevertheless, simulations with other combinations of values k, ν, D_H, and R_0, which result in the same effective diffusivity (see Eq. (A.5)) lead to identical depth profiles as long as the condition of sufficiently high dissociation is fulfilled and the trap concentration is not lower than 1 x 10^{25} m^{-3}.

In Fig. 6.3 the determined effective diffusivities of ^2H are shown as a function of reciprocal temperature for as-deposited films, and for films annealed at 1000 and 1200 °C in nitrogen, prior to tracer deposition and diffusion annealing. During the diffusion experiments the annealing temperatures never exceeded the pre-annealing temperature so that changes in microstructure were avoided. The deuterium tracer diffusivities for all three types of samples obey an Arrhenius law. The determined activation enthalpies of diffusion and pre-exponential factors do not vary with the pre-annealing temperature, resulting in values of $\Delta H^D \approx 3.4$ - 3.5 eV and of $D_0 \approx 4$ - 9 x 10^{-4} m^2/s (see Appendix/Tab. B.3). Consequently, micro-structural re-arrangements of the atoms, like relaxation or stress release which occur during the pre-annealing procedure do not significantly influence the atomic transport properties of hydrogen. Considering a trap-limited diffusion mechanism, this result shows that the concentration and type of traps are not influenced by possible atomic re-arrangement processes.

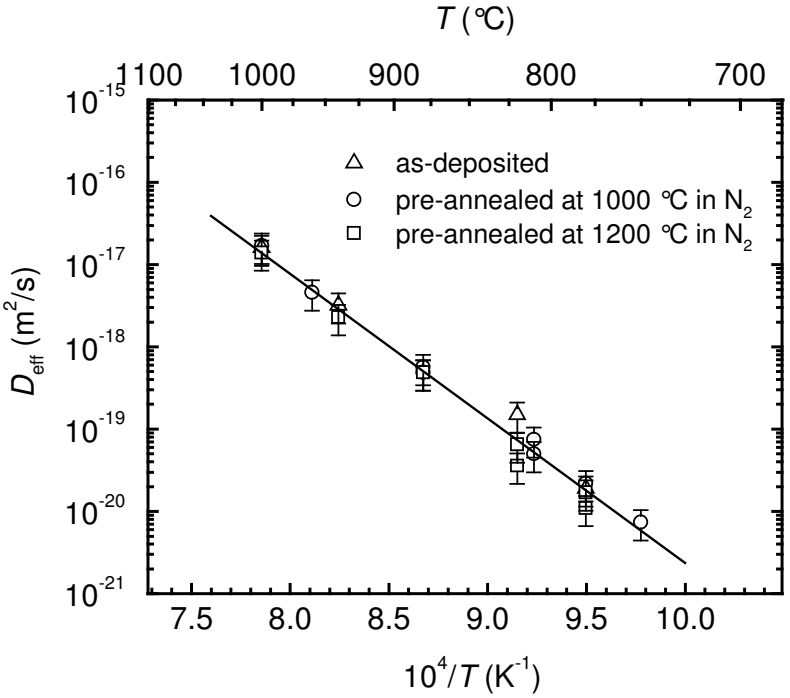

Figure 6.3 Effective diffusivities of ^2H in amorphous Si_3N_4 as a function of reciprocal temperature for as-deposited films and films pre-annealed for 2 h at 1000 °C and 1200 °C in N_2, respectively.

In Fig. 6.4 the temperature dependence of the effective diffusivities for the films pre-annealed at 1000 °C in N_2 are compared to the films pre-annealed at 1000 °C in N_2 - 6 % H_2. The hydrogen enriched annealing atmosphere results in a hydrogen charging of the

films which leads to an about seven times higher hydrogen content of about 2.6 at.%. The diffusivities of both sample series can be described by an Arrhenius behaviour, but significant differences arise for the pre-exponential factor and the activation enthalpy. These values are lower for the samples containing more hydrogen, where the activation enthalpy is decreased to 2.7 eV and D_0 by two orders of magnitude to $D_0 = 3 \times 10^{-6}$ m^2/s.

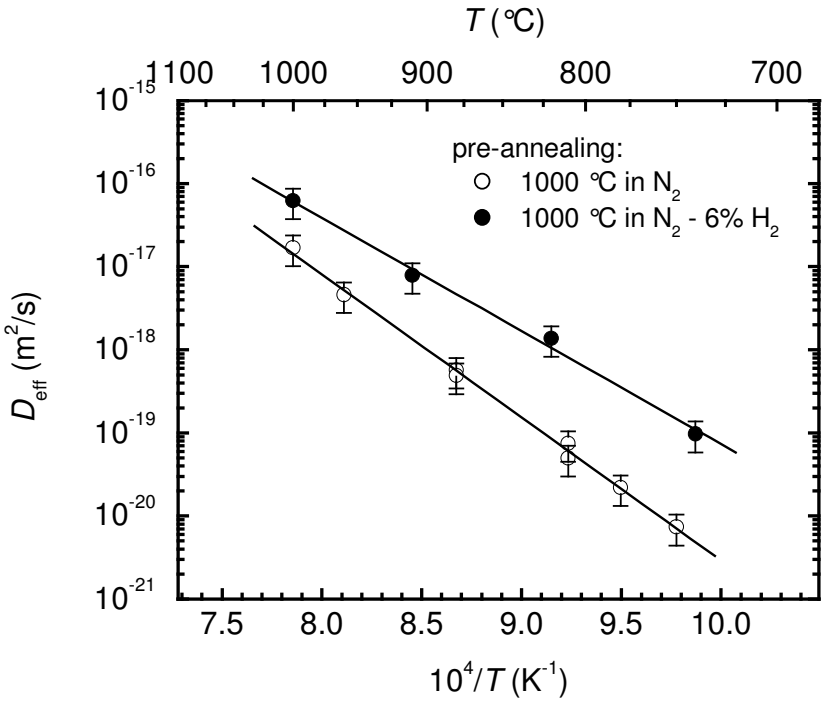

Figure 6.4 Effective diffusivities of ^{2}H in amorphous Si_3N_4 as a function of reciprocal temperature for films pre-annealed for 2 h at 1000 °C in N_2 and in N_2 - 6% H_2, respectively.

Often, diffusion measurements which are carried out with ion implanted tracers are criticized by the argument that the damage produced by the implantation process "disturbs" the real motion of atoms due to the interaction of the tracer with the extended defects. To check a possible influence of the implantation damage on the diffusivities, additional experiments were carried out on films pre-annealed at 1000 °C in N_2 - 6 % H_2 with the gas exchange technique. In Fig. 6.5(a) some typical depth profiles of this control experiment are displayed, wherefrom the diffusivities are extracted by fitting the data to Eq. (3.6). The diffusivities obey also an Arrhenius law with an activation enthalpy of $\Delta H^D = 2.6$ eV and a pre-exponential factor of $D_0 = 3 \times 10^{-6}$ m^2/s. These data are in good agreement with the diffusivities measured with the implantation technique and can be fitted with a unique Arrhenius straight line, as shown in Fig. 6.5(b). As a result, we find that the implantation damage does not influence the migration of hydrogen atoms. Therefore, the implantation technique can be considered as an adequate method to determine the correct diffusivities of hydrogen in these materials. The hydrogen atoms which are not trapped by the implantation damage with the defect concentration [R_e] diffuse nearly independently from the trapping centres with the same diffusivity as for the damage free case.

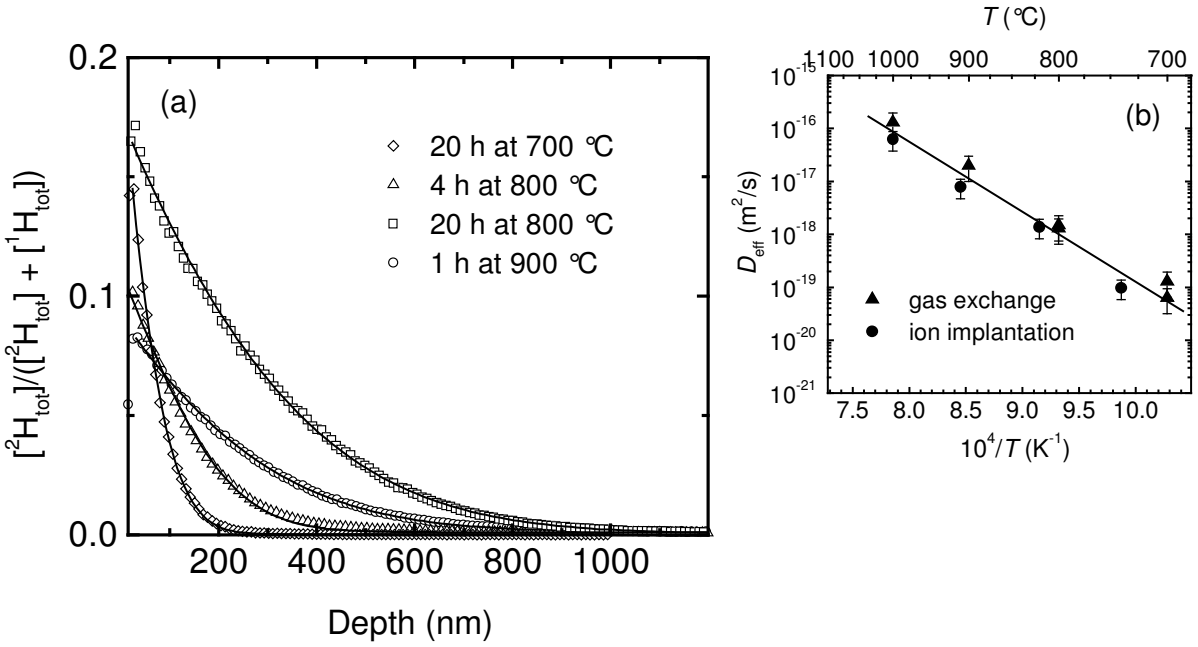

Figure 6.5 (a) Typical diffusion profiles of ^2H in amorphous Si_3N_4 (pre-annealed at 1000 °C in N_2 - 6 % H_2) as measured with SIMS after annealing at elevated temperatures using a gas exchange technique. The lines correspond to a least square fit of the experimental data to Eq. (3.6). **(b)** Effective diffusivities of ^2H in amorphous Si_3N_4 as a function of reciprocal temperature for films pre-annealed for 2 h at 1000 °C in N_2 - 6 % H_2 compared for ion implantation and gas exchange of the tracer isotopes.

The present depth profiles and diffusivities were described under the assumption of a trap-limited diffusion mechanism. This is supported by the following arguments: very high activation enthalpies of hydrogen diffusion (2.6 - 3.5 eV) were derived which are characteristic for this phenomenon and which are also observed for amorphous silicon (up to 2.4 eV) [Bey03] where this mechanism is well established. The same is true for impurity doped (e. g. B, Al) single crystalline silicon (~ 1.7 eV) [Pea91] and silicon carbide (~ 1.6 - 2.5 eV) [Jan01a, Jan01b]. In contrast, in undoped single crystalline silicon, hydrogen is diffusing via a direct interstitial mechanism with a low activation enthalpy of $\Delta H^D = 0.48$ eV, and a low pre-exponential factor of $D_0 = 9.4 \times 10^{-7}$ m^2/s due to the absence of trapping centres [Wie56, Pea91]. Further, hydrogen (and also deuterium), present in amorphous silicon nitride, is generally bound to the Si and N host atoms as demonstrated by FTIR [Rob94, Arn93, Kan87, Lus89]. Consequently, for hydrogen motion these bonds have to dissociate. Finally, the occurrence of non-Gaussian time dependent diffusion profiles as found in the polycrystalline state (see section 6.1.2) can be explained best under the assumption of a trap-limited diffusion mechanism, where interstitial-like mobile H atoms (^1H or ^2H) are temporarily trapped by intrinsic defects of the structure like dangling bonds. The intrinsic defects discussed here, which are homogeneously distributed over the whole film, should not be confused with the extrinsic defects produced by the implantation

damage in a limited depth range close to the surface, which have almost no influence on the diffusion process as shown for the present case.

According to Eq. (A.5), in case of moderately high dissociation, which is present in the amorphous state, the effective diffusivity is determined by the dissociation enthalpy of trapped hydrogen ΔH_d, which is a sum of the binding enthalpy of the HR complexes, ΔH_b, and the migration enthalpy of the free hydrogen atoms, ΔH_m, $\Delta H_d = \Delta H_b + \Delta H_m$ (see Fig. 6.6) and can be identified with the activation enthalpy of diffusion ΔH^D. The trapping centres can in principle be associated with both silicon (Si-) or/and nitrogen (N-) dangling bonds. Consequently, the migration of the ^{2}H tracer has to be connected with the dissociation of a Si-H or a N-H bond with a binding enthalpy of several eV and the formation of a mobile H species and a dangling Si- or N- bond due to Eq. (A.1). In order to have a hydrogen atom escape from a trap in the amorphous solid it is necessary to supply the dissociation enthalpy of the HR complex, ΔH_d (see Fig. 6.6(a)). After de-trapping the mobile ^{2}H tracer can migrate freely in a fast transport mode corresponding to an interstitial-like diffusion process with a low migration enthalpy ΔH_m until it is re-trapped again. In Ref. [Rob94] the energy levels of Si-H and N-H bonds in Si_3N_4 are calculated to be about -3 eV and -4 eV with respect to the value in free space. Since the maximum experimentally determined activation enthalpy of ΔH^D = 3.5 eV obtained for the samples with low hydrogen content exceeds the binding enthalpy of Si-H it becomes clear that the dissociation of N-H bonds should be the rate limiting step in this case.

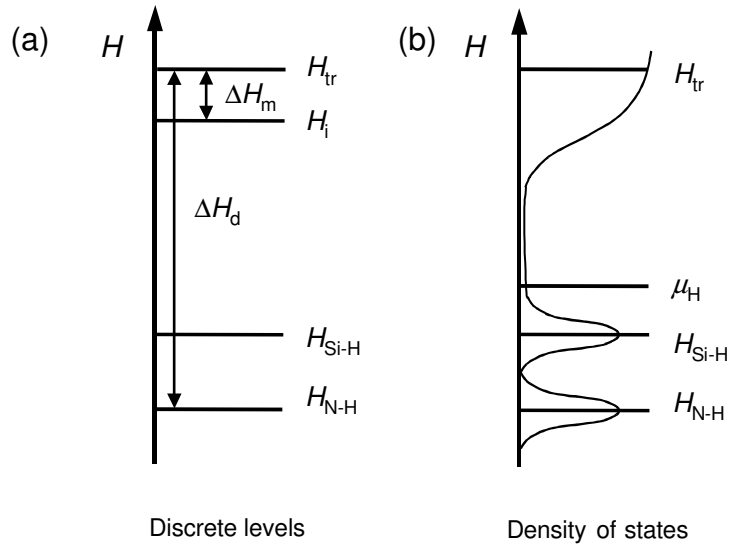

Figure 6.6 (a) Schematic sketch of the enthalpy levels assuming a trap-limited diffusion process in amorphous Si_3N_4. H_{RH} is the enthalpy level of hydrogen bound to a trap (R = Si or N atom), H_i is the enthalpy level of an interstitial-like hydrogen, H_{tr} is the enthalpy level of freely migrating hydrogen. The corresponding dissociation enthalpy, ΔH_d, and migration enthalpy, ΔH_m, are also indicated. **(b)** If a site energy distribution arises due to disorder, the process is described best by a hydrogen chemical potential μ_H.

A consequence of Eq. (A.5) is that the intrinsic hydrogen diffusivity D_H cannot be extracted from the experimental data because of the fact that different combinations of the quantities ν, k, R_0, and D_H, which are in principle unknown, result in the same effective diffusivity D_{eff}. This quantity might be orders of magnitudes lower compared to D_H, depending on the values of ν, k, and R_0. However, from the experimentally determined pre-factor D_0 it is possible to estimate the concentration of traps R_0 by Eq. (A.8) to $R_0 = \nu_0 / (4 \pi R_c D_0)$. An estimated value of $\nu_0 \approx 1 \times 10^{13}$ s^{-1} is used and the capture radius is usually set to a value in the same order of magnitude as the inter-atomic distance in the lattice of $R_c \approx 0.2$ nm. From these data a trap concentration of $R_0 \approx 10^{25}$ atoms/m^3 (error: $\log R_0 = \pm 1$) is derived, which is a quite reasonable value for the dangling bond concentration in Si_3N_4 films [Rob94].

For the films annealed in N_2 - 6 % H_2, containing 2.6 at.% of hydrogen, the activation enthalpy and the pre-exponential factor are strongly decreased compared to the nearly hydrogen free case. These findings can in principle be explained with Eq. (A.8) if two different type of traps are assumed to be present in Si_3N_4. In case of low H content, diffusion is controlled by deep traps (nitrogen dangling bonds) as indicated by comparatively large value of ΔH_d. If the hydrogen content is increased, the system re-arranges itself and the deep traps are saturated by the additional hydrogen present in the amorphous matrix and become ineffective. For a sufficiently high H concentration the rate limiting step is now the breaking of a Si-H bond, which is reflected in a reduction of the activation enthalpy. The lower pre-exponential factor indicates a decrease of the ratio $\nu_0 /(4 \pi R_c R_0)$. Since the frequency $\nu_0 \approx \nu_D$ and the capture radius R_c are relatively static material parameters for a given system, the lower pre-exponential factor should reflect an increase of the number of trapping centres R_0 (more shallow Si traps than deep N traps). Unfortunately, a high concentration of Si traps of $R_0 \approx 10^{27}$ m^{-3} (≈ 1 at. %) is calculated, which is not very realistic for a hydrogen content of almost 3 %.

Consequently, Eq. (A.8) already used for analysis has to be modified to explain the dependence on hydrogen concentration. For higher hydrogen concentrations the hydrogen chemical potential, μ_H, becomes an important factor [Kir85]. Following the theoretical concepts of Street [Str91], Beyer [Bey97, Bey03], and Kirchheim [Kir85] the trapping process can be described as a process which is governed by a temperature dependent hydrogen chemical potential, $\mu_H(T)$. In addition, a density of hydrogen states has to be assumed, resulting from the disorder of the amorphous network (for a schematic sketch see Fig. 6.6(b)). The effective diffusivity can now be written as [Str91]

$$D = D^* \exp\left(- \frac{H_{tr} - \mu_H}{k_B T} \right), \tag{6.1}$$

where H_{tr} is the enthalpy of the hydrogen transport path and D^* is the pre-exponential factor. However, since the density of hydrogen states is not known for the present materials,

an analytical expression for μ_H which adequately describes the present situation cannot be given. Nevertheless, it can be stated that due to the saturation of low energy sites additional hydrogen atoms have to occupy sites with higher energy, which leads to an increase of the hydrogen chemical potential ($\mu_H < 0$) with increasing hydrogen concentration. If in first approximation a linear temperature dependence of the chemical potential is assumed according to

$$\mu_H = \mu_H^0 + \beta T, \tag{6.2}$$

($\mu_H^0 < 0$, $H_{tr} < 0$), we get

$$D = D^* \exp\left(\frac{\beta}{k_B}\right)\exp\left(-\frac{H_{tr} - \mu_H^0}{k_B T}\right), \tag{6.3}$$

with $D_0 = D^* \exp(\beta / k_B)$ as the pre-exponential factor and $\Delta H^D = H_{tr} - \mu_H^0$ as the activation enthalpy of diffusion. Now, it can be assumed that with increasing hydrogen concentration an increase of μ_H takes place due to an increase of μ_H^0, while the quantity β decreases. This leads to a simultaneous decrease of the factor $\exp(\beta / k_B)$ and of the activation enthalpy ΔH^D, which may qualitatively explain the behaviour of the determined diffusion parameters. Depending on the special form of the density of hydrogen states, the decrease of the activation enthalpy is very likely connected with an involvement of more and more Si dangling bonds in the trapping process, while the pre-exponential factor has no longer the simple reciprocal dependence on the trap concentration. Under the assumption that there exists only a very low concentration of Si dangling bonds, meaning that they are inactive in the trapping process, a continuous distribution of N dangling bonds might also explain the results, which is, however, relatively unlikely. Further analysis is given in section 6.4.

6.1.2. Polycrystalline Si_3N_4 Films

To investigate the hydrogen diffusion in polycrystalline Si_3N_4, the as-deposited films were annealed at for 2 h 1500 °C in nitrogen. For this state a low hydrogen concentration of 0.5 at.% is measured by NRRA, nearly identical to the concentration in the pre-annealed amorphous films. Typical hydrogen diffusion profiles measured in the polycrystalline state and the corresponding numerical calculations are shown in Fig. 6.7 for an exemplary annealing temperature of 940 °C. For an annealing time of 2.3 h, a Gaussian-like profile is observed, in analogy to the amorphous state. However for additional annealing, a non-Gaussian profile develops while the deuterium concentration remains nearly constant at $[^2H_{tot}] = 4 \times 10^{25}$ atoms/m^3. At a depth of about 300 nm a steep exponential decrease in the concentration occurs forming a kind of “diffusion front”. The diffusion profile of the film

annealed for 33 h reaches nearly the same depth as that one annealed for 11.5 h, indicating a strongly time dependent hydrogen migration.

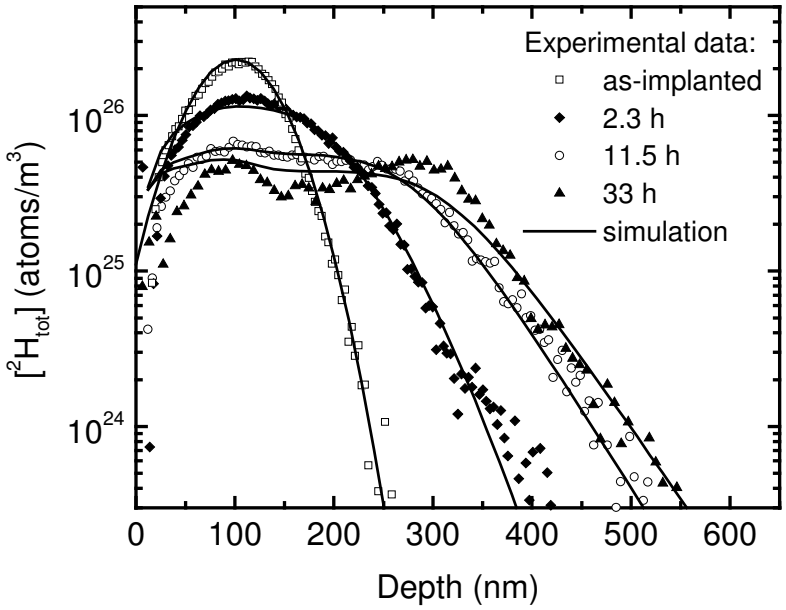

Figure 6.7 SIMS measurement of the ^{2}H concentration versus depth in polycrystalline Si_3N_4 after annealing for 2.3, 11.5, and 33 h at 940 °C in N_2. The ^{2}H background concentration was subtracted from the experimental data for a better comparison. The solid lines represent computer simulations based on the numerical solution of Eqs. (A.2) using the parameters R_1 = 4.3 x 10^{25} traps/m^3, k_1 = 1.4 x 10^{-26} m^3/s, ν_1 = 0, R_2 = 5.0 x 10^{26} traps/m^3, k_2 = 1.9 x 10^{-24} m^3/s, ν_2 = 0.25 s^{-1}, k_e = 4.2 x 10^{-30} m^3/s, and D_H = 1.4 x 10^{-15} m^2/s. For further details it is referred to the text.

This behaviour can be explained with a strong trapping effect at traps with a negligible dissociation of HR complexes. Here, an analytical solution of the diffusion equation is no longer possible. A reasonable numerical simulation of the migration process according to Eqs. (A.2) can only be achieved with the assumption of two different types of intrinsic trapping centres: traps with negligible dissociation R_1 and traps with moderately high dissociation R_2, respectively. At the beginning of the diffusion process the tracer migration into the solid is dominated by complex formation and dissociation at the traps R_2 with an effective diffusivity $D_{eff,2}$ = 3.6 x 10^{-19} m^2/s, similar to the amorphous case. During further annealing the migration is influenced more and more by the traps R_1 with negligible dissociation ($\nu_1 = 0$), which leads to a non-Gaussian profile form. When all tracer atoms are trapped, no further migration into the interior of the sample is possible due to the lack of dissociation, which leads to the observed "freezing in" of the diffusion process. A good numerical simulation of the profiles corresponding to the films annealed for 2.3 and 11.5 h at 940 °C can be achieved with the parameters given in Fig. 6.7. The results revealed that a minimum trap concentration of $[R_2] \geq 2 \times 10^{26}$ traps/m^3 and a concentration of $[R_1] = 4 \times 10^{25}$ traps/m^3 is necessary to reproduce consistently the time evolution of the depth profiles. Also, the "freezing in" of the diffusion process for the 33 h anneal is reproduced, however,

the measured profile deviates slightly from the simulation below 400 nm, which can be explained with an enhanced out-diffusion of the tracer close to the surface.

The present results of the polycrystalline state indicate that different types of active traps are present in comparison to the amorphous state. These trapping centres are attributed to be present at grain boundaries. Due to the crystallization process the number of dangling bonds in the bulk should decrease drastically due to the formation of three-dimensional long range order, making the trapping mechanism of the amorphous state ineffective. In the polycrystalline state, we observe about one order of magnitude lower diffusivities (Fig. 6.8), which also show an Arrhenius behaviour for short time anneals ($\Delta H^D \approx 4$ eV, $D_0 \approx 10^{-2}$ m^2/s). However, for long annealing times the motion of hydrogen is "blocked" by an immobilization reaction at the traps with negligible dissociation, resulting in a strong decrease of hydrogen migration.

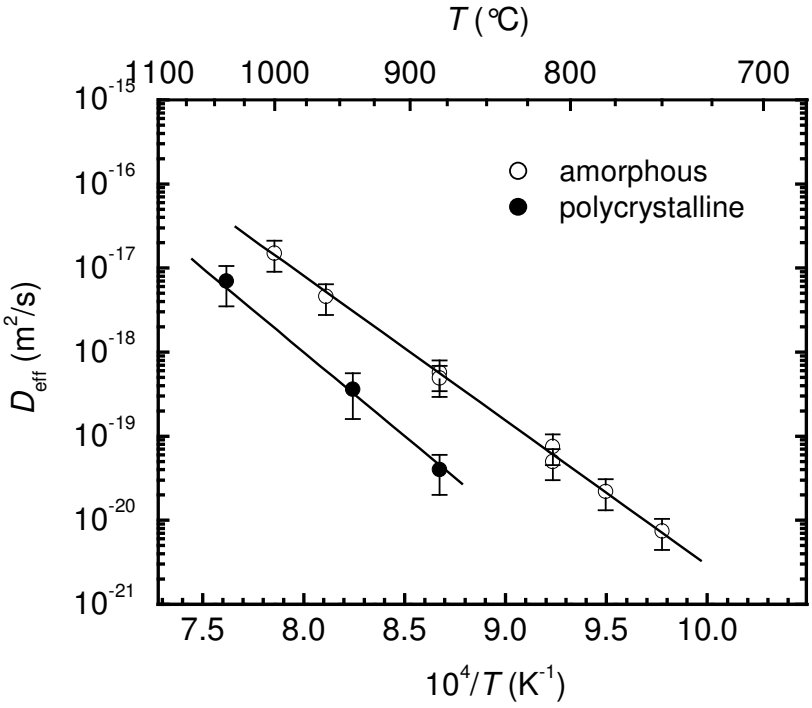

Figure 6.8 Effective diffusivities of hydrogen as a function of reciprocal temperature in amorphous Si_3N_4 and for short time anneals in polycrystalline Si_3N_4. For longer annealing times the diffusivity in polycrystalline films decreases drastically due to complex formation with negligible dissociation.

6.2. Diffusion of Hydrogen in Amorphous SiC and Si_2CN_4 Films

In addition to the studies on silicon nitride, experiments on the diffusion of hydrogen in amorphous silicon carbide (SiC) films (hydrogen concentration: 0.4 at.%) and amorphous silicon carbonitride (Si_2CN_4) films (hydrogen concentration: 0.5 at.%) were carried out in order to compare the results to similar covalently bound materials. Both types of films were produced my magnetron sputtering (see section 3.1.2) and were pre-annealed in Ar and N_2 for 2 h at 1000 °C, respectively. In the as-deposited state, Si_2CN_4 is an amorphous material

where nominally one silicon atom is replaced by one carbon atom. This material was investigated with the aim to understand the influence of chemical composition on the diffusion and trapping behaviour. Measurements were carried out for both types of films with ion implantation and additionally with the gas exchange method for SiC films pre-annealed at 1000 °C in N_2 - 6 % H_2, leading to a higher hydrogen concentration of about 1 at.%.

The obtained diffusion profiles are qualitatively identical to those obtained for amorphous Si_3N_4 and are consequently not discussed in further detail. For both materials, the data can be explained again with a trap-limited diffusion mechanism with a moderately high dissociation rate, and effective diffusivities can be extracted which are described by an Arrhenius behaviour with a single activation enthalpy (Fig. 6.9). Activation enthalpies of $\Delta H^D \approx 3.2$ eV (SiC) and $\Delta H^D \approx 3.0$ eV (Si_2CN_4) as well as pre-exponential factors of $D_0 \approx 7.1 \times 10^{-5}$ m^2/s (SiC) and $D_0 \approx 1.5 \times 10^{-5}$ m^2/s (Si_2CN_4) are derived for the films pre-annealed in a hydrogen free atmosphere (see also Appendix/Tab. B.3). As can be seen in Fig. 6.9 and Tab. B.3, the diffusivities, activation enthalpies, and pre-exponential factors of the ion-implanted SiC films are very close to those of amorphous Si_3N_4 (with approximately the same hydrogen content) and those of Si_2CN_4 are only slightly enhanced.

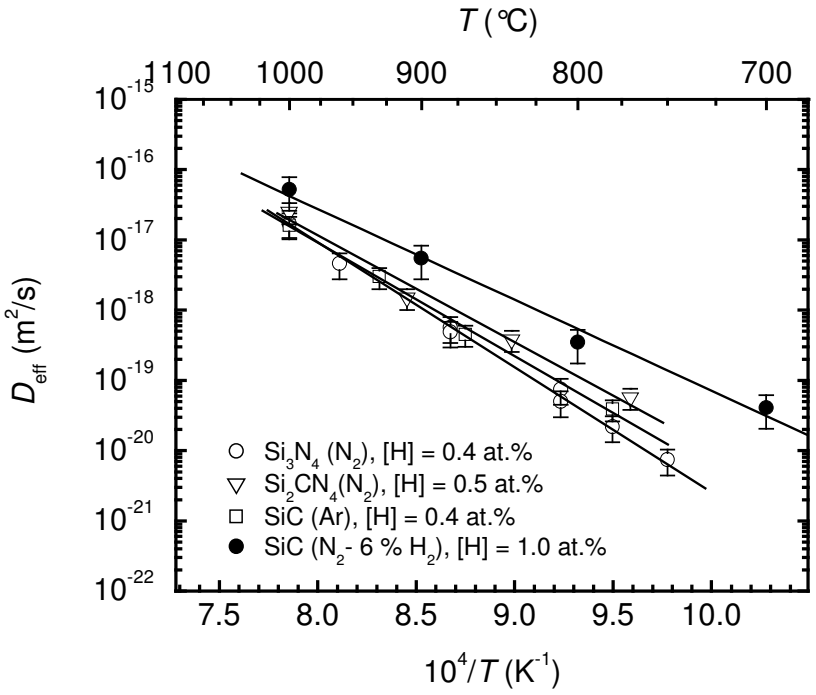

Figure 6.9 Effective diffusivities of ^{2}H in amorphous SiC and Si_2CN_4 as a function of reciprocal temperature. The hydrogen concentration and the annealing atmosphere is indicated.

This very astonishing result means that neither the chemical composition nor the local short range order of Si-C-N based materials does influence the trapping and dissociation behaviour significantly. For amorphous Si_3N_4 and SiC tetrahedrally coordinated silicon

atoms are present, where the nitrogen atoms are connected to a three dimensional amorphous network structure [Mas01, Jus02]. For Si_2CN_4, the corner-linked Si_3N_4 tetrahedra are connected via N=C=N bridges in order to form a three dimensional network, the so-called carbodiimide structure [Rie97, Gre97, Lut01]. These different structures with different atomic distances, bonds, and bond angles show nearly the same diffusion behaviour of hydrogen, which can be understood in the framework of a trap-limited diffusion mechanism. For the three materials with a low hydrogen concentration Eq. (A.8) can be applied. Due to this equation effective diffusivities are identical if the dissociation enthalpy and the trap concentration are equal. According to calculations of Robertson [Rob91], the energy levels of C-H and N-H bonds in Si_3N_4 and SiC are located at almost the same energy of -4 eV with respect to the value in free space. This means, if the rate limiting step of effective diffusion is identified with the dissociation of the C-H and/or the N-H bonds, the diffusivities are identical for the same trap concentration. This assumption seems to be fulfilled in the present case. As a result, it can be concluded that the present materials show the same migration behaviour of hydrogen, as long as the thermodynamic state is the same (amorphous) and the hydrogen concentrations are similar. In contrast, measurements with the gas exchange method on SiC films with a higher hydrogen concentration of about 1 at.% show enhanced diffusivities due to lower values of ΔH^D and D_0, as already observed for the system Si_3N_4. For a more detailed analysis its is referred to section 6.4, where the results are discussed together with the results of the Si-(B-)C-N precursor ceramics.

6.3. Diffusion of Hydrogen in Polymer-Derived Si-(B)-C-N Ceramics

Investigations on the tracer diffusion of hydrogen in Si-(B-)C-N based polymer-derived ceramics were carried out on four different types of materials, three boron containing ceramics (T21, MW33, and AM26) and one boron free (VT50) ceramic. The diffusion and defect interaction of hydrogen in Si-(B-)C-N materials is intensively investigated in the framework of the doctoral thesis of W. Gruber [Gru05a]. Here, only the most important results are discussed for an overall understanding of the topic.

6.3.1. Hydrogen Diffusion in Si-(B-)C-N Materials of Type T21

Detailed investigations on the tracer diffusion of hydrogen as a function of pre-annealing temperature were carried out on T21 materials with the gas exchange method and SIMS in order to clarify the possible influence of atomic re-arrangement processes on hydrogen motion. During pre-annealing, substantial changes in mass density and in free volume (the difference between the actual volume and the volume of an optimised packing of atoms) occur in amorphous Si-B-C-N ceramics [Rei03]. Some typical depth profiles are displayed in Fig. 6.10, where a penetration of the deuterium tracer into the solid material is clearly visible. The diffusivities are extracted by fitting the depth profiles to Eq. (3.6). The results are plotted in Fig. 6.11 as a function of reciprocal temperature. During this study,

samples thermolyzed at 1400 °C were investigated as well as samples which were pre-annealed for 2 h at 1460 and 1600 °C in nitrogen, respectively. As shown in Fig. 6.11 the hydrogen diffusivities obey Arrhenius laws for all pre-annealing states. The diffusivities of the samples in the as-thermolyzed state and the samples pre-annealed at 1460 °C are located on the same straight line and are fitted with a unique activation enthalpy of 2.2 eV and a pre-exponential factor of $D_0 = 3$ x 10^{-8} m^2/s. In contrast, the diffusivities for the samples pre-annealed at 1600 °C are located on a straight line shifted parallel to higher diffusivities by a factor of five with the same activation enthalpy and a pre-exponential factor of 1.4 x 10^{-7} m^2/s. For an as-thermolyzed sample, investigations of hydrogen diffusion were also carried out with ion implanted deuterium isotopes where an activation enthalpy of 2.5 ± 0.3 eV and a pre-exponential factor of 1 x 10^{-7} m^2/s is derived, in acceptable accordance with the gas exchange measurements [Sch02b].

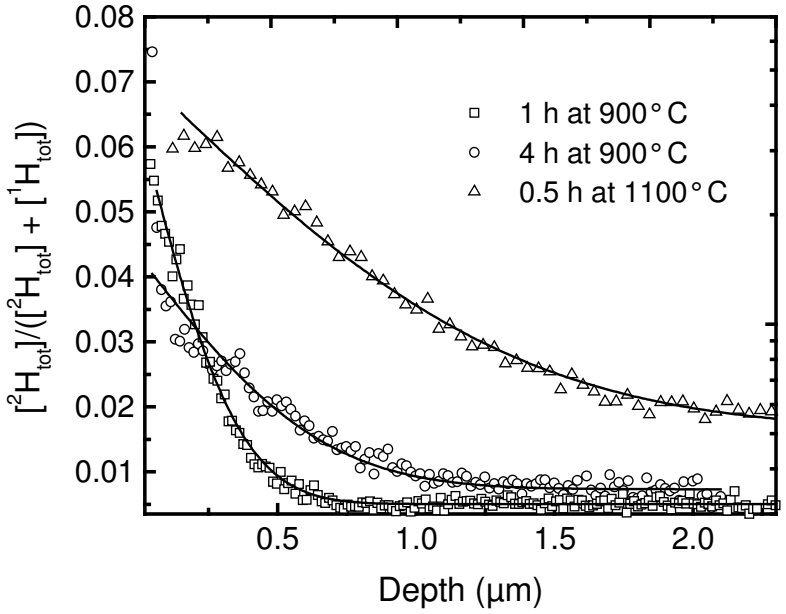

Figure 6.10 Typical diffusion profiles of ^2H tracers in T21 samples (pre-annealed at 1460 °C) after gas exchange annealing for 1 and 4 h at 900 °C and for 0.5 h at 1100 °C, respectively.

As in the case of silicon nitride and silicon carbide films, the determined diffusion data can be related to a trap-limited diffusion mechanism with a moderately high dissociation rate. The unique value of the activation enthalpy of 2.2 eV indicates that the same types of trapping centres are effective for the different pre-annealing states investigated. Due to the low hydrogen concentration in the order of 0.2 at.%, Eq. (A.8) is applied here and a trap concentration of $R_0 \approx 10^{29}$ atoms/m^3 is obtained for the as-thermolyzed samples, which is rather high. However, if the error of log $D_0 = \pm 0.6$ (see Appendix/Tab. B.3) is considered as well as the fact that the quantities R_c and ν_0 cannot be given with an accurateness better than a factor of five, a lower value of $R_0 \approx 10^{27}$ might be also present here, which is within reasonable physical limits for a system with low hydrogen concentration. Pre-annealing of the Si-B-C-N samples at 1600 °C before diffusion annealing leads to an increase of D_0 by a

factor of about five, which means that according to Eq. (A.8) R_0 is reduced if unchanged values of R_c and ν_D are assumed. Measurements with NRRA show that the hydrogen concentration of the samples annealed at 1460 and 1600 °C does not change measurably, indicating that hydrogen concentration based effects on diffusion (as for Si_3N_4) cannot account for the observed scatter of the data. Consequently the reduction of traps due to pre-annealing at 1600 °C has to be attributed to an annihilation or recombination of dangling bonds due to atomic re-arrangement processes.

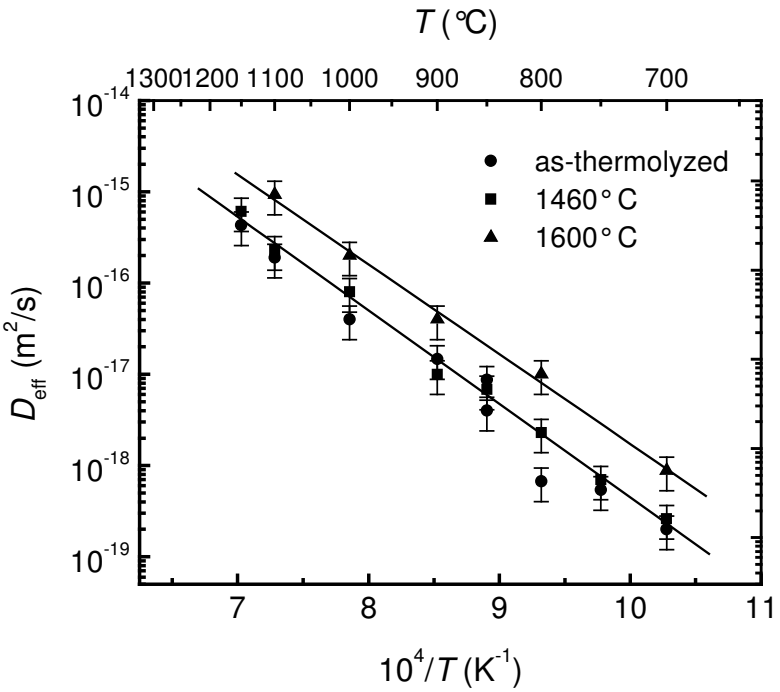

Figure 6.11 Effective diffusivities of ^2H in amorphous T21 as a function of reciprocal temperature for as-thermolyzed samples and samples pre-annealed for 2 h at 1460 °C and 1600 °C in N_2.

6.3.2. Influence of Chemical Composition

In Fig. 6.12. the effective hydrogen diffusivities of several amorphous Si-(B-)C-N ceramics are plotted as a function of reciprocal temperature in order to study the influence of chemical composition on diffusion. The diffusivities of T21, VT50, and MW33, all pre-annealed at 1460 °C, coincide within estimated errors and can be fitted with a unique straight line corresponding to an activation enthalpy of 2.2 eV and a pre-exponential factor of 3 x 10^{-8} m^2/s. This quite astonishing behaviour reflects that ceramics with different chemical composition, which are synthesized along different routes from different polymers (see section 3.1.1), show the same diffusion behaviour of hydrogen. In addition, the identical diffusivities of VT50 and T21 prove that the incorporation of boron in the Si-C-N matrix has no significant influence on hydrogen migration. The hydrogen diffusivities of amorphous SiC and Si_3N_4 films (determined with the gas exchange method), which are also plotted in Fig. 6.12 for comparison, exhibit nearly the same diffusivities as the T21

ceramics with very similar activation enthalpies in the range between 2.2 to 2.6 eV and pre-exponential factors in the order of 10^{-6} - 10^{-8} m^2/s (see Appendix/Tab. B.3).

For a straightforward interpretation of the defect interaction in Si-(B-)C-N it is necessary to get an insight into the binding of hydrogen to the surrounding atoms. As a result of FTIR measurements on VT50 ceramics, hydrogen is bound to C, Si and N atoms of the surrounding amorphous matrix after thermolysis [Bil98]. This indicates that in principle all types of atoms may act as a trapping centres here. In section 6.3 the breaking of N-H bonds and of C-H bonds is identified as the most probable rate limiting step for the motion of hydrogen in amorphous Si_3N_4 and SiC films with a low hydrogen concentration. With increasing hydrogen concentration, Si dangling bonds were assumed to be the rate limiting step. Taking into account the lower activation enthalpies measured in the present Si-(B-)C-N materials, the results permit to attribute the trapping of hydrogen to a dominating influence of Si dangling bonds. A strongly different situation arises for the AM26 material, where the diffusivities (as obtained by the gas exchange method) are considerably higher (up to several orders of magnitude at low temperatures) and are described by a much lower activation enthalpy of only 0.3 eV and an extremely low pre-exponential factor of 4 x 10^{-14} m^2/s (Fig. 6.12 and Appendix/Tab. B.3).

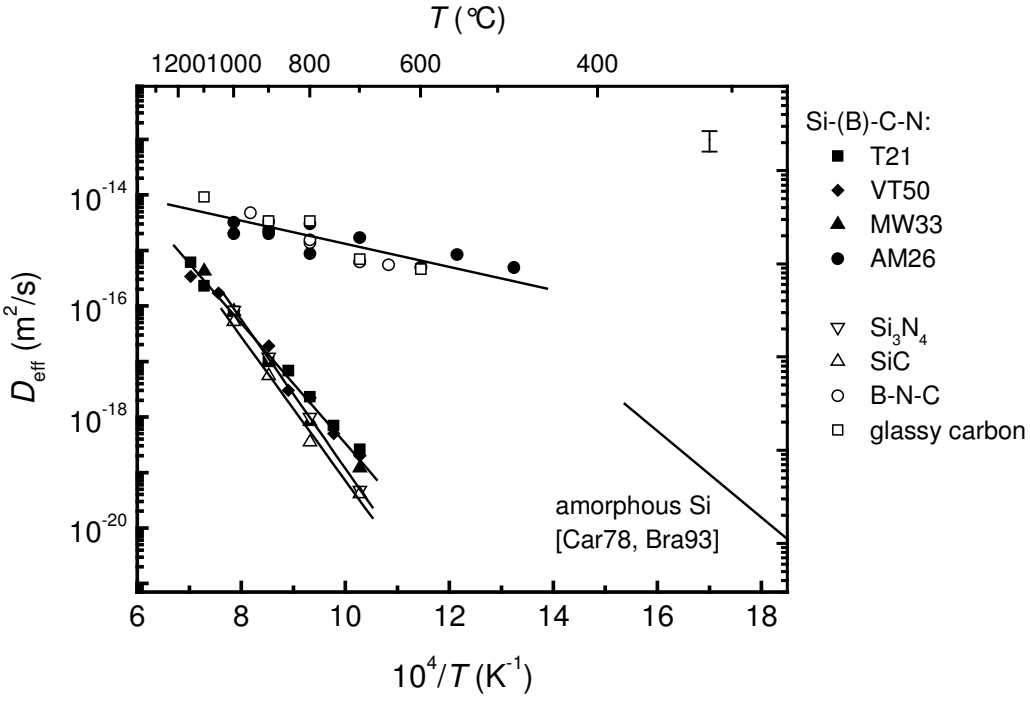

Figure 6.12 Effective diffusivities of ^2H in various Si-(B-)C-N ceramics and related materials as a function of reciprocal temperature. A typical error bar is indicated.

In order to consistently explain the present results on Si-(B-)C-N, the concept of phase-separated amorphous domains is again used. As described in section 2.2, amorphous Si-B-C-N is composed of nano-sized amorphous $Si_{3+0.25x}C_xN_{4-x}$ and BNC_x domains, and Si-C-N is composed of amorphous $Si_{3+0.25x}C_xN_{4-x}$ and C domains, respectively [Hau04a, Hau04b].

It is concluded from the present measurements that in AM26 ceramics diffusion occurs via another type of amorphous domain than in VT50, T21, and MW33 ceramics. Since VT50 (Si-C-N), T21 and MW33 (Si-B-C-N), as well as amorphous Si_3N_4 films, show identical or similar diffusivities the common diffusion medium of these ceramics has to be identified as the $Si_{3+0.25x}C_xN_{4-x}$ domain. The exact chemical composition of this phase (concentration of Si, C, and N) has no significant effect on the diffusion behaviour, meaning that the presence of amorphous Si_3N_4 domains (as for VT50) or of mixed $Si_{3+0.25x}C_xN_{4-x}$ domains (as for T21 and MW33) are not reflected in the diffusion behaviour, which is not unexpected considering the results of section 6.2.

Further application of the discussed concept implies that the much higher diffusivities in AM26 ceramics are a result of a diffusion along BNC_x domains, which are present in Si-B-C-N. To prove this assumption, additional diffusion measurements were carried out on amorphous B-N-C films which were produced by PECVD (section 2.3). The resulting diffusivities in the temperature range between 500 and 1000 °C are also shown in Fig. 6.12. The diffusivities of the B-N-C films are nearly identical to those of the AM26 ceramics within error limits. One can now argue that in AM26 and in the B-N-C films no trap-limited diffusion mechanism is present and that the intrinsic hydrogen diffusion (interstitial-like mechanism) is measured. However, this is in contradiction to the low pre-exponential factor determined for AM26 ceramics. In the case of an intrinsic diffusion mechanism, the pre-exponential factor should be given by $D_0 \approx \nu_0\, a^2 \approx 1 \times 10^{-7}$ m^2/s as for single crystalline silicon [Wie56]. This is in strong contrast to the values of 10^{-12} - 10^{-14} m^2/s as obtained for AM26 and B-N-C (Appendix/B.3). Consequently, a trap-limited diffusion mechanism has to be assumed also for AM26 ceramics. However, applying Eq. (A.8) to the pre-exponential factor, an absolutely unrealistic trap density in the order of 1×10^{34} m^{-3} is calculated, showing that these data cannot be explained with the model used. An explanation for the unconventional diffusion parameters of AM26 can be given again on the basis of the concept where the trapping process is governed by a temperature dependent hydrogen chemical potential as formulated in section 6.1.1. For a location of μ_H^0 close to the enthalpy level of interstitial-like hydrogen, H_i (see Fig. 6.6), a strongly reduced activation enthalpy of diffusion, $\Delta H^D = H_{tr} - \mu_H^0$, of about 0.5 eV is obtained, which corresponds roughly the activation enthalpy of the intrinsic diffusion process, ΔH_m. Using this model, the low pre-exponential factor is now the consequence of a low value of β.

Additional experiments on hydrogen diffusion were carried out in glassy carbon (see section 2.3) with the gas exchange method. As shown by neutron scattering, glassy carbon is a good model substance which describes the phase separated amorphous carbon phase in Si-C-N ceramics [Hau04b]. As described in Ref. [Gru05a], the diffusivities show a complicate diffusion behaviour, depending on the ^{2}H concentration and on annealing time. The diffusivities shown in Fig. 6.12 correspond to profiles with a large penetration depth obtained for long annealing times. They are very similar to the diffusivities of B-N-C films and of AM26 ceramics and the data of all three types of materials can be fitted with a unique Arrhenius straight line with an activation enthalpy of about 0.4 eV. If these results

are assigned to the concept of phase separated domains in Si-(B-)CN ceramics, it is obvious that the long range diffusion in amorphous C domains and in BNC_x domains is the same. Since in VT50 ceramics much lower diffusivities are measured, the amorphous carbon phase can be excluded as hydrogen transport path in Si-C-N, very likely due to the fact that no percolation path is formed or the transport capacity of a percolation path is too small to observe diffusion.

Also shown in Fig. 6.12 are the hydrogen diffusivities in amorphous silicon as-measured first by Carson and Magee [Car78] for comparison. It was found that atomic hydrogen diffuses in amorphous silicon with a trap-limited diffusion process, characterized by an activation enthalpy of 1.5 eV, were H interacts with Si dangling bonds. Fig. 6.12 shows that the diffusivities in amorphous silicon are strongly different from those investigated here in multi-component Si-C-N based materials.

6.3.3. Effusion of Hydrogen from Si-(B-)C-N Materials

In order to address the effusion mechanism of hydrogen from Si-(B-)C-N, the hydrogen concentration of various samples was determined with NRRA. For these investigations VT50, T21, MW33, and AM26 samples were used, which were cut from the interior of thermolyzed bulk materials. The as-thermolyzed ceramics all show a high hydrogen concentration of about 3 - 7 at. % (see Appendix/Tab. B.4), which resulted from the synthesis from pre-ceramic polymers. Annealing in nitrogen in the temperature range between 1460 and 1800 °C leads to a significant loss of hydrogen down to a residual concentration of 0.1 - 0.8 at. %. An important point here is that annealing at 800 or 900 °C, a temperature which is lower than the thermolysis temperature, likewise leads to a decrease of the hydrogen concentration by a factor of roughly ten down to 0.2 - 1.6 at. %. With respect to the diffusion length of hydrogen of only 1 µm for 1 h of annealing at this temperature (Fig. 6.12), it is concluded that the effusion of hydrogen is not a process controlled by volume diffusion. It can be assumed that most of the hydrogen in the as-thermolyzed state is present in pores of the material left from the thermolysis, weakly bound to the surface. Annealing at relatively low temperatures leads to a desorption and to a decrease of the hydrogen content to values around 0.5 – 1.6 at. %. This residual hydrogen is present in the interior of the ceramics, bound to the surrounding atoms and is diffusing slowly due to a trap-limited mechanism. An extrapolation of the measured diffusivities to higher values results in a diffusion length of 20 - 30 µm at 1500 °C. Considering an average pore to pore distance of 20 - 50 µm as measured by surface profiling, the effusion of this residual hydrogen at higher temperatures can be described as a two stage process. First, a diffusion controlled migration of hydrogen to the pores occurs and afterwards a fast outward motion to the sample surface along pores. Thus, the only way for hydrogen atoms to leave a compact ceramic body is an interconnected void or pore structure. Dense samples without any porosity (which are not available at the moment) should contain significantly higher amounts of hydrogen up to much higher temperatures.

6.4. The Compensation Law

In order to correlate the hydrogen diffusion parameters of all materials investigated in this study, the activation enthalpies and the logarithm of the pre-exponential factors are plotted together in Fig. 6.13. The data obey a compensation law over eleven orders of magnitude according to

$$\ln D_0 = \ln D^+ + \frac{1}{k_B T^+} \Delta H^D, \tag{6.4}$$

where D^+ is the pre-exponential factor and T^+ is the isokinetic temperature, where all diffusivities are equal (for a detailed discussion see e. g. [Fie01]). An understanding of that compensation law can be found in terms of Eq. (6.2) and (6.3). It is assumed that every material plotted in Fig. 6.13 is characterized by a hydrogen chemical potential, μ_H, which is determined by certain values of the trap concentration, the hydrogen concentration, and/or the hydrogen density of states. It is further assumed that a variation of μ_H takes place only due to a change of $\mu_H{}^0$ and β in the opposite direction (see Eq. (6.2)). Since, $\ln D_0 = \ln D^* + \beta/k_B$ and $\Delta H^D = H_{tr} - \mu_H{}^0$, a high chemical potential μ_H is connected with a low activation enthalpy ΔH^D and a low pre-exponential factor D_0 and vice versa. This qualitatively explains the occurrence of the compensation law. Since the hydrogen density of states and also the exact trap concentration is not known for the various materials, it is not possible to calculate μ_H as a function of temperature and a quantitative data analysis is not possible. The common link between all the materials in Fig. 6.13 is very probably the fact that the trapping centres (C, N, and Si dangling bonds) are located at nearly the same enthalpy for different materials. The fact that in glassy carbon, B-N-C, and AM26 ceramics no Si traps are present at all seems to have to influence.

As shown in Fig. 6.13, the present data do not yet prove unambiguously a continuous variation of ΔH^D and D_0. Three distinct regions of ΔH^D can be identified where data points are located: between 3.0 and 4.0 eV, between 2.2 and 2.7 eV, and between 0.3 and 1.0 eV. The occurrence of these regions might correspond to the location of the hydrogen chemical potential close to regions of a high density of hydrogen states, which occurs around the N-H and C-H bond enthalpy, around the Si-H bond enthalpy, and around the enthalpy of interstitial hydrogen atoms. In-between these regions a jump of μ_H may (but not necessarily has to) occur due to a gap or a low density of states.

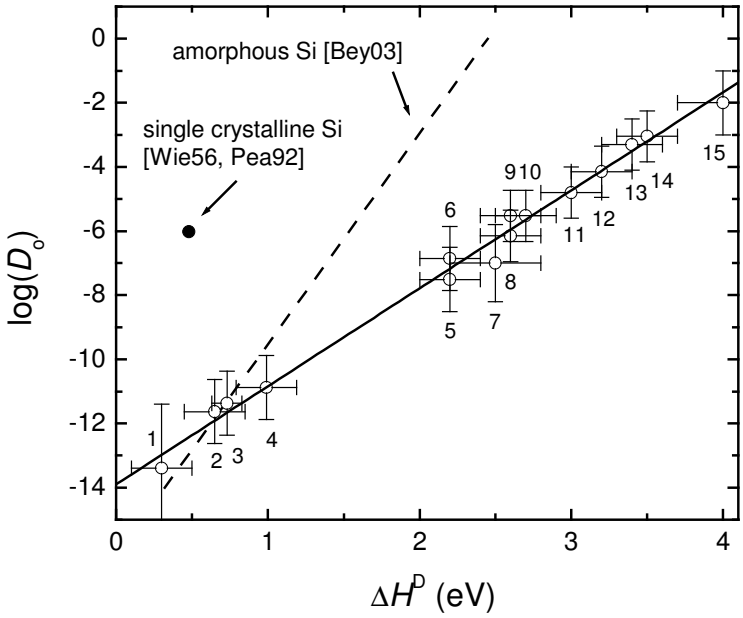

Figure 6.13 Logarithm of the pre-exponential factor, D_0, plotted as a function of the activation enthalpy of diffusion, ΔH^D, for the amorphous Si-C-N based and related materials measured in this study. 1: AM26, 2: glassy carbon (long annealing times), 3: B-N-C, 4: glassy carbon (short annealing times), 5: T21/MW33/VT50 (1460), 6: T21(1600), 7: T21(cast), 8: SiC (1000HE), 9,10: Si_3N_4 (1000HE), 11: Si_2CN_4, 12: SiC (1000), 13: Si_3N_4, 14: Si_3N_4 (1000/1200), and 14: Si_3N_4 (1500). Also shown are data on amorphous Si from Ref. [Bey03] and on single crystalline Si from Ref. [Wie56]. For certain values the pre-annealing temperature is given in brackets. HE means annealed in a hydrogen enriched atmosphere.

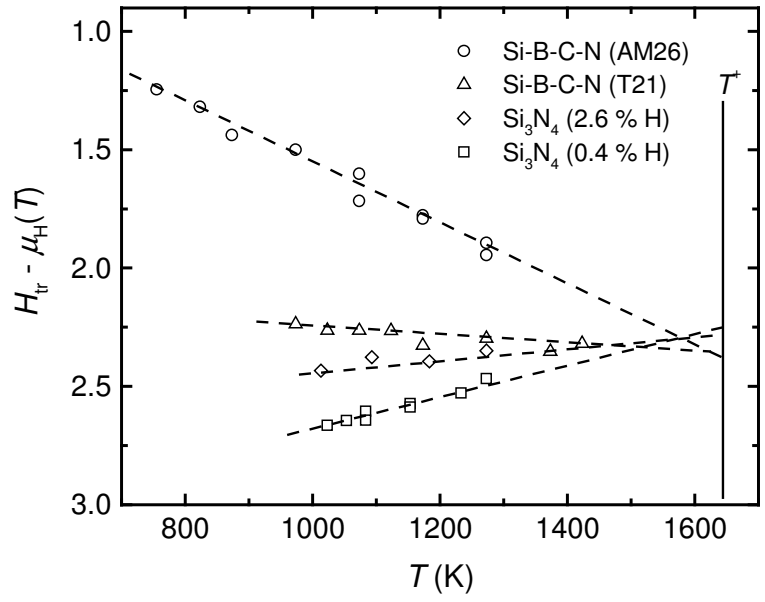

Figure 6.14 Hydrogen chemical potential, μ_H, calculated relative to the hydrogen transport level, H_{tr}, as a function of temperature for selected Si-C-N based materials.

In Fig. 6.13 also the intrinsic diffusivity of hydrogen in single crystalline silicon is plotted, which is definitely not obeying the compensation law, reflecting the fact that for this material no trap-limited, but a pure interstitial diffusion mechanism is operating.

Diffusion data of hydrogen in amorphous silicon for different hydrogen concentrations taken from Ref. [Bey03] are also indicated in Fig. 6.13. These data obey also a compensation law [Bey99], however, resulting from a variation of μ_H only with hydrogen concentration in different Si films, as also found for Si_3N_4 in section 6.1.1. These two compensation laws are definitely not identical. The parameters $D^+ = 1.3 \times 10^{-14}$ m^2/s and $T^+ = 1648$ K are derived by linear fitting for the present Si-C-N related materials, while values of $D^+ = 6 \times 10^{-17}$ m^2/s and $T^+ = 760$ K are found for amorphous silicon [Bey99]. A possible reason for that difference might be the fact that in the present multinary materials other or further types of traps are active than in silicon and a completely different density of hydrogen states is present.

Using a value of $D^* \approx 1 \times 10^{-7}$ m^2/s for the intrinsic pre-exponential factor, the quantity $H_{tr} - \mu_H$ can be calculated from the experimental data according to Eq. (6.1), which reflects the shift of the hydrogen chemical potential with temperature. In Fig. 6.14 some typical examples for materials of Fig. 6.12 are given. A linear temperature dependence of the chemical potential is clearly visible, in accordance with the assumption of Eq. (6.2), supporting the present theory. An extrapolation to higher temperatures shows that close to the isokinetic temperature of 1648 K $H_{tr} - \mu_H$ is nearly identical for the different materials.

7. Formation Kinetics of Crystalline Precipitations in Polymer-Derived Amorphous Si-(B-)C-N Ceramics

Thermodynamically metastable amorphous Si-(B-)C-N ceramics can be prepared by solid state thermolysis at temperatures between 1000 and 1400 °C (see section 3.1.1). Annealing at higher temperatures in nitrogen or inert atmosphere leads to the formation of crystalline silicon carbide (SiC) and silicon nitride (Si_3N_4), yielding different types of composites with completely clean grain boundaries [Pen02]. In the present section, XRD studies as a function of annealing time and additional selective TEM measurements were carried out to obtain systematic information on the mechanisms and kinetics of precipitate formation. These investigations were realized in order to obtain data, which allow to produce composites with a tailored microstructure by in-situ crystallization, as well as to understand the thermal stability of the amorphous state on a fundamental level and to optimise it for technological applications. In these materials, diffusion controlled processes are expected due to the multinary nature of the material. Samples of various chemical compositions obtained from different processing routes are studied as a function of annealing time and temperature. Materials of the Si-B-C-N system (T21, MW33, AM26) are compared to materials of the Si-C-N system (VT50, NCP200) in order to get insight into the role of boron on the stability of amorphous ceramics.

In Fig. 7.1 X-ray diffractograms of various Si-(B-)C-N ceramics in the as-thermolyzed state and after annealing for 4 hours at elevated temperatures are displayed. The diffractograms show that the ceramics are all amorphous after thermolysis, which was also proven by high resolution and energy-filtering TEM and SAED measurements [Bil00, Cai01, Jan05, Rie96]. Annealing leads to partial or complete crystallization of SiC and/or Si_3N_4, depending on the chemical composition, on the temperature, and on the annealing time. While for Si-C-N the α modification of Si_3N_4 is formed, for Si-B-C-N the β modification is stable.

Generally, the formation of the crystalline SiC and Si_3N_4 in a supersaturated amorphous Si-(B-)C-N matrix and the subsequent development of the microstructure may be influenced by various overlapping processes. For the present materials, three independent processes were identified in the framework of this study: (1) the crystallization of SiC and Si_3N_4 mediated by nucleation and growth, (2) a transformation of Si_3N_4 to SiC due to a solid state reaction, and (3) crystallite growth due to coarsening. The progress of these transformations can be tracked by monitoring the average diameter of the SiC and Si_3N_4 crystallites $\langle d \rangle$ and the transformed volume fraction χ of the two phases as a function of annealing time. The classical crystallization process mediated by nucleation and growth is governed by an increase of both quantities as a function of annealing time, while for coarsening only $\langle d \rangle$ grows with annealing time and χ remains approximately constant. For solid state reactions the variation of these quantities depends on the certain mechanisms

governing the transformation and are discussed later on. More details on the theory of phase transformations can be found in Refs. [Wag01, Chr75, Chr65].

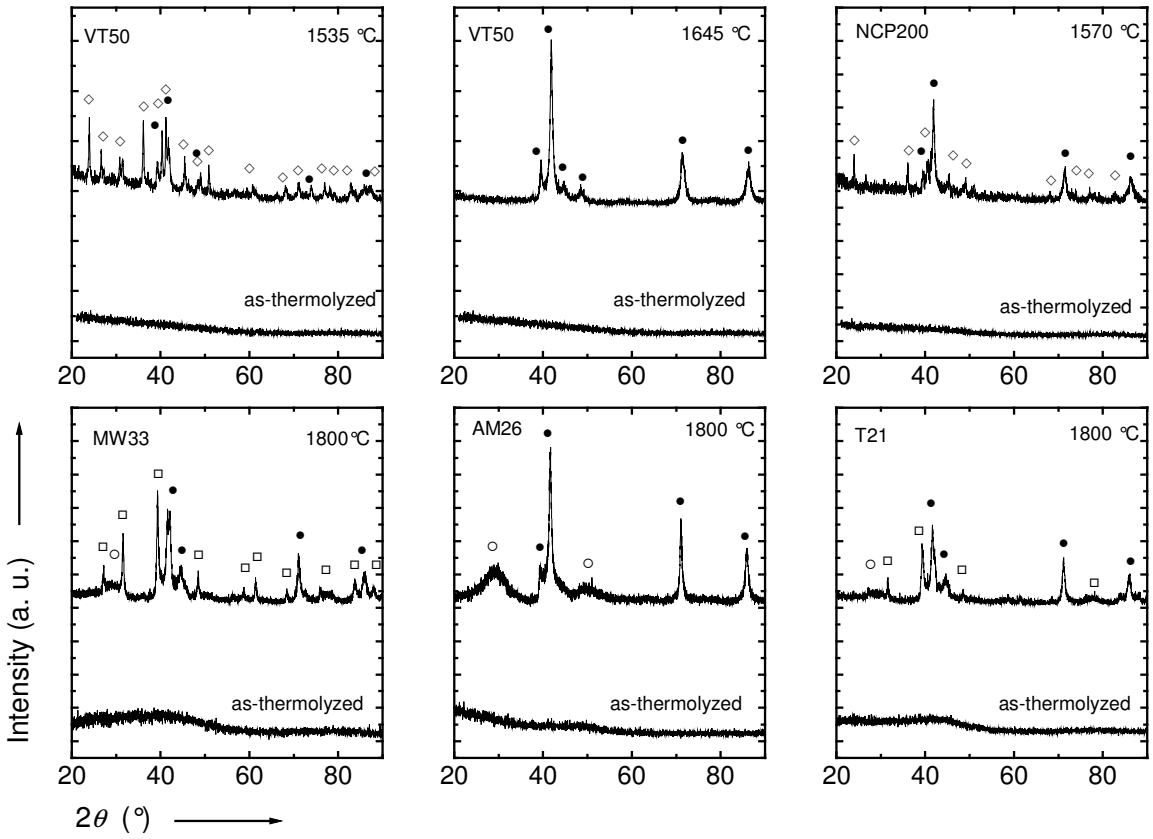

Figure 7.1 X-ray diffractograms of various Si-(B-)C-N ceramics in the as-thermolyzed state and after annealing at elevated temperatures for 4 h (exception: 50 h for VT 50 annealed at 1535 °C). The Bragg peaks corresponding to the crystallized phase are marked: SiC (●), α–Si_3N_4 (◇), and β–Si_3N_4 (□). The broad structure marked with an ○ is reminiscent of an amorphous or turbostratic BNC_x phase.

Both of the quantities <*d*> and χ were determined by XRD studies, which were carried out as a function of annealing time. The following systematic procedure was applied: first, the amorphous material was isothermally annealed at a distinct temperature for a given time. Then the material was characterized by XRD and afterwards annealed again. Certain Bragg peaks were numerically fitted with a Lorentzian function, from which the integrated peak area I and the full width at half maximum $\beta(2\theta)$ of the corresponding peak were determined. It is assumed that the volume of a newly formed phase, $V_i(t)$ (i = Si_3N_4, SiC), is proportional to the integrated intensity, $I_i(t)$, of a single X-ray peak. The peak at 2θ = 24.03 ° was used for α–Si_3N_4, that at 2θ = 31.5 ° for β–Si_3N_4, and that at 2θ = 71.20° for SiC to determine the volume fraction $\chi_i(t) = I_i / I_i^{max}$ of formed phase i at an annealing time t. I_i^{max} is the corresponding value for complete transformation of phase i. The XRD peaks were chosen in such a way that no or only minimum overlap with neighbouring peaks is

present. The use of other Bragg peaks did not result in a different transformation behaviour within estimated errors.

If no micro-strain is present, the average volume-weighted crystallite diameter (for definition see e. g. Ref. [Nat96]), $<d>$ can be determined from $\beta(2\theta)$ with the Scherrer formula [Sch18, Klu74], using a single Bragg peak for analysis

$$< d > = \frac{0.9\ \lambda}{\beta(2\theta)\ \cos\theta}, \tag{7.1}$$

where λ = 0.1789 nm is the wave length of the CoK_α tube radiation. The use of different peaks for analysis allows the additional calculation of possible micro-strain ε according to the Williamson-Hall equation [Wil53, Klu74]

$$\frac{\beta(2\theta)\ \cos\theta}{\lambda} = \frac{1}{< d >} + \varepsilon \frac{4\ \sin\theta}{\lambda} \tag{7.2}$$

from a straight line fit to the data points, if $\beta(2\theta)\cos\theta/\lambda$ is plotted against $4\sin\theta/\lambda$.

7.1. Crystallization of Si-C-N Ceramics

For amorphous Si-C-N ceramics of type VT50, the crystallization of α–Si_3N_4 and SiC is observed in the temperature range between 1500 - 1645 °C (Fig. 7.1). Graphite reflexes or reflexes of other carbon phases were not detected by XRD. This has to be explained with the formation of a carbon enriched amorphous matrix phase during crystallization in order to conserve atom numbers. Indeed, such a kind of phase was proven by TEM measurements on ceramics made of the same type of material after annealing at 1500 [Bil98] and 1600 °C [Wic03]. Annealing at a lower temperature of 1450 °C for about 400 h does not result in any detectable X-ray reflections of crystalline phases, indicating that the material is still amorphous. An analysis of the average crystallite diameters of α–Si_3N_4 and SiC is given in Fig. 7.2, where two typical examples of Williamson-Hall diagrams are displayed. For SiC an average crystallite size of $<d> \approx$ 30 - 40 nm is determined, independent of the annealing temperature [Sch04b].

In contrast, for α–Si_3N_4 it was not possible to identify the crystallite size exactly, because the corresponding broadening of the peak is beyond or close to the broadening caused by the apparatus function of the X-ray diffractometer. Only a lower limit of the average crystallite size of $<d> \geq$ 100 nm could be derived. These results are in accordance with TEM investigations on Si-C-N material [Fri94], which revealed micro-crystalline Si_3N_4 with a crystallite size of about 0.5 - 1 µm and nano-crystalline SiC. All samples investigated show considerable micro-strain of about $\varepsilon \approx$ 0.002 - 0.003 not changing

systematically with temperature. It is concluded from the present results that the thermally induced crystallization process leads to a complex composite material composed of micro-crystalline Si_3N_4, nano-crystalline SiC, and an amorphous C-rich residual Si-C-N matrix.

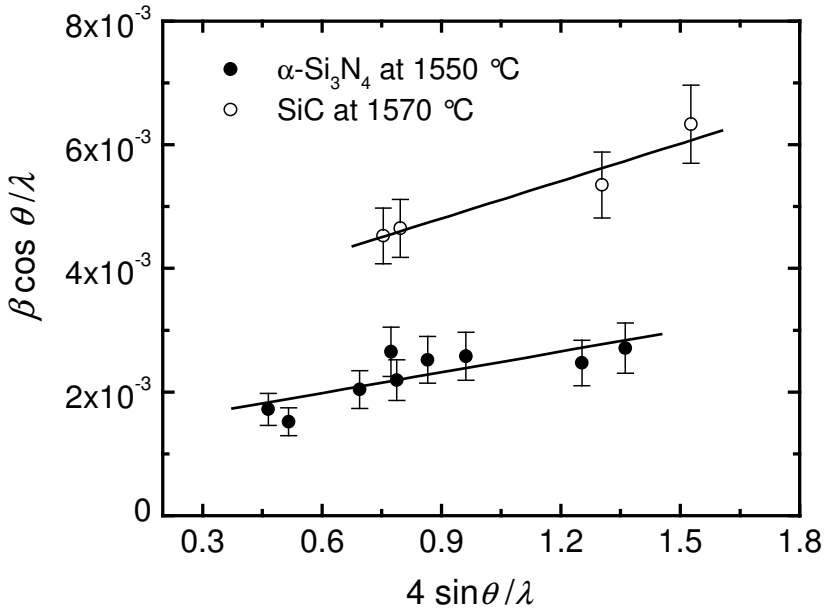

Figure 7.2 Williamson-Hall diagram for α-Si_3N_4 and SiC formed during the crystallization of VT50 ceramics, exemplarily illustrated for two temperatures.

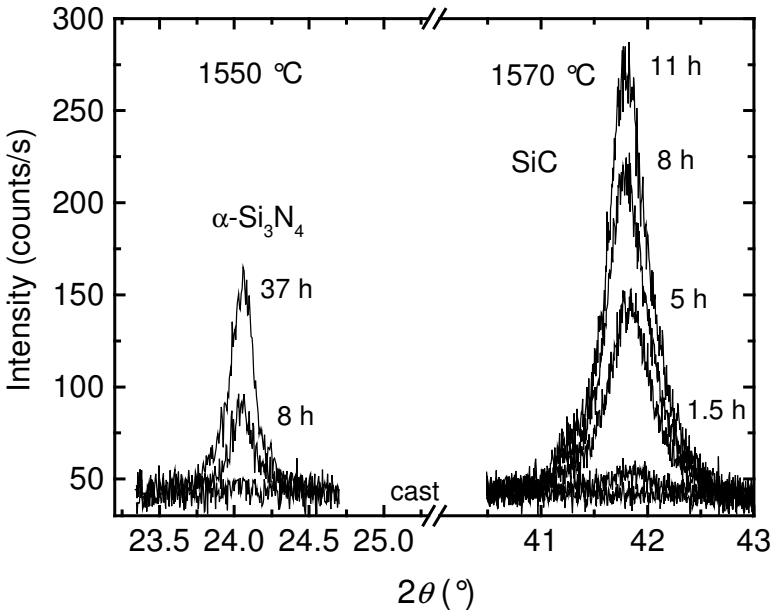

Figure 7.3 Exemplary illustration of the growth of a α–Si_3N_4 Bragg peak at 1550 °C and of a SiC Bragg peak at 1570 °C for VT50 ceramics. The annealing times are indicated. Not all data are shown for clarity.

The variation of the Bragg peaks with increasing annealing time is exemplarily illustrated in Fig. 7.3. An increase of the integrated peak area, and thus of the crystallized

volume fraction is clearly visible. A monotonic variation of the peak width, $\beta(2\theta)$, as a function of annealing time is not observed. The crystallized volume fraction, χ, as a function of annealing time is displayed in Fig. 7.4 for various temperatures. With increasing annealing time, χ increases in a sigmoidal way for all temperatures. Annealing for long times leads to a saturation corresponding to a complete crystallization of both phases. Also visible in Fig. 7.4 is that the crystallization of Si-C-N is a process, where α–Si_3N_4 and SiC are formed simultaneously in the temperature range where a formation of both phases is observed (for more details see section 7.2).

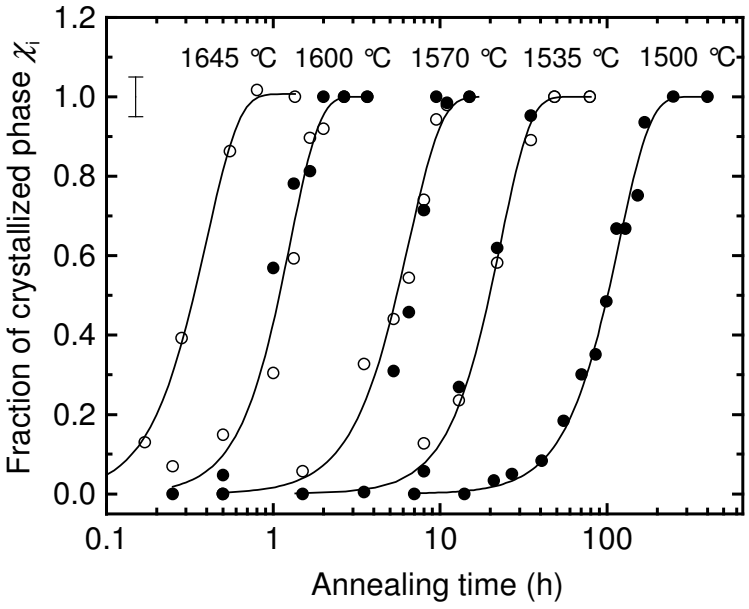

Figure 7.4 Normalized fraction of crystallized α–Si_3N_4 (full circles) and SiC (open circles) as a function of annealing time at various temperatures for VT50 ceramics. The solid lines correspond to a fit of the data according to Eq. (7.4). A typical error bar is indicated.

The crystallization process is further analysed using the classical nucleation and growth theory [Chr65]. In case of isotropic nucleation, the crystallized volume fraction $\chi(t)$ of a specimen after time t is given by

$$\chi(t) = 1 - \exp\left(-\int_0^t I_N \; V(t-t')\,\mathrm{d}t' \right). \tag{7.3}$$

where V is the volume of a particle at time t which is nucleated at time t' and I_N is the nucleation rate. The crystallized volume is given by $V = g\, r^{m/l}$, where g is a geometric factor, r is the radius of a crystallized particle, m describes the dimensionality of the growth process, and l describes the crystallization mode (interface-reaction controlled (l = 1) or diffusion controlled (l = 2)). For a constant nucleation rate or for crystallite growth from pre-existing nuclei Eq. (7.3) can be written as

$$\chi(t) = 1 - \exp\left(-(k_{NG}\, t)^n\right) \tag{7.4}$$

according to Johnson, Mehl, Avrami, and Kolmogorov (JMAK-theory) [Avr39, Avr40, Avr41, Joh39, Kol37]. Here, k_{NG} is the temperature dependent rate constant of crystallization and $n = m/l + 1$ is the JMAK exponent giving information on the dimensionality of the growth and on the type of nucleation. Analysis of the experimental data in Fig. 7.4 in terms of Eq. 7.4. yields JMAK exponents in the range between $n = 2.0$ and 2.4 for both crystalline phases, leading to an average value of $n = 2.3 \pm 0.3$. A value of $n = 2.5$ is in accordance with a three-dimensional diffusion controlled crystallite growth and a constant nucleation rate* during the growth process [Chr65]. Such a diffusion controlled growth is expected due to the multi-component nature of the Si-C-N material, where long range re-arrangement processes of the elements are required in order to form the precipitated phases. For this limiting case, k_{NG} is given by

$$k_{\mathrm{NG}} = g I_{\mathrm{N}}^{2/5} (2\ \gamma\ D)^{3/5} \tag{7.5}$$

where D is the self-diffusivity of the slowest moving species, $\gamma \approx 0.6$ - 0.75 is the fraction of crystallized phase (from phase diagram considerations [Pen01]), and $g = 1.67$. In contrast, a value of $n = 1.5$ is in accordance with a diffusion controlled growth from pre-existing nuclei, respectively [Chr65]. If the JMAK exponents appear to be in between these two limiting cases the actual nucleation is of 'intermediate nature', e.g. a time dependent nucleation rate. The JMAK description is not applicable in a strict sense to this intermediate case. However, a detailed analysis of that problem shows that the application of the JMAK formalism is also useful here [Kem02]. Assuming a decreasing nucleation rate according to $I_{\mathrm{N}} = I_0 \exp(-t/\tau)$ with a typical time constant τ, Eq. (7.3) has to be integrated numerically and fitted to the experimental data. Such calculations show that in order to obtain a value of $n = 2.3$ the nucleation rate, I_{N}, has to decrease by only 20 % of the starting value I_0 until complete crystallization is achieved. Thus, further analysis is carried out using a value of $n = 2.5$ for simplicity. For Si-C-N ceramics of type NCP200 with different chemical composition qualitatively the same crystallization behaviour is observed as for the VT50 compound (for details see Ref. [Sch05a]).

The rate constants of crystallization for both Si-C-N ceramics are strongly temperature dependent and are given in Fig. 7.5 as a function of reciprocal temperature. A simultaneous formation of α–Si_3N_4 and SiC is observed between 1500 and 1600 °C. At 1500 °C only

* The term "constant nucleation" does not mean that the number of nuclei which are formed during a time interval is constant until all phase is crystallized, which would be not quite reasonable. The number of nuclei at a time t is rather given by

$$N = \int_0^t I_{\mathrm{N}} (1 - \chi(t'))\mathrm{d}t'.$$

α–Si_3N_4 and at 1650 only SiC is formed for VT50 ceramics. It is obvious that the data can be described for each material with an unique Arrhenius law of the form

$$k_{NG} = k_{NG}^{0} \exp\left(-\frac{\Delta H^{NG}}{k_B T}\right), \tag{7.6}$$

where ΔH^{NG} is the activation enthalpy of crystallization and k_{NG}^{0} the pre-exponential factor. Extremely high values of ΔH^{NG} = 12.8 ± 1.2 eV and k_{NG}^{0} = 2 x 10^{31} s^{-1} (NCP200) and of ΔH^{NG} = 12.5 ± 1.0 eV and k_{NG}^{0} = 7 x 10^{29} s^{-1} (VT50) are obtained for the two materials (see also Appendix/Tab. B.5).

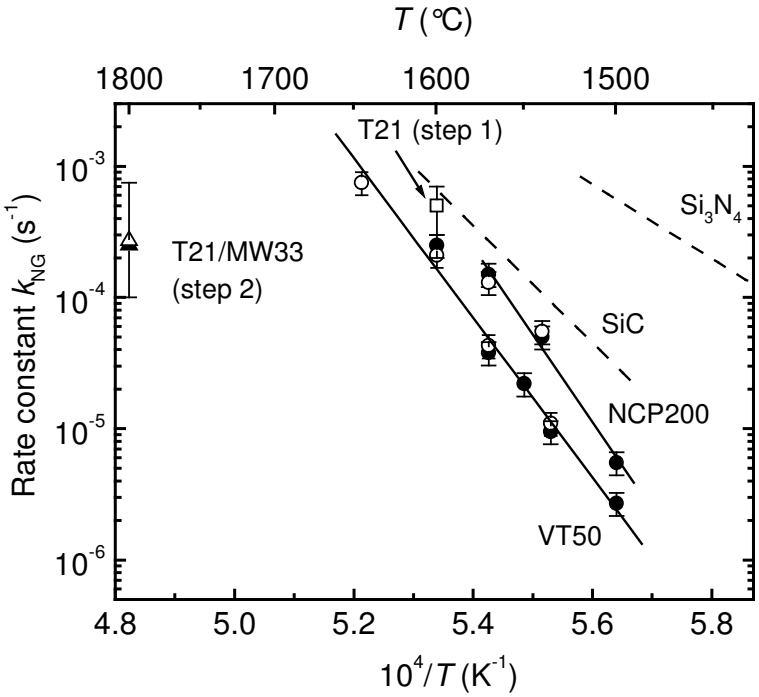

Figure 7.5 Rate constants of crystallization for SiC (open symbols) and Si_3N_4 (filled symbols) for amorphous Si-C-N as a function of reciprocal temperature. The various types of materials are indicated. Also shown are the data for the crystallization of Si-B-C-N (section 7.3) and of SiC and Si_3N_4 films (dashed lines; section 8).

The extraordinarily high activation enthalpy of about 12 - 13 eV governing the crystallization of Si-C-N has the consequence that an extended amorphous phase field is present up to 1450 °C, which can be used for technical applications. In contrast, only a small temperature window of only 150 °C (between 1500 and 1650 °C) is available for a controlled crystallization of amorphous Si-C-N in order to tailor microstructures. The pre-exponential factors are also extremely high, which should lead to a fast crystallization. However, they are overcompensated by the enormous activation enthalpy of crystallization with the result of low crystallization rates. In contrast to Si-C-N, the crystallization rates measured for amorphous Si_3N_4 and SiC are higher, at least one order of magnitude at low

temperatures (see Fig. 7.5 and section 8). This is reflected in lower activation enthalpies between 5.5 and 8.9 eV (see Appendix/Tab. B.5). This trend is also supported by literature data. Seher et al. [Seh94] obtained an activation enthalpy of only 3.3 eV for the crystallization of amorphous polymer-derived Si_3N_4 using optical microscopy. Measurements on the crystallization kinetics of amorphous SiC were done by Kurtenbach et al. [Kur99] on polymer-derived material, by Calgano et al. [Cal01] on films produced by CVD, and by Inoue et al. [Ino87] on sputter deposited films resulting in activation enthalpies of about 5 - 7 eV. These results clearly show that the high activation enthalpy of crystallization is the reason for the enhanced stability of amorphous Si-C-N in comparison to the binary counterparts Si_3N_4 and SiC.

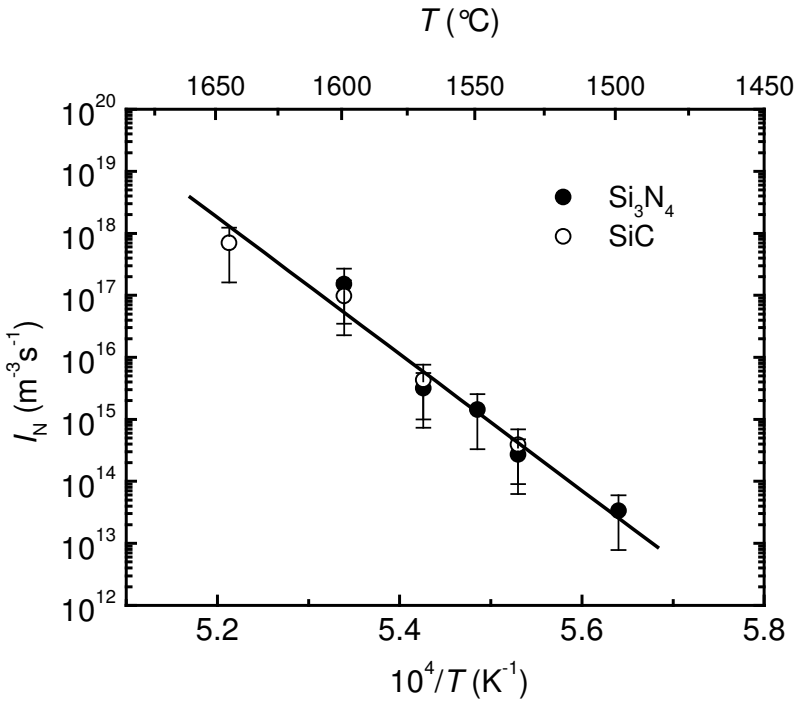

Figure 7.6 Nucleation rate of VT50 ceramics as a function of reciprocal temperature as obtained by Eq. (7.5)

If the self-diffusivities of the slowest moving species are known in the temperature range where the crystallization experiments were carried out, the nucleation rate can be calculated from Eq. (7.5). Using the linearly extrapolated self-diffusivities of the VT50 material from section 4.2, a temperature dependent nucleation rate is obtained as shown in Fig. 7.6. At 1500 °C a slow nucleation rate in the order of $I_N \approx 10^{13}$ nuclei m^{-3} s^{-1} is obtained which is increasing rapidly to a 10^5 times higher value of about $I_N \approx 10^{18}$ nuclei m^{-3} s^{-1} at 1645 °C. The data can be described also by an Arrhenius behaviour with an activation enthalpy of nucleation as high as $\Delta H^N \approx 22$ eV.

As obvious from Eqs. (7.5), (7.6), and (4.4) the activation enthalpies of the two elementary processes, diffusion and nucleation, are related by

$$\Delta H^{NG} = \tfrac{3}{5}\Delta H^{D} + \tfrac{2}{5}\Delta H^{N}, \tag{7.7}$$

with $\Delta H^{D} \approx 6$ eV and $\Delta H^{N} \approx 22$ eV. These data clearly demonstrate that both, nucleation and growth (controlled by diffusion) plays a significant role for the kinetics of crystallization in amorphous Si-C-N ceramics. A clear domination of one mechanism (nucleation controlled or growth controlled) does not occur. The activation enthalpy of nucleation is given by [Chr65]

$$\Delta H^{N} = \Delta H^{I} + \Delta G^{*}, \tag{7.8}$$

where ΔG^{*} is the work of nucleus formation and ΔH^{I} is the enthalpy for the transfer of an atom across the amorphous/crystalline interface and its subsequent incorporation into the lattice, which can be approximately set as the activation enthalpy of self-diffusion, $\Delta H^{I} \approx \Delta H^{D}$. A value of $\Delta G^{*} \approx 16$ eV is derived, independently of temperature. ΔG^{*} is given by [Chr65]

$$\Delta G^{*} = \frac{16\,\pi\,\Gamma^{3}}{3\,\Delta\mu^{2}\Omega^{2}}, \tag{7.9}$$

where Γ is the surface free energy of the crystal/amorphous interface, Ω = 1.2 x 10^{5} mol/m^{3} is the mole density of the matrix, and $\Delta\mu$ is the difference of the chemical potentials between the amorphous and the crystalline phase (driving force of nucleation). Generally, $\Delta\mu$ strongly depends on temperature and is given by

$$\Delta\mu = \Delta H_{ac} - T\Delta S_{ac} \approx \Delta S_{m}\,\Delta T, \tag{7.10}$$

where ΔH_{ac} and ΔS_{ac} are the enthalpy and entropy differences between amorphous and crystalline state, ΔS_{m} is the melting entropy, and $\Delta T = T^{*} - T$ is the "undercooling" of the material compared to a temperature T^{*} where the amorphous and the crystalline phases coexist. The influence of this term would lead to a strong non-linear behaviour of the rate constants in the Arrhenius plots of Figs. 7.5 and 7.6, where k_{NG} and I_{N} have to decrease with increasing temperature close to T^{*}, contrary to the present results (for a sketch see Fig. 7.7). The observed Arrhenius-like transformation with no local maximum in the crystallization and nucleation rates is in contrast to the crystallization of oxide glasses [Vog77, Zan85] and metallic glasses [Loe03, Fau03], where the expected non-monotonic behaviour is commonly observed.

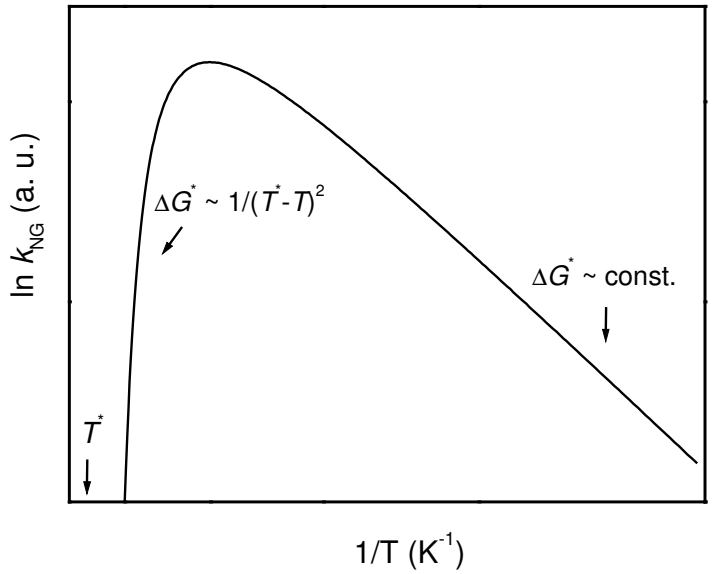

Figure 7.7 Schematic sketch of the rate constant of crystallization vs. reciprocal temperature as observed commonly for metallic glasses and oxide glasses.

The measured linear increase of ln k_{NG} as a function of $1/T$ and the temperature independence of ΔG^* can be attributed in principle to the fact that our measurement data are far away from T^*, and a relatively large supersaturation (undercooling) is present. However, using the temperature dependence given in Eqs. (7.9) and (7.10) for simulations, it is found that an equilibrium temperature of at least T^* = 10000 °C is necessary for an adequate description of the experimental data in Fig. 7.5, which is not very reasonable. In order to explain the present findings, there exist three possibilities: (1) the assumption of $\Delta\mu \approx \Delta S_m \Delta T$ is not valid for the present case. (2) The enthalpy for the transfer of an atom through the amorphous/crystalline interface, ΔH^I, is higher than the enthalpy of self-diffusion, ΔH^D. (3) The self-diffusivities governing the crystallization process at high temperatures do not coincide with those measured in the amorphous state pre-annealed at 1460 °C.

Concerning point (1), an approximately constant driving force of crystallization, $\Delta\mu$, has to be present in the present temperature range, which can be realized by a temperature independence of the quantity ΔH_{ac} and a very low value of ΔS_{ac} or by the influence of the heat capacity, ΔC_p, which is neglected in the approximation of Eq. (7.10). In Ref. [Gol04] a simple thermodynamic model of amorphous Si-C-N is presented, where the entropy difference between amorphous and crystalline state and the temperature dependence of ΔH_{ac} are neglected. As a first approximation, $\Delta\mu \approx \Delta H^0$ is used for the VT50 compound, where ΔH^0 = (69 ± 13) kJ/(mol Si_3N_4) (0.1 eV/atom) is the standard molar enthalpy change for the transition from amorphous Si_3N_4 to α-Si_3N_4, as determined from florine combustion calorimetry [Tom01]. According to Eq. (7.9) a quite high, but reasonable value of 0.2 eV/surface-atom (Γ = 0.6 J/m^2) is calculated for the interfacial energy in order to reproduce a work of nucleus formation as high as ΔG^* = 16 eV. This

surface free energy is about two times higher than the corresponding value found for the crystallization of amorphous silicon, where the same $\Delta\mu$ but a value of $\Delta G^* = 2$ eV is present [Spi98]. From the calculated data a critical radius of nucleus formation in Si-C-N of $r_c = 2\,\Gamma/(\Delta\mu\,\Omega) \approx 1$ nm is found. However, according to Ref. [Gol04] the driving force of crystallization, $\Delta\mu$, should be lower by a factor of roughly two for the NCP200 ceramics, which is definitely not reflected in the present experimental data. For an exact modelling of the process detailed thermodynamic data are necessary.

To address item (2), a value of at least $\Delta H^I \approx 23$ eV and $\Delta G^* << \Delta H^I$ would be necessary to explain the observed Arrhenius behaviour of ΔH^{NG}. This might be achieved if the jump of an atom through the amorphous to crystalline interface is strongly hindered, e.g. due to segregated atoms at the grain boundaries. However, TEM investigation give no hint for such a situation [Pen02].

A completely different interpretation of the measured high activation enthalpy of crystallization can be given if the use of the self-diffusion data in the amorphous state for the modelling of the crystallization behaviour does not hold. The measured diffusivities correspond to a metastable amorphous state which was formed by pre-annealing the material at 1460 °C. This results in a defined microstructure and point defect concentration of the amorphous matrix. However, crystallization anneals at higher temperatures may result in a modification of the amorphous matrix (in the partially crystallized sample) with strongly enhanced diffusivities, away from a linear extrapolation of the data. Consequently, the diffusivities may vary stronger with temperature as measured in section 4.2. Such a model can not be excluded on basis of the present experimental results. However, it is very unlikely because no difference is found between the Arrhenius straight lines of Si diffusion in VT50, pre-annealed at 1350 and 1460 °C, respectively (section 4.3). This means, that the metastable amorphous states corresponding to both pre-annealing temperatures are identical, at least with respect to self-diffusion. It has to be noted that for the diffusion of Ge* in VT50 ceramics, a significant decrease of the diffusivities is observed with increasing pre-annealing temperature from 1200 to 1350 °C by Matics et al. [Mat00], but not an increase as would be necessary to address item (3). In addition, measurements in amorphous Si-B-C-N [Vos03] indicate that Ge is no good substitute for Si in these materials.

The rate constants of the NCP200 material are higher than the rate constants of the VT50 material by a factor of about 2 - 3 in the whole temperature range investigated (Fig. 7.5). Defining the rate constant k_{NG} as a characteristic parameter which describes the stability of the amorphous phase at a given temperature, the differences in k_{NG} for the two types of materials lead to a reduced stability of the NCP200 material. However, due to the high activation enthalpy this effect is only slightly developed, leading to a shift of the "stability curve", ln k_{NG} vs. $1/T$, to lower temperatures by only 25 °C. If, for example, an

* Ge is often used as an isoelectric substitute for Si in order to realize diffusion measurements with the radiotracer method.

activation enthalpy of about 5 eV would be given for Si-C-N, as for the binary amorphous compound Si_3N_4 a reduction of k_{NG} by a factor of 2 - 3 would lead to a shift close to 100 °C. From the present data the reason for the difference in the rate constants of the two Si-C-N materials investigated cannot unambiguously be derived. However, it can be tentatively attributed to a different supersaturation of the amorphous matrix at different compositions, which leads to slightly different activation enthalpies of nucleation.

As a result from the preceding analysis, the enormous stability of amorphous Si-C-N against crystallization is the result of a combined effect of kinetic and thermodynamic factors. Very low self-diffusivities with high activation enthalpies and a high temperature independent work of nucleus formation leads to a high temperature independent activation enthalpy of crystallization. Nucleation and growth contribute both to crystallization. As will be shown in section 8, the crystallization of SiC and Si_3N_4 is dominated by a growth process of already nucleated crystallites. This leads to a considerably lower activation enthalpy and a higher rate constant of crystallization in comparison to Si-C-N.

7.2. Solid State Reactions in Si-C-N Ceramics

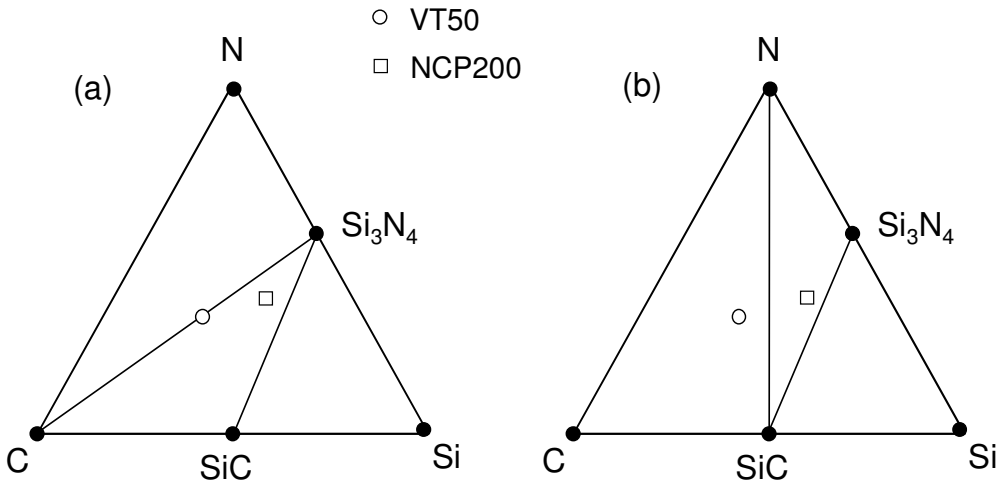

Figure 7.8 Isothermal sections of the Si-C-N system at a total pressure of 1 bar for **(a)** $T < 1484$ °C and **(b)** 1484 °C < $T < 1841$ °C (after Ref. [Pen02]). The composition of amorphous Si-C-N ceramics is indicated.

The special arrangement of the microstructure of partially crystallized Si-C-N, where Si_3N_4, SiC and carbon coexist, implies that in addition to crystallization, other atomic re-arrangement processes may influence the formation of crystalline phases. Probably, a complete or partial dissociation of Si_3N_4 may occur according to the solid state reaction

$$Si_3N_4 + 3\,C \leftrightarrow 3\,SiC + 2\,N_2, \qquad (7.11)$$

where crystalline Si_3N_4 reacts with amorphous carbon to crystalline SiC and gaseous nitrogen, which leaves the sample. The equilibrium temperature of this reaction is 1484 °C at ambient pressure [Pen02] and two different isothermal sections of the phase diagram result for temperatures above and below this temperature (see Fig. 7.8). This transformation process might overlap with the crystallization process and influence the kinetics.

Table 7.1 Relative volume fractions of crystallized SiC (in comparison to Si_3N_4) after complete crystallization of both phases for various temperatures.

Annealing temperature (°C)	VT50	NCP200
1500	0	10 %
1535	25 %	-
1540	-	30 %
1550	35 %	-
1570	90 %	50 %
1600	95 %	-
1645	100 %	-

A hint for the existence of such a process can be found in the relative amount of crystalline SiC and Si_3N_4 which is formed after complete crystallization, as given in Tab 7.1. The data are calculated from the XRD patterns with the PCW program (section 3.4.5) for various temperatures. For VT50 material annealed at 1500 °C only α–Si_3N_4 is detected. With growing temperature the fraction of α–Si_3N_4 decreases and at the same time the fraction of SiC increases, until at 1645 °C only SiC is present. The observation that only SiC is formed at 1645 °C is in agreement with the phase diagram, calculated for the thermal equilibrium phases SiC, C and N_2 in Fig. 7.8(b). Since C is still amorphous and N_2 is gaseous, both phases can not be detected by XRD. However, the formation of gaseous N_2 was proven by thermogravimetric measurements, where a weight loss of the sample of about 10 % occurs [Fri02]. On the other hand, the results at lower temperatures between 1500 and 1570 °C are in contrast to the phase diagram, where Si_3N_4 should be present only at temperatures below 1484 °C in thermal equilibrium with C (Fig. 7.8(a)). Considering the data of Tab. 7.1 it is obvious that the temperature where reaction (7.11) is in equilibrium, is shifted from 1484 °C to a higher value of about 1550 °C. Above 1550 °C Si_3N_4 decomposes and below 1550 °C Si_3N_4 is still stable. A possible explanation for that effect might be given by the presence of an enhanced nitrogen partial pressure at the crystallite surface of Si_3N_4 due to the embedding in the amorphous carbon rich Si-C-N matrix (see also sections 2.1 and 7.4). According to Ref. [Fri02] the equilibrium of reaction (7.11) is shifted to higher temperatures for a higher nitrogen partial pressure. However, it is still unclear why no discrete transition temperature, but a temperature range (1500 - 1600 °C) is

present where both crystalline phases coexist. Here, an inhomogeneous distribution of microstructures with different local partial pressure may account for this phenomenon. NCP200 ceramics show a similar behaviour with the only difference that at high temperatures residual α–Si_3N_4 is still observed by XRD. However, this is also in accordance with the phase diagram in Fig, 7.8(b) due to the different chemical composition of NCP200 and VT50. In order to investigate the kinetics of reaction (7.11) the following experiments were carried out. Samples which were completely crystallized due to annealing at a certain temperature were post-annealed for prolonged periods at the same temperature. For example, a VT50 sample which was crystallized at 1500 °C during a 100 h anneal or a NCP200 sample which was crystallized at 1540 °C during a 10 h anneal were post-annealed for further 100 h (see also Refs. [Sch04b, Sch05a]). Here, the initial phase composition does not change significantly during the whole post-annealing period, indicating that the system is locally in thermodynamic equilibrium (or metastable equilibrium). Another explanation might be the fact that reaction (7.11) exhibits a very low rate constant of transformation, much lower than the rate constant of crystallization.

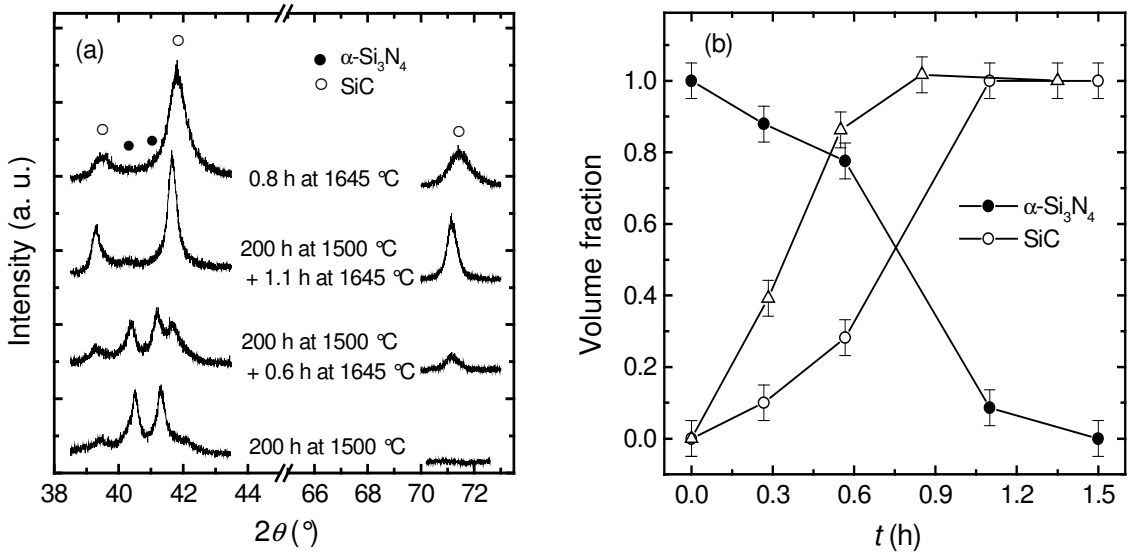

Figure 7.9 (a) X-ray diffractograms of VT50 ceramics after annealing at 1500 °C for 200 h and successive post-annealing at 1645 °C compared to a diffractogram after direct annealing at 1645 °C. **(b)** Volume fraction of unreacted α-Si_3N_4 and formed SiC as a function of post-annealing time at 1645 °C for the sample crystallized at 1500 °C (circle) and for the directly annealed sample at 1645 °C (triangle). The lines are a guide to the eye.

However, post-annealing of a VT50 sample where only crystalline Si_3N_4 is present at a higher temperature of 1645 °C results in the formation of crystalline SiC by reaction (7.11), as illustrated in Fig. 7.9. From the analysis of the XRD peaks of SiC and Si_3N_4 the rate constant of the transformation, k_T, is obtained by determining a time $\tau = 1 / k_T$, where the volume fraction of transformed material $\zeta(t)$ is increased to a value of $\zeta(\tau) = 0.63$ (in analogy to a JMAK type of transformation). A rate constant of $k_T = (3.5 \pm 1.0) \times 10^{-4}$ s^{-1} is obtained, which is about two times smaller than the value determined for the direct crystallization of amorphous Si-C-N at 1645 °C (see Fig. 7.9(b)). This explicitly proves that

the formation of SiC due to a solid state transformation is slower than the direct crystallization process out of an Si-C-N matrix, also at temperatures as high as 1645 °C.

The analysis of the average crystallite diameters of the XRD data in Fig. 7.9 leads to the interesting result that nano-crystalline SiC (<*d*> = 60 nm) is formed out of micro-crystalline Si_3N_4 during the transformation. This strongly implies that a direct reaction, controlled by volume diffusion of the constituents in the newly formed SiC phase is very unlikely. Instead, an indirect mechanism is suggested, where C and Si atoms dissolve from carbon and Si_3N_4 at grain boundaries, segregate at preferred nucleation sites, and form the nucleus of the new SiC phase.

With the present results, also more detailed information can be given on the crystallization process of SiC and α–Si_3N_4 in amorphous VT50 and NCP200 materials (section7.1), where both phases are formed simultaneous with the same rate constants. To describe this process two different scenarios are possible: the first one is that Si_3N_4 crystallizes first with a JMAK type of kinetics, and afterwards SiC crystallites are formed out of Si_3N_4 crystallites according to reaction (7.11). For this case, a simultaneous formation of both phases is possible only if the formation of SiC due to reaction (7.11) is considerably faster than the crystallization of Si_3N_4. This is definitely not the case, as demonstrated. Consequently, a second scenario is much more likely, where both phases are formed by a parallel nucleation and growth process and not in a successive way. That means that a decomposition of amorphous Si-C-N is taking place prior to the crystallization process due to the formation of SiC and Si_3N_4 nuclei, whose number is determined by local thermodynamic conditions.

7.3. Microstructural Evaluation of Si-B-C-N Ceramics

For high temperature stable, boron containing Si-B-C-N ceramics two classes of materials have to be distinguished. For the AM26 material, which is located in the three phase range SiC, C and BN (Fig. 3.1), only SiC crystallites are formed in an amorphous Si-B-C-N matrix during annealing. In contrast, for the other both types of ceramics, T21 and MW33, which are located in the four phase range SiC, C, Si_3N_4 and BN, crystalline SiC as well as β-Si_3N_4 are precipitated (see Fig. 7.1).

First, the AM26 material is discussed, where XRD investigations were carried out in the temperature range between 1600 and 1900 °C. Using Eq. (7.1) for analysis, small crystallites between 2 and 30 nm are detected, depending on temperature and annealing time. An analysis of the XRD diffractograms with the Williamson-Hall method yielded no significant hint on a possible contribution of micro-strain to profile broadening. From the XRD patterns the approximate fraction of crystallized SiC phase is calculated to be about 15 - 20 %, in acceptable accordance with thermodynamic calculations [Mul02b]. The very broad maxima at $2\theta = 29°$ and $47°$ in Fig. 7.1 are reminiscent of a graphite-like amorphous or turbostratic BNC_x phase [Hau04b].

As shown in Fig. 7.10(a), investigations with TEM on AM26 material confirmed that the SiC precipitates are approximately nano-sized spheres embedded in an amorphous (turbostratic) host matrix of BNC_x, as shown by elemental mapping. From image analysis of the TEM micrograph in Fig. 7.10(a) the particle distribution of the SiC crystallites is obtained, as shown in Fig 7.10(b). The particle distribution function can be fitted in good approximation by a log-normal function with a maximum value at a diameter of 12 nm. An average volume-weighted crystal diameter [Nat96] of 29 ± 3 nm is derived, which is in good accordance with the value of 25 ± 3 nm obtained from the present XRD measurements, justifying the application of X-ray diffractometry for the determination of crystallite diameters.

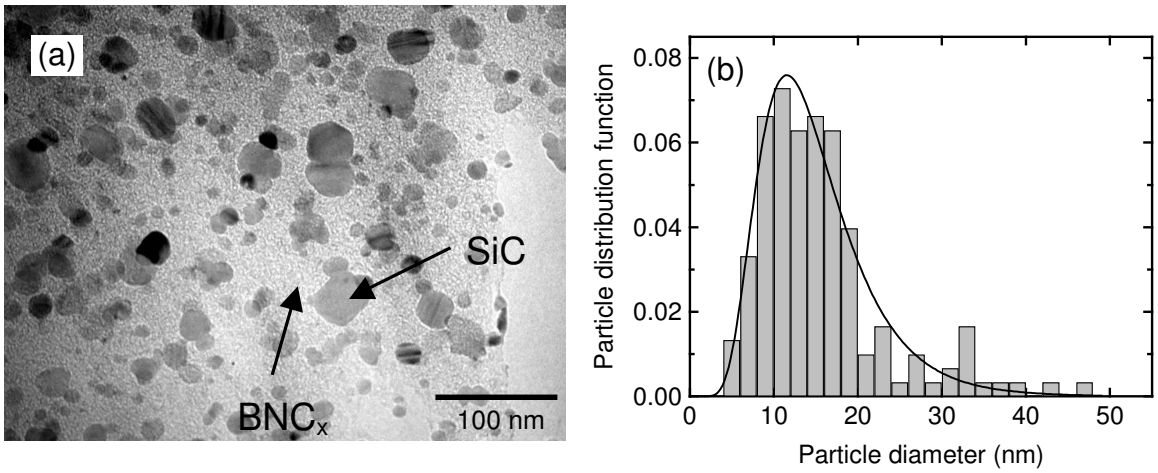

Figure 7.10 (a) TEM image taken from a AM26 sample after annealing for 5 h at 1800 °C. The dark spheres correspond to nano-crystalline SiC which is embedded in a turbostratic BNC_x matrix. **(b)** The particle distribution as determined from the TEM micrograph. The solid line is a least-square fit of a log-normal distribution function to the data.

The annealing time dependence of the integrated peak area, I, as determined by XRD, which is proportional to the crystallized volume fraction χ, and the average crystallite diameter $\langle d \rangle$ are displayed in Fig. 7.11 for a temperature of 1700 °C as a typical example. It can be seen that with increasing annealing time, I increases rapidly in the first 15 min of annealing and remains unchanged afterwards, while $\langle d \rangle$ is broadening continuously. The data can be interpreted in a way that first a very fast crystallization process takes place, where nano-crystalline SiC precipitations are formed first within the first 15 min of annealing. Further annealing leads to a slow growth process of the crystallized particles on a time scale of several hours which can be identified as coarsening. This behaviour is found for all temperatures investigated.

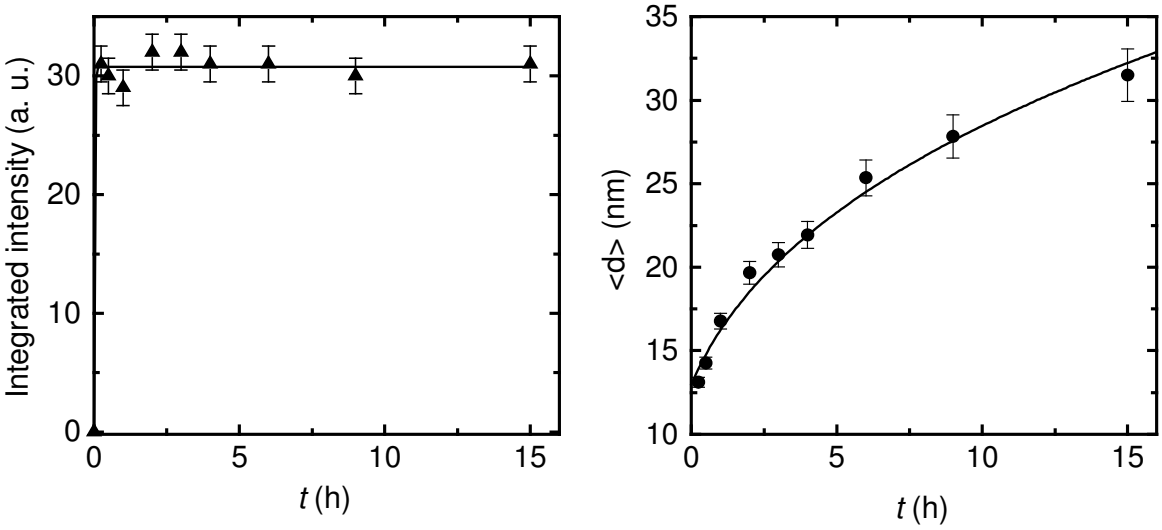

Figure 7.11 (a) Integrated peak intensity (which is proportional to the crystallized SiC fraction) and **(b)** average SiC crystallite diameter as obtained from the SiC Bragg peak at an angle of 71.2 ° as a function of annealing time at 1700 °C for the AM26 material. The lines are a guide to the eye.

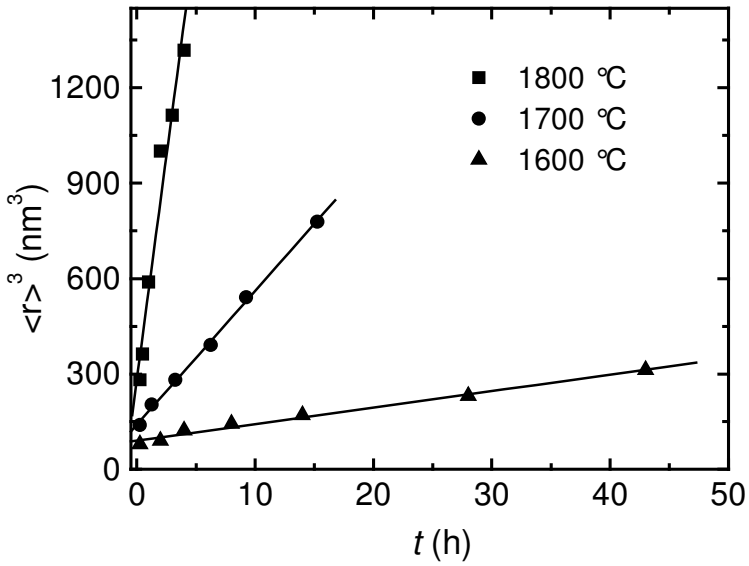

Figure 7.12 Cube of the average grain radius <*r*> plotted as a function of annealing time for the AM26 material at different temperatures. The solid lines are least-squares fits according to Eq. (7.12).

The kinetics of coarsening can be described by the Lifshitz-Slyozov-Wagner (LSW) theory [Lif61, Wag61], where the growth process is driven by a reduction of the overall interfacial energy between crystallite and amorphous matrix. The average crystallite radius at time *t* is given by

$$< r >^3 (t) = r_0^3 + k_C t, \tag{7.12}$$

where r_0 is the crystallite radius at the beginning of the coarsening process and k_C is the temperature dependent rate constant of coarsening. All types of Si-B-C-N ceramics investigated in this study show in good approximation a $\langle r \rangle^3$-behavior, indicating the validity of the LSW theory. As an example, the data of the AM26 material are plotted for consistency with Eq. (7.12) at different temperatures in Fig 7.11.

In contrast, the T21 and MW33 ceramics show a much more complex behaviour of phase formation which is illustrated in Fig. 7.13, exemplarily for the MW33 material. Again, nano-crystalline SiC crystallizes first in a fast process within the first 15 min. Afterwards, in a second crystallization step, starting after about 1 h of annealing, nano-crystalline β-Si_3N_4 and additional SiC is formed.

Generally, a quantitative analysis of the first SiC crystallization step is not possible for all three types of ceramics for temperatures higher than 1600 °C because of a high rate constant of crystallization ($k_{NG} > 10^{-3}$ s^{-1}). The process happens within the first 15 minutes (shortest possible annealing time) and can not be quantitatively resolved with the present experimental equipment. However, an approximate value of $k_{NG} = 5 \times 10^{-4}$ s^{-1} could be determined at 1600 °C, which is plotted together with the data of the Si-C-N system in Fig. 7.5. As obvious, the rate constant is in accordance with a linear extrapolation of the NCP200 data. Since the rate constant of crystallization depends on the self-diffusivity according to Eq. (7.5), it is expected from the Si diffusivity measurements in section 4.2 that crystallization is slower by a factor of four for T21 ceramics compared to VT50 ceramics. This is not reflected in the present measurements on crystallization, which means that this considerably small effect is expected to be compensated by a slightly enhanced nucleation rate due to the different chemical composition.

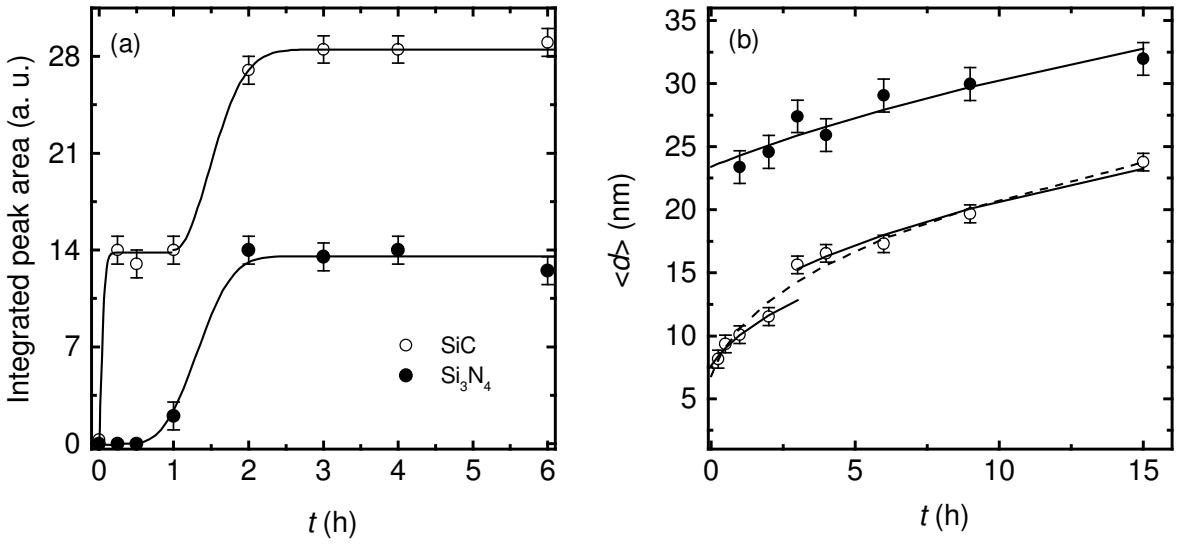

Figure 7.13 (a) Integrated peak area (which is proportional to the crystallized fraction) and **(b)** average crystallite diameter of SiC and β-Si_3N_4 as function of annealing time for MW33 material annealed at 1800 °C. The dashed line corresponds to a fit of all measured data to Eq. (7.12) and the solid lines to a separate fit of the data before and after the second crystallization step.

In contrast, the crystallization rate of the second crystallization step, assessed from the data in Fig. 7.13 at 1800 °C, is considerably lower for Si_3N_4 and SiC (see Fig. 7.5) if extrapolated to lower temperatures. From these results it can be concluded that Si-B-C-N has an increased stability against crystallization due to a retarded and also due to a slower formation of crystalline Si_3N_4 in comparison to Si-C-N. During the formation of β-Si_3N_4, the matrix is depleted in nitrogen and silicon so that a supersaturation with respect to the additional formation of SiC is realized. Thus, SiC crystallizes again in a simultaneous process with Si_3N_4 in analogy to the Si-C-N system. Unfortunately, the analysis of this two step behaviour is restricted only to a temperature of 1800 °C. For lower annealing temperatures a quantitative analysis is not possible because only traces of β-Si_3N_4 phase are formed. At 1900 °C the crystallization of β-Si_3N_4 is so fast that it also occurs within the first 30 min of annealing and a separation of the two crystallization steps is no longer possible. At temperatures below 1600 °C, SiC crystallites with very small average diameters in the order of 1 nm are formed, which is beyond the resolution limit of the XRD apparatus.

In MW33 and T21 ceramics the crystallization process is also superimposed by a coarsening process where the SiC crystallites grow on a slow time scale during annealing (Fig. 7.13 (b)). The rate constants of coarsening determined before and after the second crystallization step, do not differ within an estimated error of $\Delta k_C/k_C = 0.3$. Consequently, the same rate constants are used in both temperature ranges. According to the LSW theory the rate constant of coarsening k_C can be described as [Cal94]

$$k_C\, T = D\frac{8\Gamma V_m c_m (1-c_m)}{9R(c_c - c_m)^2} \tag{7.13}$$

for an ideal solid solution, where c_m is the solubility of Si or C in the amorphous matrix, c_c is the solubility in SiC, V_m is the molar volume of SiC, D is the diffusivity of the slowest component in the matrix, Γ is the interfacial enthalpy, and R is the gas constant. Under the assumption that the solubility in the matrix, c_m, depends only weakly on temperature the diffusivity is the only significant temperature dependent quantity on the right side of Eq. (7.13). A plot of $\log(k_C\, T)$ vs. $1/T$, as depicted in Fig. 7.14, results in a straight line from which the activation enthalpy of coarsening ΔH^C is determined. Values in the order of 7 - 8 eV are obtained (see Appendix/Tab. B.6) showing not much variation for the three ceramics within error bars. These values roughly coincide with the activation enthalpies of self-diffusion (see section 4.3), wherefrom can be concluded that the coarsening behaviour of SiC in Si-B-C-N is also controlled by diffusion in accordance with the LSW theory. The slightly lower value of ΔH^D (about 1 eV) compared to ΔH^C for the T21 and MW33 material can be attributed to the fact that a non-negligible temperature dependence of the Si solubility in Si-B-C-N may play a role. The determination of the rate constant of coarsening for Si_3N_4 is much more difficult to achieve, because the crystallites are generally larger compared to SiC which decreases the sensitivity of determination. The possible presence of

micro-strain could also not completely be excluded here. Nevertheless, as shown in Fig. 7.14 the rate constant of coarsening for Si_3N_4 as measured for the MW33 material at 1800 °C is in the same order of magnitude as for SiC. Using the diffusivities of the T21 ceramic from Fig. 4.5, the rate constants of coarsening from Fig. 7.14, and Γ = 0.6 J/m^2 (as determined in section 7.1), a solubility, c_m, of the atoms in the (already depleted) amorphous matrix between 1 and 0.1 at. % can be assessed, which is quite reasonable.

As shown in Fig. 7.14, the diffusion controlled coarsening rates are in the same order of magnitude for all Si-B-C-N ceramics, which is a further prove for the presence of kinetic processes which are relatively independent of composition. The rate constants of the AM26 material are highest, while those of the T21 and MW33 materials are lower by a factor of about three and of about six, at low temperatures. During the first crystallization step of SiC the composition of the amorphous matrix is modified while an enrichment of nitrogen and boron and a depletion of silicon and carbon takes place. At the end of the crystallization process (and at the beginning of the coarsening process) a modified matrix composition is present. A detailed analysis [Sch05b] shows that the coarsening and consequently the underlying self-diffusion processes in the matrix are slow for high silicon and nitrogen concentrations. The AM26 material, where no additional Si_3N_4 crystallizes, exhibits the highest rate constant.

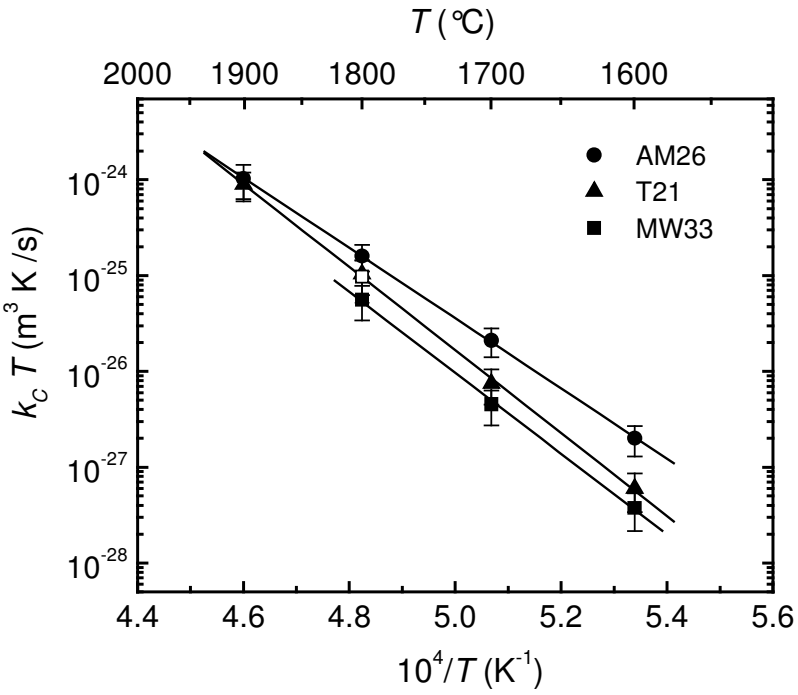

Figure 7.14 Plots of log(k_C T) vs. 1/T describing the coarsening of SiC in Si-B-C-N. The open symbol corresponds to the rate constant of Si_3N_4 in MW33 at 1800 °C.

7.4. High Temperature Stability of Si-(B-)C-N Ceramics

In section 2.1 several possible reasons for the enhanced high temperature stability of Si-B-C-N ceramics in comparison to Si-C-N ceramics are given. With the present measurements a straightforward discussion of this point becomes possible. First, it is necessary to distinguish between (1) the enhanced high temperature stability of the material against decomposition and (2) the enhanced high temperature stability of the amorphous state against crystallization.

First, topic (1) is addressed. More or less all possible reasons given in section 2.1 attribute the enhanced stability of the whole system to an enhanced stability of silicon nitride against decomposition according to Eq. (7.11). This solid state reaction is not observed for Si-B-C-N, where β-Si_3N_4 is still stable at 1900 °C. The reason that the structural disorder present in the amorphous state leads to an enhanced enthalpy of the decomposition reaction is not very plausible, because Si-B-C-N is also stable as a composite, containing crystalline Si_3N_4 during several hours of annealing at 1800 °C (section 7.3). A further possible reason to explain the stability might be that turbostratic BNC_x layers segregated at grain boundaries act as diffusion barriers for N and C, and reaction (7.11) is completely suppressed. The results on coarsening show that long range atomic re-arrangement processes between Si_3N_4 and SiC crystallites take place in the amorphous matrix of partially crystallized ceramics due to diffusional flow, also across such a barrier. However, no decomposition of silicon nitride is observed, which makes that possibility unlikely. Another reason might be that an encapsulation of the Si_3N_4 crystallites with BNC_x phase leads to an enhancement of the local nitrogen partial pressure at the grain surface, which enhances the decomposition temperature significantly. The equilibrium condition of reaction (7.11) can be expressed as

$$\frac{p_{N_2}^2 a_{SiC}^3}{a_{Si_3N_4} a_C^3} = \exp\left(-\frac{\Delta G^0}{RT_e}\right), \tag{7.14}$$

where ΔG^0 is the standard Gibbs free enthalpy, p_{N2} is the nitrogen partial pressure, and a_i is the activity of compound i. The activities of the solid compounds can be set to one and the equilibrium temperature T_e is determined entirely by p_{N2}. As obvious from Eq. (7.14), T_e is shifted to a higher temperature with increasing nitrogen partial pressure. According to thermodynamic calculations [Sei98] a temperature of $T_e > 1900$ °C is reached for $p_{N2} = 30$ bar. To maintain such an internal pressure for long annealing times, it is necessary that nitrogen may not diffuse away from the grain surface across the matrix at high temperatures, which necessitates some kind of diffusion barrier. Despite of this argumentation, it was recently experimentally verified by Friess et al. [Fri04] that the decomposition of Si_3N_4 in VT50 ceramics is a sensitive function of applied external pressure, which indicates that such an effect may play indeed a considerable role for the stability of the present ceramics. To clarify this point exactly, further investigations are still

necessary, especially the determination of rate constants as a function of nitrogen partial pressure. One of the most likely reasons for the enhanced stability is that carbon is completely incorporated in the BNC_x phase and thus has a decreased activity in comparison to elemental carbon. This decreased carbon activity might also shift the decomposition temperature to higher values. According to Eq. (7.14) a decrease of the activity to at least $a_C = 0.1$ (in BNC_x) is necessary to account for the same shift of the equilibrium temperature as for the internal pressure effect, which is quite reasonable.

To attribute topic (2), a comparison of the overall crystallization behaviour of Si-C-N and Si-B-C-N shows that the formation of nano-crystalline SiC occurs for both materials on the same time scale. For Si-C-N this formation is accompanied by a simultaneous crystallization of microcrystalline α-Si_3N_4 with the same rate constant. For Si-B-C-N, however, a retarded and slower formation of nano-crystalline β-Si_3N_4, accompanied by an additional crystallization of SiC is observed. This second crystallization step can be identified as the reason for the better stability of Si-B-C-N against crystallization. Since the rate constants of crystallization depend on the self-diffusivity according to Eq. (7.5), this process should be slower by a factor of four for T21 ceramics compared to VT50 ceramics. However, since the difference in the rate constants of the second crystallization step is at least two orders of magnitude for both types of ceramics, the lower diffusivities cannot account for this effect alone. The decreased rate constant may, however, be rationalized by a smaller driving force of nucleation, $\Delta\mu$, to be present in the modified matrix. The retardation of the crystalline Si_3N_4 formation is unexplained up to now. One can speculate that an incubation time is established, where nucleation without (or with strongly reduced) crystallite growth takes place. To clarify these points, a combined approach of detailed investigations on crystallization (especially in the very early stages where the phase separation in the amorphous state may play a role) and of thermodynamic calculations are necessary.

8. Crystallization of Magnetron Sputtered Si_3N_4 and SiC Films

In this section, the crystallization behaviour of stoichiometric amorphous Si_3N_4 and SiC films is discussed, which were deposited by r. f. magnetron sputtering. For these binary compounds, interface-reaction controlled transformations from amorphous to crystalline state are expected, which are not necessarily influenced by the self-diffusion of the constituting elements. However, as will be shown, self-diffusion and the motion of point defects may play also an important role for these polymorphous transformations. For SiC, the influence of the substrate on the kinetics of crystallization is discussed and a model is proposed which can describe the different crystallization behaviour. The obtained results on SiC and Si_3N_4 films were also used as a reference material for the crystallization of amorphous Si-C-N, as already discussed in section 7.

8.1. Si_3N_4 Films

Stoichiometric silicon nitride films were deposited on SiC substrates as explained in section 3.1.2. After deposition the films are amorphous which was proven by XRD measurements as shown in Fig. 8.1(a). Additional FTIR measurements, which are depicted in Fig 8.1(b), confirm the formation of disordered Si-N bonds as a broad absorption maximum at 820 cm^{-1} [The02]. The chemical composition was determined by RBS. Concentration depth profiles measured with SNMS confirmed the constant ratio of silicon to nitrogen concentration throughout the film. Annealing of the films up to 1700 °C did not change these concentration depth profiles.

Annealing of the Si_3N_4 films in the temperature range between 1300 - 1700 °C in nitrogen leads to the crystallization of a mixture of the two polymorphic modifications α–Si_3N_4 and β–Si_3N_4 (Fig. 8.1(a)), which generally coexist at ambient conditions in sintered ceramics or powders [Ril00]. A relative volume fraction of the β modification, ranging from about 15 % at 1300 °C to slightly more than 40 % at 1700 °C is derived [Sch04a]. No transformation of the α–Si_3N_4 modification to the β–Si_3N_4 modification was observed by post-annealing the corresponding sample at the same temperature or at a higher temperature. The lack of this transformation, which is commonly found in sintered samples, can be attributed to the relatively high purity of the films with a oxygen concentration below 0.2 at. % as determined by n-RBS using the resonance at 3.05 MeV [Bla88]. This presumably leads to the absence of SiN_xO_y grain boundary layers assisting the impurity controlled transformation to β–Si_3N_4 in the solid state (for details see Ref. [Sch04a]). The higher amount of β–Si_3N_4 formed during the crystallization process at higher annealing temperatures can be attributed to the fact that the difference in the Gibbs enthalpy of formation between the α and the β phase $\Delta G^{\alpha/\beta}$ becomes slightly more negative with

increasing temperature [Chi98, Lie01]. Therefore, a greater stability of β–Si_3N_4 compared to α–Si_3N_4 is expected at higher temperatures.

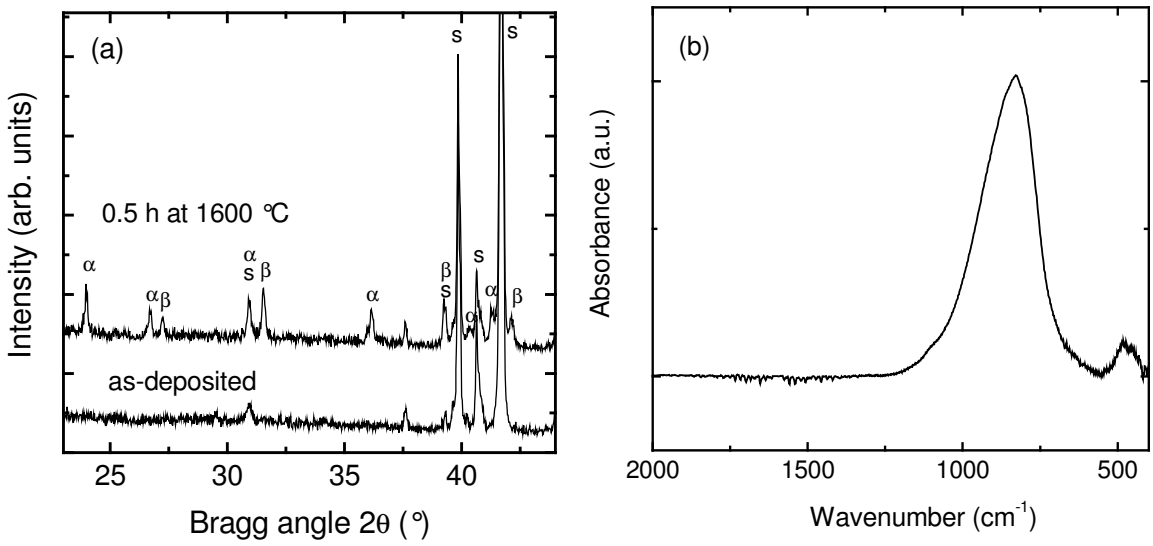

Figure 8.1 (a) X-ray diffractograms of a Si_3N_4 film in the as-deposited state and after annealing for 0.5 h at 1600 °C; α: α-Si_3N_4, β: β-Si_3N_4, and s: substrate. **(b)** FTIR spectrum of a $Si_3{}^{15}N_4$ film in the as-deposited state. The broad peaks at 820 cm^{-1} and 480 cm^{-1} correspond to Si-N bond vibrations and reflect the amorphous state of the material.

An average crystallite diameter of $\langle d \rangle \approx 100$ nm is determined from XRD peaks to be constant within experimental uncertainties during the crystallization process for both modifications. However, since the value of $\beta(2\theta)$ is close to the resolution limit of the X-ray diffractometer, the crystallite diameter has to be understood as a lower limit. In Fig. 8.2 the term $\ln(-\ln(1-\chi(t)))$ is plotted against $\ln(t)$ for partially crystallized α–Si_3N_4 at four annealing temperatures. Least-squares fitting of these data with the JMAK equation (7.4) leads to straight lines with a slope between $n = 2.8$ and 3.1 for the JMAK exponent. This is in good accordance with the theoretically value of $n = 3$, which is expected for a three-dimensional interface-reaction controlled growth process from pre-existing nuclei that governs polymorphic transformation like the crystallization of amorphous Si_3N_4. As demonstrated for a temperature of 1390 °C the crystallization of amorphous Si_3N_4 is a process where the phases α–Si_3N_4 and β–Si_3N_4 are formed simultaneously, with nearly the same rate constant [Sch04a]. Therefore, further analysis is restricted to the behaviour of α–Si_3N_4.

The experimentally determined rate constants for the crystallization of amorphous Si_3N_4 films are shown in Fig. 8.3 as a function of reciprocal temperature. According to the classical nucleation and growth theory, the temperature dependence of the rate constants of crystallization for a interface-reaction controlled growth process from pre-existing nuclei is given by [Chr65]

$$k_{NG} = k_{NG}^{0} exp\left(-\frac{\Delta H^{I}}{k_B T}\right)\left(1 - \exp\left(-\frac{\Delta\mu}{k_B T}\right)\right) \qquad (8.1)$$

where ΔH^{I} is the activation enthalpy for the transfer of an atom across the amorphous-crystalline interface and $\Delta\mu$ is the difference between the chemical potentials of the amorphous and of the crystalline state at the amorphous-crystal interface. Using $\Delta\mu = 0.1$ eV/atom, as measured by florine combustion calorimetry for Si_3N_4 [Tom01], a value of ΔH^{I} = 5.5 ± 0.5 eV and of k_{NG}^{0} = 4 x 10^{12} s^{-1} is determined by fitting Eq. (8.1) to the experimental data. Since the quantity $\Delta\mu/k_B T$ is relatively high, the second term in Eq. (8.1) can be neglected and the growth process can be described in good approximation by a simple Arrhenius behaviour with $\Delta H^{NG} = \Delta H^{I}$ as the activation enthalpy of crystallization. A comparison of this value to the activation enthalpies of 9.2 eV [Yam83] and 3.3 eV [Seh94] determined by other research groups in amorphous Si_3N_4 powders is of minor significance, because of the small temperature range of only 80 °C investigated in Ref. [Yam83] and because of a relatively large scatter of the data points given in Ref. [Seh94].

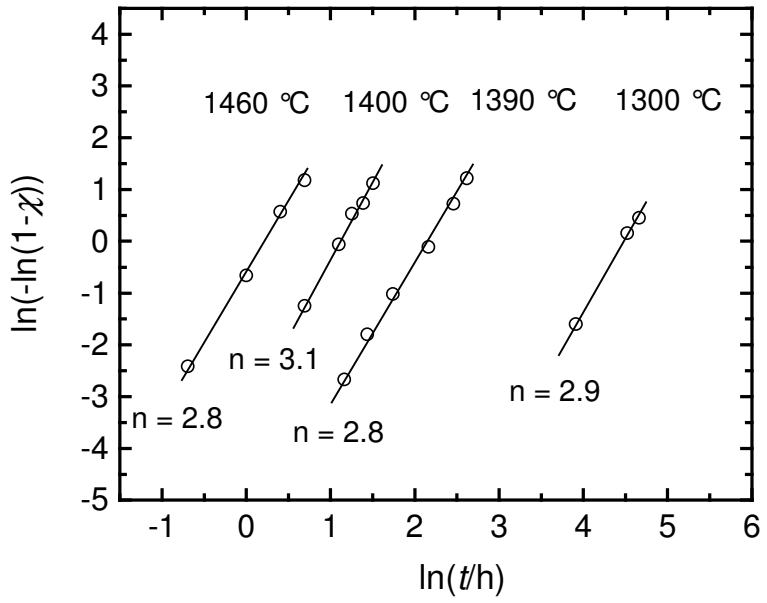

Figure 8.2 JMAK diagrams describing the transformation of amorphous Si_3N_4 to crystalline α–Si_3N_4.

For polymorphic transformations, the quantity ΔH^{I} is essentially unknown. However, a reasonable approximation might be to compare it to the activation enthalpies of self-diffusion in the amorphous and in the crystalline state, which can be seen as approximate values describing the transfer of an atom across the amorphous/crystalline interface. As shown in section 6.2, the activation enthalpies of N and Si self-diffusion are within the range of 4.5 - 5.5 eV, which is identical to the value of ΔH^{I} within error bars. The rate constant of crystallization is now approximated by

$$k_{NG} = u\left(\frac{4\pi}{3}N_0\right)^{1/3} = a\nu_0\left(\frac{4\pi}{3}N_0\right)^{1/3}\exp(\Delta S^{I}/k_B)\ \exp\left(\frac{\Delta H^{I}}{k_B T}\right) \approx \frac{D}{a}\left(\frac{4\pi}{3}N_0\right)^{1/3} \quad (8.2)$$

where u is the rate constant of crystallite growth, $a \approx 0.26$ nm is the approximate distance between Si and N atoms in the crystal lattice, which is about the distance the interface moves per atomic rearrangement, N_0 is the density of pre-existing nuclei (and also crystallites), ν_0 is an attempt frequency, which corresponds approximately to the Debye frequency ν_D, and $\Delta H^I = \Delta H^D$ and $\Delta S^I = \Delta S^D$ are the activation enthalpy and the entropy change of the transfer process, which correspond to the values of self-diffusion. In Fig. 8.3, the rate constants of crystallization as calculated from the nitrogen self-diffusivities in polycrystalline Si_3N_4 according to Eq. (8.2) are displayed, which are in good accordance with the data determined by XRD. For the calculations, values of $N_0 = 2 \times 10^{21}$ m^{-3} or $N_0 = 4 \times 10^{21}$ m^{-3} are used, which are derived from the equation $N_0 = (4\pi/3\ (<d>/2)^3)^{-1}$ for an average diameter of spherical crystallites of $<d> = 100$ nm and 1000 nm, respectively. This result indicates that for the present case of silicon nitride the crystallization process is essentially determined by the kinetic parameters governing self-diffusion, but without being a process which is controlled by long-range diffusion.

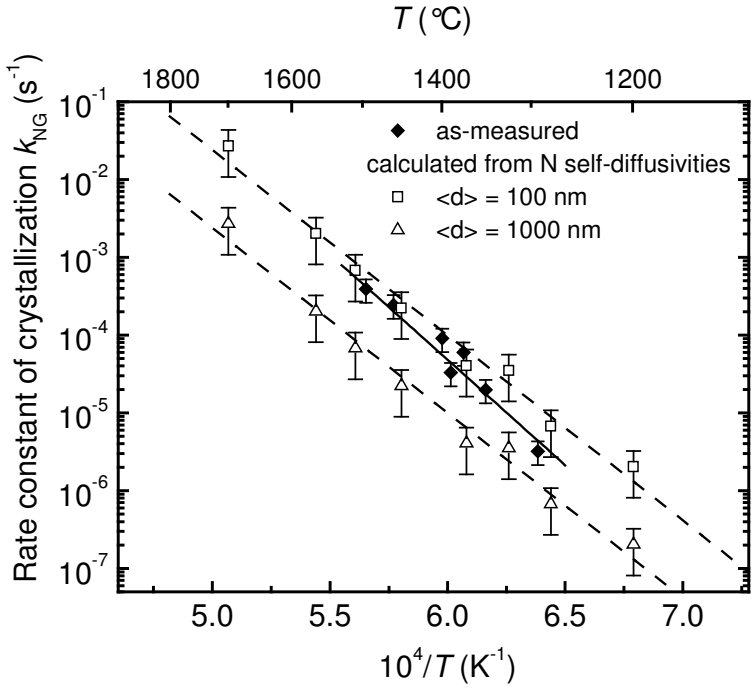

Figure 8.3 Rate constants of crystallization as a function of reciprocal temperature for Si_3N_4 films deposited on SiC substrates. Shown are data directly obtained from XRD measurements in comparison to data calculated according to Eq. (7.2) from the self-diffusivities as measured in section 5. For the calculations average crystallite sizes of 100 nm or 1000 nm are used.

8.2. SiC Films

Analogous experiments as for silicon nitride were carried out for stoichiometric amorphous silicon carbide films. Here, two different substrates were used, single crystalline

silicon wafers and glassy carbon, where a good adhesion of the films was achieved. Details of this work can be found in Refs. [Sch05c, Fot05]. After deposition, the films are amorphous as can be seen in Fig. 8.4, where a high resolution TEM image of an as-deposited film is depicted together with the corresponding SAED patterns as an inset. The diffuse halo of the pattern which can be attributed to the amorphous SiC film is clearly visible. The sharp overlapping spots belong to the Si substrate. In Fig. 8.5 the TEM bright field and dark field images of a SiC film, which was annealed at 1550 °C for 5 h in argon are shown. Crystallites of approximately spherical or ellipsoidal shape with a maximum aspect ratio of about 1:3 and an average diameter between 30 and 70 nm can be identified. A detailed analysis of the crystallite sizes as a function of annealing time from TEM images was not possible due to the bad contrast between crystalline and amorphous material. The crystallized SiC can be identified from the distinct rings of the SAED pattern as polycrystalline material to be present in the cubic β modification with a lattice constant of $a = 4.25 \pm 0.1$ Å. Crystallization is observed for anneals at temperatures above 1200 °C for films on Si substrates and above 1500 °C for films on glassy carbon substrates, respectively. Striking differences in the microstructure of the completely crystallized films were not found in the TEM micrographs for the two types of substrates.

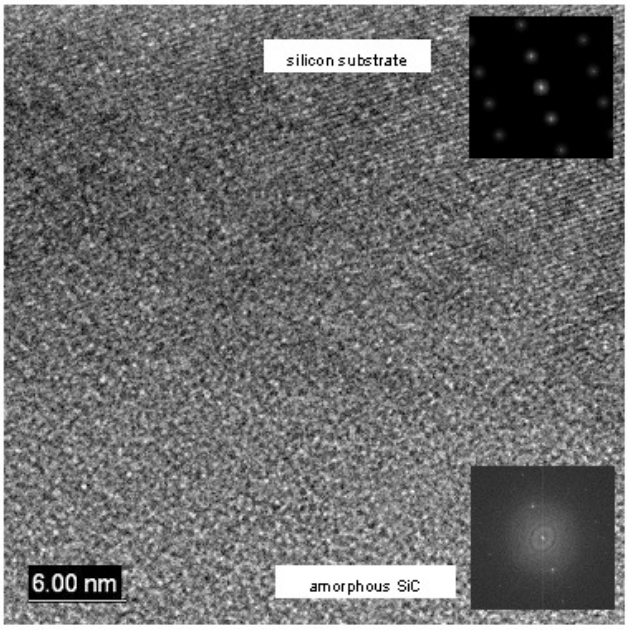

Figure 8.4 High resolution TEM image of the interface between an amorphous SiC film deposited on a single crystalline silicon substrate. The insets show SAED patterns of the silicon substrate and of the amorphous film, respectively.

In analogy to the case of Si_3N_4, the fraction of crystallized SiC χ and the average crystallite radius $\langle r \rangle$ were determined from the XRD patterns as a function of annealing time as shown in Fig. 8.6 for SiC films on glassy carbon substrates at 1550 °C. It can be seen, that with increasing annealing time the crystallized fraction increases continuously until a saturation occurs, corresponding to the complete crystallization of the film. Least-

squares fitting of the crystallized fraction to the JMAK equation (7.4) results in growth exponents between n = 0.8 and 1.2 for different temperatures, corresponding to a one-dimensional interface-reaction controlled growth from pre-existing nuclei [Chr65]. This finding is in strong contrast to the morphology of the crystallites observed by TEM measurements, which strongly suggests that the growth of crystallites is three-dimensional.

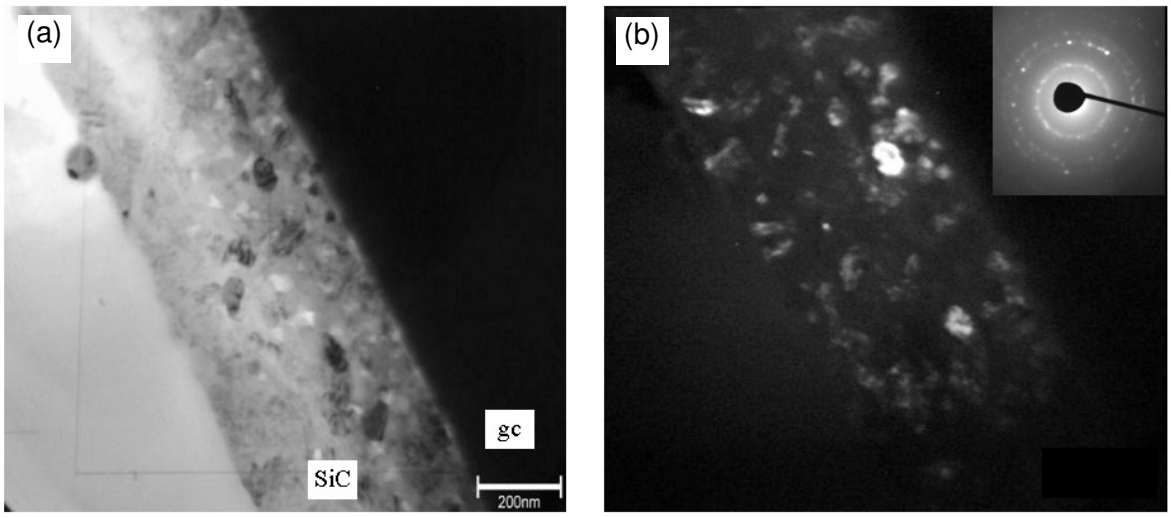

Figure 8.5 TEM bright field **(a)** and dark field **(b)** images of SiC deposited on glassy carbon (gc) and annealed at 1550 °C for 5 h in argon. The insets show the corresponding SAED patterns for polycrystalline β-SiC. Crystallites can be identified as the dark and bright areas in case of **(a)** and **(b)**, respectively.

Fig. 8.6 also shows exemplarily the evolution of the average crystallite radius, $\langle r \rangle$, with time. In the early stages of the crystallization process, the experimental data follow a straight line in accordance with an interface-reaction controlled growth behaviour. In the later stages of the process deviations occur which are due to the impingement of the growing crystallites. Note, that a linear growth characteristic is observed in the same time interval where the crystallized fraction increases significantly. A least-squares fit of the data in Fig. 8.6 to a straight line results in the determination of the rate constant of crystallite growth, u, which is the slope of the straight line. A high average crystallite radius of about 11 nm is found by extrapolating the data to t = 0, indicating that this value cannot be associated with the critical radius of nucleus formation, r_c, which should be in the order of 1 nm (see section 7.1). Consequently, this value has to be interpreted in a different way. It is assumed that prior to the growth process detected by XRD an additional growth process (or nucleation and growth process) takes place in the early stages of crystallization on a time scale which can not be resolved with the present experimental equipment. Thus, a two stage overall process of crystallization is operating. The first process leads to the fast formation of crystallites in the order of 10 nm (e. g. within the first 600 s in case of the data of Fig. 8.6). However, this process is connected only with the formation of a limited amount of

crystalline phase (about 30 %). During the second process, which is takes place with a slower growth rate, the rest of the amorphous material crystallizes.

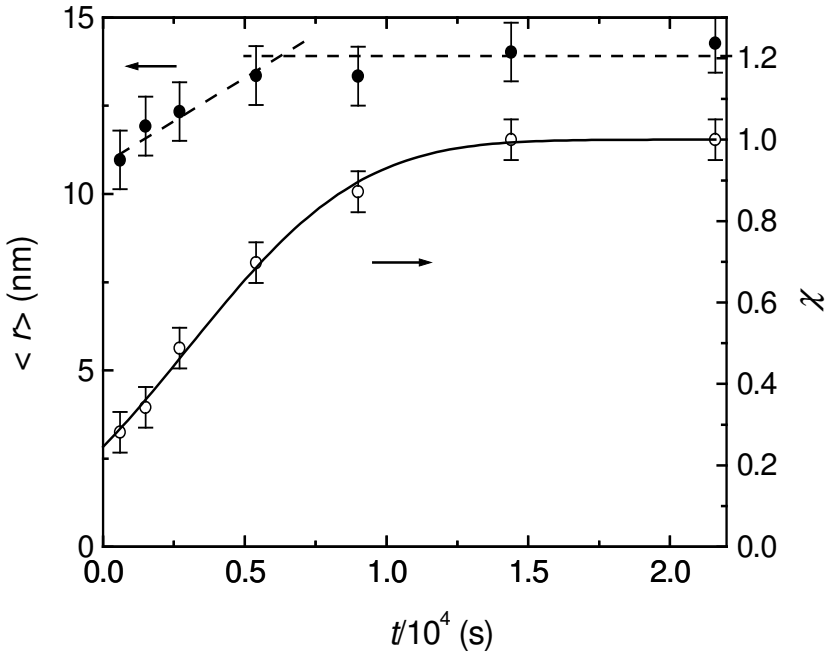

Figure 8.6 Volume fraction of crystallized β-SiC, χ, and average radius of SiC crystallites, <*r*>, as a function of annealing time at 1550 °C for a film deposited on glassy carbon substrate. The solid curve corresponds to a least-squares fit of the experimental data to Eq. (8.3) and the straight line indicates an interface-reaction controlled growth of crystallites. For further details see text.

Because of these findings, the JMAK equation (7.4) has to be modified in order to achieve a correct description of the data. For a growth from pre-existing crystallites (n = 3) the equation

$$\chi(t) = 1 - \exp\left(-\frac{4\pi}{3} N_0 \left(< r^* > + u \ (t - t^*) \right)^3 \right) \tag{8.3}$$

can be derived, where u is the rate constant of crystallite growth, t^* corresponds to the annealing time where the first data point of the crystallized fraction and of the average crystallites radius is measured, and $<r^*> = <r>(t^*)$. Using Eq. (8.3) an excellent description of the time dependence of the crystallized fraction is possible under the consideration of a three-dimensional growth, as shown in Fig. 8.6. Consequently, the value of n ≈ 1, which is determined with the conventional JMAK equation, leads to an erroneous interpretation by a one-dimensional growth process. For the fitting procedure $<r^*>$ = 11 nm and a constant value of N_0 = 9.0 x 10^{22} m^{-3} is used for the density of the crystallites, independent of temperature. This particle density is calculated according to $N_0 = (4\pi/3 <r>^3)^{-1}$, using an average radius of spherical crystallites of <*r*> = 14 nm as obtained by XRD measurements for a complete crystallization of the amorphous film. Consequently, fitting of the experimental data to Eq. (8.3) results in the determination of u as the only free parameter.

For SiC films deposited on Si substrates a similar analysis is applied, which is discussed extensively in Refs. [Sch05c, Fot05].

Using the equation

$$k_{NG} = \left(\frac{4\pi}{3} N_0 \right)^{1/3} u \tag{8.4}$$

the rate constants of crystallization can be calculated from the rate constants of crystallite growth. The rate constants of crystallization are strongly temperature dependent quantities and are plotted in Fig. 8.7 as a function of reciprocal temperature for films on both types of substrates. We have to distinguish the values obtained directly from the growth of the crystallites and from the analysis with Eq. (8.3). The growth rates derived from the latter analysis are higher by a factor of three and six, respectively, than the directly measured values for films on silicon and glassy carbon substrates. The reason for this discrepancy is still unclear at the moment but it can be tentatively attributed to micro-strain, present in the films, that changes during the crystallization process. Thus, the growth rates determined from the full width at half maximum of the Bragg peaks by Eq. (7.1) are underestimated. If, for example, at the beginning of the growth process no micro-strain, ε, is present, and at the end of the process a value of only $\varepsilon = 4 \times 10^{-4}$, a crystallite radius of 17 nm would be present instead of 14 nm for SiC on glassy carbon, as assessed from Eq. (7.2). This can account for the difference in the growth rates, determined by the two methods. The evolution of micro-strain during crystallization can be explained by the different densities of amorphous (2.75 g/cm^3) and crystalline SiC (3.21 g/cm^3) [Hee97]. Unfortunately, an analysis of micro-strain, e. g. due to the Warren-Averbach or the Williamson-Hall method [Klu73] was not possible due to the limited number of Bragg peaks suitable for quantitative analysis. Consequently further discussion is limited to the data obtained from Eq. (8.3).

It is obvious from Fig. 8.7 that the rate constants are considerably higher for the films on Si substrate compared to those on glassy carbon substrate by several orders of magnitude at low temperatures. This means that the crystallization of SiC films does strongly dependent on the type of substrate used for deposition. The rate constants can be described by Arrhenius straight lines. An activation enthalpy of $\Delta H^{NG} = (8.9 \pm 0.9)$ eV and a pre-exponential factor of $k_0 = 4.7 \times 10^{20}$ s^{-1} is obtained for the films on glassy carbon substrates, while for the films on silicon substrate much lower values of the activation enthalpy of $\Delta H^{NG} = (4.1 \pm 0.7)$ eV and of the pre-exponential factor $k_0 = 5.3 \times 10^8$ s^{-1} are found. In literature, two studies on the crystallization kinetics of amorphous SiC films deposited on silicon substrates can be found. Calgano et al. [Cal01] derived an activation enthalpy of 5.1 eV for films produced by plasma enhanced chemical vapour deposition and Inoue et al. [Ino87] gave a value of 5.0 eV for sputter deposited films where crystallization was followed by infra-red spectroscopy in both cases. These activation enthalpies are in acceptable agreement with our value of 4.1 eV for the films on Si substrates.

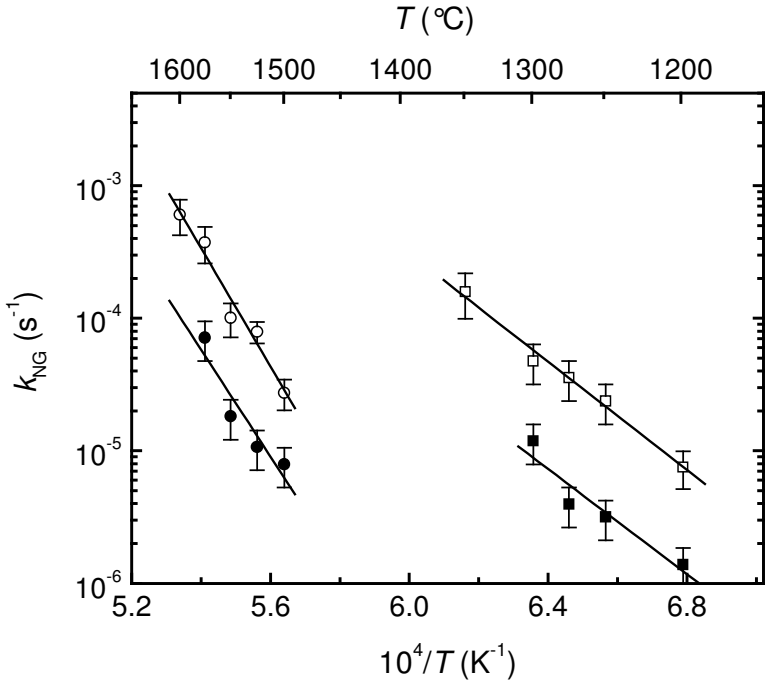

Figure 8.7 Rate constants of crystallization as a function of reciprocal temperature for SiC on Si substrates (squares) and SiC on glassy carbon substrates (circles). The open symbols represent data obtained from least-squares fitting of the modified JMAK model according to Eq. (8.3) and the filled symbols represent the data taken directly from the average crystallite radii.

Applying an analogous argumentation as for the case of silicon nitride, the activation enthalpy of crystallization has to be associated with the activation enthalpy of self-diffusion in SiC. In literature, various self-diffusion data are obtained for SiC single crystals with activation enthalpies between 7.5 and 8.7 eV for C [Rus04, Lin04, Hon79, Hon80a, Hon80b, Hon81] and between 7.2 and 9.5 eV for Si [Rus04, Hon, Hon79, Hon80a, Hon80b, Hon81]. These data are in good agreement with $\Delta H^{NG} = 8.9$ eV for SiC deposited on glassy carbon substrate, indicating that here an intrinsic value is measured. Using the equation

$$k_{NG}^{0} = a\nu_0 \left(\frac{4\pi}{3} N_0\right)^{1/3} \exp(\Delta S^{I} / k_B) \tag{8.5}$$

values of $\Delta S^{I} = (21 \pm 5)\ k_B$ for films on glassy carbon substrates and $\Delta S^{I} = -(6 \pm 3)\ k_B$ for films on Si substrates can be calculated from the experimental data, where $\Delta S^{I} = \Delta S^{D}$. The first value seems to be relatively high, if it is compared to the entropy of self-diffusion in metals [Phi91] or in Si_3N_4 of $\Delta S^{D} = 0 - 4\ k_B$. However, it has to be kept in mind that the entropy of self-diffusion in SiC is also in the order of 20 k_B, as calculated from the pre-exponential factor of $D_0 \approx 10^2$ m^2/s [Hon79, Hon80a, Hon80b, Hon81] according to Eq. (4.6), so that this value is quite reasonable within estimated errors.

In contrast, for SiC films on Si substrate a large negative value of ΔS^{I} is obtained. To explain this, a more detailed look on the self-diffusion mechanism in SiC is necessary.

Under the quite reasonable assumption of a point defect mediated self-diffusion mechanism, the incorporation of an atom from the amorphous into the crystallite phase is assumed to be defect mediated. The activation enthalpy of self-diffusion is then given by $\Delta H^{D} = \Delta H^{f} + \Delta H^{m}$, with ΔH^{f} and ΔH^{m} being the enthalpies of point defect formation and of atomic migration, respectively. The entropy of diffusion $\Delta S^{D} = \Delta S^{f} + \Delta S^{m}$ is also composed of a formation and migration part. The considerably lower activation enthalpy of SiC on Si substrates can now be explained under the assumption that a temperature independent mole fraction of superabundant point defects, c_d, is present in SiC at the temperatures under investigation. These point defects may accelerate the transfer of an atom across the amorphous/crystalline interface. Due to the superabundant point defects, the activation enthalpy of crystallization is now determined by the migration enthalpy of the point defects $\Delta H^{c} \approx \Delta H^{m}$. Assuming $\Delta H^{m} \approx \Delta H^{f} \approx 0.5\ \Delta H^{D}$ as a crude approximation, and ΔH^{D} = 8.9 eV for the films on glassy carbon substrates, a value of $\Delta H^{D} \approx 4.5$ eV is calculated for the films on Si substrates in accordance with the experimentally derived value.

A possible explanation for the presence of superabundant point defects in SiC might be found in the fact that the Si substrate is a point defect source. The temperature where our experiments are carried out is only 100 - 200 °C below the melting point of silicon at 1412 °C. At this temperature appreciably more point defects (vacancies or interstitials) are present in Si than in SiC with a dissociation temperature of 2500 °C [Kom94], which try to equilibrate due to a net point defect flux into the SiC layer. According to Ref. [Tan85] the mole fraction of vacancies and interstitials in silicon is about 2 x 10^{-6} close to the melting point. Using

$$k_{NG}^{0} = a \nu_0 c_d \left(\frac{4\pi}{3} N_0 \right)^{1/3} \exp(\Delta S^{m} / k_B) \qquad (8.6)$$

and ΔS^{m}(Si substrate) $\approx \Delta S^{f}$ (Si substrate) $\approx$ 0.5 ΔS^{I}(glassy carbon substrate) a value of $c_d \approx 10^{-7}$ can be assessed for the mole fraction of superabundant point defects in SiC, which is quite reasonable. In contrast, glassy carbon is stable up to 3000 °C in an inert atmosphere and the point defect concentration has to be relatively low at the temperatures of investigation. Unfortunately, more detailed work on that interesting topic is necessary to verify the mechanism suggested here.

A possible influence of point defects on the crystallization behaviour is also reflected in the first crystallization step of the SiC films, which takes place before the main transformation and may lead to an erroneous interpretation in the framework of the conventional JMAK formalism. Here, it can be speculated that a supersaturation of point defects is present in the amorphous films due to the preparation with magnetron sputtering. These non-equilibrium point defects are equilibrated during the very first stages of annealing. During this time crystallite formation is accelerated.

In conclusion, the present results indicate an interface controlled, but defect mediated growth mechanism for SiC and Si_3N_4 films, where the self-diffusion properties of the elements entirely control the crystallization kinetics. However, self-diffusion is not the rate determining step in this process because long range atomic re-arrangements are not necessary.

9. Summary

In this study, investigations on the self-diffusion and on diffusion controlled processes in amorphous materials of the system Si-C-N (silicon carbide, silicon nitride, and silicon carbonitrides) were carried out at temperatures up to 1900 °C. For analysis, metastable bulk materials and thin films were produced by polymer thermolysis and magnetron sputter deposition. The present work was motivated by the fact that the thermal stability, the microstructure formation, and the long term durability of these high temperature materials depend sensitively on diffusion controlled atomic re-arrangement processes. The results are described by phenomenological models and numerical calculations, which enabled to understand these processes on a fundamental level and to obtain process parameters in order to tailor materials for applications, like e. g. SiC/Si_3N_4 nano-composites.

The first part of this work deals with the investigation of self-diffusion of the elements B, C, N, and Si in polymer-derived amorphous Si-C-N and Si-B-C-N ceramics (precursor ceramics), where conventional methods of tracer deposition are not successfully. The experiments were realized with stable isotopes, which were ion implanted with a high fluence (> 1 x 10^{19} ions/m^2). Complex diffusion profiles were obtained by Secondary Ion Mass Spectrometry (SIMS), which could be not explained with standard models. However, considering the interaction between the tracer and implantation induced defects a numerical simulation became possible. The diffusivities are in the same order of magnitude for ceramics with different composition and for the major constituents, which shows that diffusion controlled processes like crystallization or grain growth are not dominated by one type of element, but are influenced by all elements rather equally. It is further shown that the self-diffusivities exhibit an Arrhenius behaviour in analogy to crystalline materials with high activation enthalpies between 5 and 7 eV and pre-exponential factors between 10^{-3} and 5 m^2/s. In case of silicon and nitrogen diffusion, the results indicate a point defect-like diffusion mechanism via $Si_{3+0.25x}C_xN_{4-x}$ domains in the phase separated amorphous structure, which was identified by comparison to the results on amorphous Si_3N_4. A discussion of the diffusion data in relation to other classes of materials (metals, semiconductors, metallic glasses, silicates) revealed that short-range ordered SiN_4 tetrahedra seem to be a key structure element which governs diffusion in Si_3N_4 based materials.

In order to quantify the self-diffusivities in Si_3N_4, isotope heterostructures were used. Here, the tracer is introduced into the system in-situ during the synthesis with magnetron sputtering, where isotope enriched nanometer sized layers of the form $^{28}Si_3{}^{14}N_4/Si_3{}^{15}N_4/^{28}Si_3{}^{14}N_4$ are deposited on high temperature stable SiC substrates. During annealing, the various layers interdiffuse and the diffusivities were determined by high resolution SIMS or NRRA analysis over a wide temperature range between 1100 and 1700 °C and down to values of 10^{-23} m^2/s. The two elements Si and N are found to diffuse via a common diffusion mechanism with an activation enthalpy of about 5 eV. This result can be explained with the assumption of a divacancy as the responsible diffusion mediating defect.

The main advantages of isotope heterostructures are that the diffusing stable isotopes can be detected over a wide concentration range from 1 to 100 % (in contrast to ion implanted isotopes), that oxide formation at the film surface does not influence the detection of the diffusion process in the interior of the film, and that an undisturbed tracer exchange through interfaces is enabled (in contrast to tracer deposition from the gas phase). With the present method it was possible to realize the first successful experiments on covalent ceramics where the self-diffusivities in the amorphous and in the polycrystalline state were measured in direct comparison. The diffusivities in the amorphous state are only slightly enhanced by a factor of five in comparison to the crystalline state, which indicates a similar diffusion mechanism due to a similar short-range order.

A further central theme of the present thesis is the characterization of hydrogen migration in amorphous Si-(B-)C-N, SiC, and Si_3N_4 films and bulk materials in the temperature range between 600 and 1150 °C. The element hydrogen is present in these materials in the per cent range in addition to the main elements. Its mobility controls the hydrogen content of the material, which is the determining factor for stress relaxation in the amorphous structure and for the compensation of electronic defects like dangling bonds in order to enable electronic and optoelectronic applications. For magnetron sputtered Si_3N_4 films, hydrogen diffusion was investigated exemplary as a function of pre-annealing state, hydrogen content, and thermodynamic state. The results were interpreted in the framework of a trap-limited diffusion mechanism. Here, the migration of hydrogen is described by an effective diffusivity and by temporary trapping of hydrogen at Si, C, and N dangling bonds, in strong contrast to single crystalline materials. High activation enthalpies up to 3.5 eV were obtained and the hydrogen concentration of the samples was identified to be a sensitive factor which influences atomic motion. The hydrogen diffusivities in SiC were found to be nearly identical with those of Si_3N_4 if compared for the same hydrogen concentration, an observation which can be also understood in the framework of a trap-limited diffusion mechanism. For Si-(B-)C-N precursor ceramics, hydrogen diffusion in the phase separated amorphous structure can be classified into two categories, where migration takes place via domains with strongly different effective diffusivities. Fast hydrogen diffusion with an activation enthalpy of about 0.5 eV occurs along amorphous BNC_x domains where most of the trapping sites are saturated. In contrast, slow diffusion with an activation enthalpy of 2 eV takes place along amorphous $Si_{3+0.25x}C_xN_{4-x}$ domains where a considerably amount of unsaturated traps exists. Comparing all materials investigated, a wide range of activation enthalpies (0.3 - 4 eV) and of pre-exponential factors (10^{-14} -10^{-2} m^2/s) were found to obey a compensation law. This can be explained under the assumption that both quantities are directly related to a temperature dependent hydrogen chemical potential.

In the final main part of the work, the phase formation of crystalline precipitations in a supersaturated amorphous Si-(B-)C-N matrix and the underlying kinetic processes were investigated by XRD as a function of annealing time and by TEM. It is shown that crystalline phase formation is governed by several superimposed processes. For the boron

free Si-C-N system, phase formation can be described by simultaneous crystallization of micro-crystalline α-Si_3N_4 and nano-crystalline SiC according to the JMAK formalism, assuming a diffusion controlled crystallite growth with a nearly constant nucleation rate. The determined rate constants of crystallization show an Arrhenius behaviour with a very high activation enthalpy of about 13 eV, where the enthalpies of self-diffusion and nucleation contribute substantially to that value. The high activation enthalpy is identified to be the reason for the extreme stability of the amorphous state in these materials. In addition, a solid state reaction contributes to phase formation, where α-Si_3N_4 reacts with amorphous carbon to SiC and nitrogen which leads to a decomposition of the ceramics at temperatures higher than 1500 °C by loss of gaseous nitrogen. However, the rate constant of this process is lower than the rate constant of crystallization. This implies that a de-mixing of the amorphous state occurs before crystallization by nucleation of separate SiC and Si_3N_4 particles, which simultaneously grow in order to form SiC/Si_3N_4 nano-composites.

In contrast, for the Si-B-C-N system the formation of nano-crystalline SiC and nano-crystalline β-Si_3N_4 is observed, occurring in a stepwise process: first SiC particles crystallize with a rate constant comparable to the Si-C-N system. During further annealing, in a second crystallization step β-Si_3N_4 and additional SiC is formed. This retarded crystallization seems to be the reason for an enhanced stability of amorphous Si-B-C-N at high temperatures. In these ceramics the microstructural evolution is also strongly influenced by a diffusion controlled coarsening process superimposed on the crystallization steps. Here, Si_3N_4 and SiC crystallites grow very slowly on a time scale of hours or days at very high temperatures due to a reduction of interfacial energy, a phenomenon which determines the long term stability of the formed nano-composites. In light of the present results, possible reasons for the enhanced high temperature stability of crystalline Si-B-C-N in comparison to Si-C-N are discussed.

At last, polymorphic transformations from amorphous to crystalline state were investigated for Si_3N_4 and SiC films. Here, the classical nucleation and growth theory was applied, where crystallites grow by a three-dimensional interface-reaction controlled process from pre-existing nuclei. Analysis of the thermally activated crystallization rates led to the conclusion that crystallite growth is governed by single atom jumps over the amorphous/crystalline phase boundary. This process is determined by the self-diffusivities of the constituents, however, without the necessity of long-range atomic re-arrangements of atoms. Tremendous differences were found for the thermal stability of SiC films deposited on different substrates which were explained by a point defect-mediated growth process and defect equilibration between film and substrate.

In conclusion, the present work gives a comprehensive overview on the fundamental properties of diffusion controlled processes in metastable amorphous materials of the system Si-C-N.

10. Acknowledgements

First of all, I would like to thank Prof. Dr. Günter Borchardt for his continuous interest in this work, which he always supported generously. The intensive discussions, his suggestions, and the critical reading of the manuscript helped to advance this study. All the members of the working group “Thermochemie und Mikrokinetik I” are thanked for the excellent working atmosphere, for many helpful discussions, and for the co-operation in daily laboratory work. Especially, Dr. Lars Dörrer and Dr. Peter Fielitz have to be mentioned for their technical support during SIMS analysis. I also express my gratitude to the doctorate students Wolfgang Gruber and Roland Fotsing. The extent of this work would be smaller without their help. Also thanked are the former students Alain Ndjampoup, Gaëtan Le Gall, and Dragana Stojic. I would also acknowledge the members of the electronics, mechanical, and ceramics workshop of the Institut für Metallurgie for their prompt and reliable delivery of complicate parts and repairs. Especially mentioned should be Eberhard Ebeling for his help.

I am very obliged to Dr. Horst Baumann and Dr. Mario Rudolphi from the Institut für Kernphysik (Universität Frankfurt) for the possibility to carry out the ion implantations, the NRRA, and the n-RBS measurements at Frankfurt as well as for the gentle hospitality and for the fruitful discussions during my stays in Frankfurt. The boron implantations were realized at the Université de Paris-Sud by Dr. Bernard Lesage and Odilie Kaïtasov, thank you also here. Special thanks are also addressed to Dr. Michael Bruns and Udo Geckle from the Forschungszentrum Karlsruhe for their fruitful co-operation in depositing the magnetron sputtered films and the isotope heterostructures.

I would also address a "extra-grand merci" to Sylvain Weber, Prof. Hubert Scherrer, and Prof. Stanislas Scherrer from the Ecole des Mines de Nancy in France, where I stayed for several weeks in order to carry out investigations with SIMS/SNMS. It is always a nice time to be there.

Special thanks also to Dr. Anita Müller, Dr. Joachim Bill, Dr. Markus Weinmann, and Peter Gerstel from the MPI für Metallforschung in Stuttgart for the synthesis of the polymer-derived Si-B-C-N ceramics and for the interesting discussions in the framework of the DFG main program "Percursorkeramiken".

Further, Dr. Sébastien Chevalier and Dr. Remy Chassagnon (Université de Bourgogne, Dijon, France) are thanked for the possibility to use their TEM equipment and for the co-operation. Dr. Nantasha Bunjes (MPI-MF Stuttgart) is also thanked for supplying a TEM image, Prof. Dr. Sigfried Hofmann (MPI-FF Stuttgart) for the possibility to use his MRI program, and Sabine Stöckel (TU Chemnitz) for allocating the B-N-C layers.

The Deutsche Forschungsgemeinschaft is gratefully acknowledged for the financial support of this work.

11. References

[Agn00] O. P. Agnihotri, S. C. Jain, J. Poortmans, J. Szlufcik, G. Beaucarne, J. Nijs, R. Mertens, Semicond. Sci. Technol. 15 (2000), R29.

[Ald98] F. Aldinger, M. Weinmann, J. Bill, Pure Appl. Chem. 70 (1998), 439.

[Ali02] Z. Alizadeh, K. B. Sundaram, J. Mat. Sci. Lett. 21 (2002), 7.

[Ama99] B. Amadon, F. Finocchi, Eur. Phys. J. B 11 (1999), 207.

[Amb98] O. Ambacher, F. Freudenberg, R. Dimitrov, H. Angerer, M. Stutzmann, Jpn. J. Appl. Phys. 37 (1998), 2416.

[An98] L. An, R. Riedel, C. Konetschny, H. J. Kleebe, R. Raj, J. Am. Ceram. Soc. 81 (1998), 1349.

[An04] L. An, Y. Wang, L. Bharadwaj, L. Zhang, Y. Fan, D. Jiang, Y. Sohn, V. H. Desai, J. Kapat, L. C. Chow, Adv. Eng. Mat. 6 (2004), 337.

[Arn93] W. M. Arnoldbik, C. H. M. Maree, A. J. H. Maas, M. J. van den Boogaard, F. H. M. Habraken, A. E. T. Kuiper, Phys. Rev. B 48 (1993), 5444.

[Atk94] A. Atkinson in: *Materials Science and Technology Vol. 11*, M. Swain (ed.), (VCH, Weinheim, 1994), p. 295.

[Avr39] M. Avrami, J. Chem. Phys. 7 (1939), 416.

[Avr40] M. Avrami, J. Chem. Phys. 8 (1940), 212.

[Avr41] M. Avrami, J. Chem. Phys. 9 (1941), 177.

[Bad98] A. Badzian, T. Badzian, Diamond Relat. Mater. 7 (1998), 1519.

[Bak96] S. M. Baker, G. S. Smith, N. J. S. Brown, M. Nastasi, K. Hubbard, Phys. Rev. B 55 (1996), 7255.

[Bal94a] H.-P. Baldus, G. Passing, Mater. Res. Soc. Symp. Proc 346 (1994), 617.

[Bal94b] H.-P. Baldus, M. Jansen, O. Wagner, Key Eng. Mater. 89-91 (1994), 75.

[Bal97] H.-P. Baldus, M. Jansen, Angew. Chem. 109 (1997), 338.

[Bar97] M. W. Barsoum, *Fundamentals of Ceramics,* (Mc Graw-Hill, New York, 1997), p. 441.

[Bau01] A. Bauer, M. Christ, A. Zimmermann, F. Aldinger, J. Am. Ceram. Soc. 84 (2001), 2203.

[Bej97] F. Béjina, O. Jaoul, Earth Plan. Sci. Lett. 153 (1997), 229.

[Ben87] A. Benninghoven, H. W. Werner, F. G. Rüdenauer, *Secondary Ion Mass Spectrometry: Basic Concepts, Instrumental Aspects, Applications and Trends* (Wiley, New York, 1987).

[Ben97] A. Bendeddouche, R. Berjoan, E. Beche, T. Merle-Mejean, S. Schamm, V. Serin, G. Tailades, R. Hillel, J. Appl. Phys. 81 (1997), 614.

[Ber01] T. Berlind, N. Hellgren, M. P. Johansson, L. Hultman, Surf. Coat. Tech. 141 (2001), 145.

[Bey97] W. Beyer, Phys. Stat. Sol. A 159 (1997), 53.

[Bey99] W. Beyer in: *Semiconductors and Semimetals Vol. 61*, N. H. Nickel (ed.), (Academic Press, San Diego, 1999), p. 165.

[Bey03] W. Beyer, Sol. Energ. Mat. Sol. C 78 (2003), 235.

[Bha04] L. Bharadwaj, Y. Fan, L. Zhang, D. Jiang, L. An, J. Am. Ceram. Soc. 87 (2004), 483.

[Bil95] J. Bill, F. Aldinger, Adv. Mat. 7 (1995), 775.

[Bil96] J. Bill, F. Aldinger, Z. Metallkd. 87 (1996), 827.

[Bil98] J. Bill, J. Seitz, G. Thurn, J. Dürr, L. Canel, B. Z. Janos, A. Jalowiecki, D. Sauter, S. Schempp, H.-P. Lamparter, J. Mayer, F. Aldinger, Phys. Stat. Sol. 166 (1998), 269.

[Bil99] J. Bill, F. Wakai, F. Aldinger (eds.), *Precursor-Derived Ceramics,* (Wiley-VCH, Weinheim, 1999).

[Bil00] J. Bill, J. Schumacher, K. Müller, S. Schempp, J. Seitz, J. Dürr, H.-P. Lamparter, J. Golczewski, J. Peng, H. J. Seifert, F. Aldinger, Z. Metallk. 91 (2000), 335.

[Bil01] J. Bill, T. W. Kamphowe, A. Müller, T. Wichmann, A. Zern, A. Jalowieki, J. Mayer, M. Weinmann, J. Schuhmacher, K. Müller, J. Peng, H. J. Seifert, F. Aldinger, Appl. Organomet. Chem. 15 (2001), 777.

[Bis98] R. Biswas, Q. Li, B. C. Pan, Y. Yoon, Phys. Rev. B 57 (1998), 2253.

[Bla88] B. Blanpain, P. Revesz, L. R. Doolittle, K. H. Purser, J. W. Mayer, Nucl. Instr. Meth. B 34 (1988), 459.

[Bon89] D. A. Bonnel, T. Y. Tien (Eds.), *Preparation and Properties of Silicon Nitride-Based Materials*, Materials Science Forum Vol. 47, (Trans Tech Publ., Aedermannsdorf, 1989).

[Bra93] H. M. Branz, S. E. Asher, B. P. Nelson, Phys. Rev. B. 47 (1993), 7061.

[Bra98] H. Bracht, E. E. Haller, R. Clark-Phelps, Phys. Rev. Lett. 81 (1998), 393.

[Bra99a] H. Bracht, E. E. Haller, K. Eberl, M. Cardona, Appl. Phys. Lett. 74, (1999), 49.

[Bra99b] H. Bracht, M. Norseng, E. E. Haller, K. Eberl, M. Cardona, Sol. State Commun. 112 (1999), 301.

[Bra00] H. Bracht, S. P. Nicols, W. Walukiewicz, J. P. Silveira, F. Briones, E. E. Haller, Nature 408 (2000), 69.

[Bri83] D. Briggs, M. P. Seah, *Practical Surface Analysis Vol. 2 – Ion and Neutral Spectroscopy* (Wiley, New York, 1983).

[Brn99] H. M. Branz, Phys. Rev. B 60 (1999), 7725.

[Bru85] R. Brutsch, Thin Solid Films, 126 (1985), 313.

[Bul96] J. N. Bullock, C. Bechinger, D. K. Benson, H. M. Branz, J. Non-Cryst. Sol. 198-200 (1996), 1163.

[Bus00] R. Busch, JOM 52 (2000), 39.

[But00] E. Butchereit, K. G. Nickel, Key Eng. Mater. 175-176 (2000), 69.

[But01] E. Butchereit, K. G. Nickel, J. Am. Ceram. Soc. 84 (2001), 2184.

[Cai01] Y. Cai, S. Prinz, A. Zimmermann, A. Zern, F. Phillipp, F. Aldinger, Scr. Mater. 45 (2001), 1301.

[Cal94] H. A. Calderon, P. W. Voorhees, J. L. Murray, G. Kostorz, Acta Metall. Mater. 42 (1994), 991.

[Cal01] L. Calcgano, P. Musumeci, F. Rocaforte, C. Bongiorno, G. Foti, Appl. Surf. Sci. 184 (2001), 123.

[Car78] D. E. Carlson, C. W. Magee, Appl. Phys. Lett. 33 (1978), 81.

[Cau78] R. A. Causey, J. D. Fowler, C. Ravanbakht, T. S. Ellman, K. Verghese, J. Am. Ceram. Soc. 61 (1978), 221.

[Cau93] R. A. Causey, W. R. Wampler, J. R. Retelle, J. L. Kaae, J. Nuc. Mat. 203 (1993), 196.

[Che94] J. Chevallier, *Hydrogen in Compound Semicondictors,* (Trans Tech Publications, Switzerland, 1994), p. 219.

[Che96] L. C. Chen, C. Y. Yang, D. M. Bhusari, K. H. Chen, M. C. Lin, J. C. Lin, T. J. Guang, Diamond Relat. Mater. 5 (1996), 514.

[Che98] L. C. Chen, C. K. Chen, S. L. Wei, D. M. Bhusari, K. H. Chen, Y. F. Chen, Y. C. Yong, Y. S. Huang, Appl. Phys. Lett. 72 (1998), 2463.

[Che99] L. C. Chen, K. H. Chen, S. L. Wei, P. D. Kichambare, J. J. Wu, T. R. Lu, C. T. Kuo, Thin Solid Films 355-356 (1999), 112.

[Chi98] W. Ching, Y. Xu, J. D. Gale, M. Rühle, J. Am. Ceram. Soc. 81 (1998), 3199.

[Chr65] J. W. Christian in: *Physical Metallurgy*, R.W. Cahn (ed.), (North Holland, Amsterdam, 1965), 443.

[Chr75] J. W. Christian, *The Theory of Transformations in Metals and Alloys* (Pergamon Press, Oxford, 1975).

[Chr00] M. Christ, G. Thurn, G. Weinmann, J. Bill, F. Aldinger, J. Am. Ceram. Soc. 83 (2000), 3025.

[Chr01a] M. Christ, A. Zimmermann, A. Zern, M. Weinmann, F. Aldinger, J. Mat. Sci. 36 (2001), 5767.

[Chr01b] M. Christ, A. Zimmermann, F. Aldinger, J. Mat. Res. 16 (2001), 1994.

[Chu78] W.-K. Chu, J. W. Mayer, M.-A. Nicolet, *Backscattering Spectrometry* (Academic Press, New York, 1978).

[Col97] P. Colombo, T. E. Paulson, C. G. Pantano, J. Am. Ceram. Soc. 80 (1997), 2333.

[Cra75] J. Crank, *The Mathematics of Diffusion* (Oxford Univ. Press, Oxford, 1975).

[Dav93] R. F. Davis, Am. Cer. Soc. Bul. 72 (1993), 99.

[Doo86] L. R. Doolittle, Nucl. Instr. Methods B 15 (1986), 227.

[Due84] R. Dübgen, G. Popp, Z. Werkstofftech. 15 (1984), 331.

[Dur97] J. Dürr, S. Schempp, P. Lamparter, J. Bill, S. Steeb, F. Aldinger, Sol. State Ion. 101 (1997), 1041.

[Dur98] J. Dürr, P. Lamparter, J. Bill, S. Steeb, F. Aldinger, J. Non-Cryst. Sol. 232 (1998), 155.

[Fau03] F. Faupel, W. Frank, M.-P. Macht, H. Mehrer, V. Naundorf, K. Rätzke, H. R. Schober, S. K. Sharma, H. Teichler, Rev. Mod. Phys. 75 (2003), 238.

[Fed02] P. A. Fedders, J. Non-Cryst. Sol. 299-302 (2002), 201.

[Fel66] W. Feller, *An Introduction to Probability Theory and its Applications Vol. 2* (Wiley, New York, 1966).

[Fie01] P. Fielitz, G. Borchardt, Sol. State Ion. 144 (2001), 71.

[Fis02] A. Fissel in: *Recent Research Developments in Material Science and Engineering Vol. 1, Part 1,* S. G. Pandalai (ed.) (Transworld Research Network, Fort P. O., Trivandrum, 2002), p. 277.

[Fly72] C. P. Flynn, *Point Defects and Diffusion* (Clarendon, Oxford, 1972).

[Fot01] G. Foti, Appl. Surf. Sci. 184 (2001), 20.

[Fot05] E. R. Fotsing*, Phase Transformation Kinetics and Microstructure of Carbide and Boride Based Ceramics*, doctoral thesis, (Technische Universität Clausthal, Germany, 2005).

[Fra84] W. Frank, U. M. Gösele, H. Mehrer, A. Seeger, *Diffusion in Crystalline Solids*, (Academic Press, New York, 1984), 53.

[Fra91] W. Frank, Diff. Def. Forum 75 (1991), 121.

[Fra92] W. Frank in: *Crucial Issues in Semiconductor Materials and Processing Technologies,* S. Coffa, F. Priolo, E. Rimini, J. M. Poate (eds.), NATO ASI Series E: Applied Sciences Vol. 222 (Kluwer, Dordrecht, 1992), p. 383.

[Fri94] M. Friess, *Untersuchungen an ternären und quaternären Silicium(Element) carbidnitriden: Synthese und Kristallisation zu Verbundkeramiken mit definiertem Gefüge*, doctoral thesis (Universität Stuttgart, Germany, 1994).

[Fri02] M. Friess, J. Bill, J. Golczewski, A. Zimmermann, F. Aldinger, R. Riedel, R. Raj, J. Am. Ceram. Soc. 85 (2002), 2587.

[Fuc95] H. D. Fuchs, W. Walukiewicz, E. E. Haller, W. Dondl, R. Schorer, G. Abstreiter, A. I. Rudnev, A. V. Tikhomirov, V. I. Ozhogin, Phys. Rev. B 51, (1995), 16817.

[Fuj98] H. Fujiwara, J. Koh, Y. Lee, C. R. Wronski, R. W. Collins, J. Appl. Phys. 84 (1998), 2278.

[Fuy89] T. Fuyuki, M. Nakayama, T. Yoshinobu, H. Shiomi, R. Matsunami, J. Cryst. Growth 95 (1989), 461.

[Gha99] R. Gharbi, M. Fathallah, C. F. Pirri, E. Tresso, G. Grovini, F. Giorgis, Can. J. Phys. (1999), 699.

[Gil98] M. D. Giles, S. Yu, H. Kennel, P. A. Packan, Sol. State Technol. 41 (1998), 97.

[Gol92] I. Golecki, F. Reidinger, J. Marti, Appl. Phys. Lett. 60 (1992), 1703.

[Gol04] J. A. Golczewski, F. Aldinger, J. Non-Cryst. Sol. 247 (2004), 204.

[Gom96] F. J. Gomez, P. Prieto, E. Elizalde, J. Piqueras, Appl. Phys. Lett. 69 (1996), 773.

[Gre97] A. Greiner, *Keramiken aus Silylcarbodiimiden,* doctoral thesis, (Technische Hochschule Darmstadt, Germany, 1997).

[Gru05a] W. Gruber*, Haftstellenverzögerte Diffusion von Wasserstoff in Si-(B-)C-N*, doctoral thesis (Technische Universität Clausthal, Germany, 2005).

[Gru05b] W. Gruber, G. Borchardt, H. Schmidt, M. Rudolphi, H. Baumann, P. Gerstel, A. Müller, Def. Diff. Forum 237- 240 (2005), 414.

[Gup04a] M. Gupta, A. Gupta, J. Stahn, M. Horisberger, T. Guberlet, P. Allenspach, Phys. Rev B 70 (2004), 184206.

[Gup04b] A. Gupta, M. Gupta, S. Rajagopalan, A. K. Balamurgan, A. K. Tyagi, U. Pietsch, S. Ayachit, J. Non-Cryst. Solids 343 (2004), 39.

[Hab94] F. H. P. M. Habraken, A. E. T. Kuiper, Mater. Sci. Eng. Rep. 12 (1994), 123.

[Hag90] A. M. Haghiri-Gosnet, F. Rousseaux, B. Kebabi, F. R. Ladan, C. Mayeux, A. Madouri, D. Decanini, J. Bourneix, F. Carcenac, H. Launois, B. Wisniewski, E. Gat, J. Durand, *J. Vac. Sci. Tech. B* 8 (1990), 1562.

[Ham88] H. Hamakawa, D. Kruangam, M. Deguchi, Y. Hattori, T. Toyama, H. Okamoto, Appl. Surf. Sci. 33-34 (1988), 1142.

[Ham94] S. Hampshire, in: *Materials Science and Technology Vol. 11*, M. Swain, (ed.) (VCH, Weinheim, 1994), p. 122.

[Hau04a] J. Haug, P. Lamparter, M. Weinmann, F. Aldinger, Chem. Mater. 16 (2004), 72.

[Hau04b] J. Haug, P. Lamparter, M. Weinmann, F. Aldinger, Chem. Mater. 16 (2004), 83.

[Har01] C. I. Harris, S. Savage, A. Konstantinov, M. Bakowski, P. Ericson, Appl. Surf. Sci. 184 (2001), 393.

[Hee97] V. Heera, F. Prokert, N. Schell, H. Seifarth, W. Kukarek, M. Volskow, W. Skorupa, Appl. Phys. Lett. 70 (1997), 3531.

[Her01] A. M. Hermann, Y. T. Wang, P. A. Ramakrishnan, D. Balzar, L. An, C. Haluschka, R. Riedel, J. Am. Ceram. Soc. 84 (2001), 2260.

[Heu92] A. T. Heumann, *Diffusion in Metallen* (Springer, Berlin, 1992).

[Hir79] Y. Hirohata, M. Kobayashi, S. Maeda, Thin Solid Films. 63 (1979), 237.

[Hof00] S. Hofmann, Surf. Interf. Anal. 30 (2000), 228.

[Hon79] M. H. Hon, R. F. Davis, J. Mater. Sci. 14 (1979), 2411.

[Hon80a] M. H. Hon, R. F. Davis, D. E. Newbury, J. Mat. Sci. 15 (1980), 2073.

[Hon80b] J. D. Hong, R. F. Davis, J. Am. Ceram. Soc. 63 (1980), 546.

[Hon81] J. D. Hong, R. F. Davis, D. E. Newbury, J. Mat. Sci. 16 (1981), 2485.

[Hon92] J. W. Hong, Y. W. Chen, K. C. Chang, Y. K. Fang, IEEE Trans. Elec. Dev. 39 (1992), 292.

[Hor88] K. M. Horn, W. A. Lanford, Nucl. Instr. Meth. B 34 (1988), 1.

[Ino87] S. Inoue, K. Yoshii, M. Umeno, H. Kawabe, Thin Solid Films 151 (1987), 403.

[Iwa01] Y. Iwamoto, W. Völger, E. Kroke, R. Riedel, T. Saitou, K. Matsunaga, J. Am. Ceram. Soc. 84 (2001), 2170.

[Jac92] W. B. Jackson, C. C. Tsai, Phys. Rev. B 45 (1992), 6564.

[Jan97] M. Jansen, Sol. State Ion. 101 (1997), 1.

[Jan01a] M. S. Janson, A. Hallen, M. K. Linnarsson, B. G. Svensson, Phys. Rev. B 64 (2001), 195202.

[Jan01b] M. S. Janson, A. Hallen, M. K. Linnarsson, B. G. Svensson, Apl. Surf. Sci. 184 (2001), 257.

[Jan05] N. Janakiraman, A. Zern, M. Weinmann, F. Aldinger, P. Singh, J. Europ. Ceram. Soc. 25 (2005), 509.

[Joh39] W. A. Johnson, R. Mehl, Trans. AIME 135 (1939), 416.

[Jus02] J. F. Justo, C. R. S. Silva, Diff. Def. Forum 206 (2002), 19.

[Kak83] H. Kakinuma, S. Nishikawa, T. Watanabe, K. Nihei, Jap. J. Appl. Phys. 22 (1983), L801.

[Kan87] J. Kanicki, P. Wagner, Electrochem. Soc. Proc. 67 (1987), 261.

[Kau95] I. Knaur, Y. Mishin, W. Gust, *Fundamentals of Grain and Interphase Boundary Diffusion*, (Wiley, Chichester, 1995).

[Kem93] M. Kemp, H. M. Branz, Phys. Rev. B, 47 (1993), 7067.

[Kem02] A. T. W. Kempen, F. Sommer, E. J. Mittemeijer, J. Mater. Sci. 37 (2002), 1321.

[Kha89] P. K. Khabibullaev, B. G. Skorodumov, *Determination of Hydrogen in Materials* (Springer, Berlin, 1989).

[Kij76] K. Kijima, S. Shirasaki, J. Chem. Phys. 65 (1976), 2668.

[Kim98] J. H. Kim, K.W. Chung, J. Appl. Phys. 83 (1998), 5831.

[Kir85] R. Kirchheim, U. Stolz, J. Non-Cryst. Sol. 70 (1985), 323.

[Kir82] R. Kirchheim, Acta Metall. 30 (1982), 1069.

[Klu74] H. P. Klug, L. E. Alexander, *X-ray Procedures for Polycrystalline and Amorphous Materials* (Wiley, New York, 1974).

[Koi74] M. Koiwa, Acta Metall. 22 (1974), 1259.

[Kol37] A. N. Kolmogorov, Isz. Akad. Nauk SSR, Ser. Fiz. 3 (1937), 355.

[Kom90] S. Komateu, Y. Hirobata, S. Fukuda, T. Hino, T. Yamashina, T. Hata, K. Kuskabe, Thin Solid Films 193-194 (1990), 917.

[Kom94] K. Komeya, M. Matsui in: *Materials Science and Technology Vol. 11,* R. W. Cahn, P. Haasen (eds.), (VCH, Weinheim, 1994), p. 545.

[Kra96] W. Kraus, G. Nolze, J. Appl. Cryst. 29 (1996), 301.

[Kro00] E. Kroke, Y. L. Li, C. Konetschny, E. Lecomte, C. Fasel, R. Riedel, Mat. Sci. Eng. R26 (2000), 97.

[Kru98] D. Kruangam, T. Sujaridchai, K. Chirakawikul, B. Ratwises, S. Panyakeow, J. Non-Cryst. Sol. 227-230 (1998), 1146.

[Kum04] N. V. R. Kumar, R. Mager, Y. Cai, A. Zimmemann, F. Aldinger, Scr. Mater. 51(2004), 65.

[Kun88] K. P. Kunz, K. Sarin, R. F. Davis, S. R. Bryan, Mat. Sci. Eng. A 105-106 (1988), 47.

[Kur99] D. Kurtenbach, B. S. Mitchell, H. Zhang, M. Ade, E. Müller, Thermochim. Acta 337 (1999), 155.

[Lan78] W. A. Lanford, Nucl. Instr. Meth. 149 (1978), 1.

[Lan98] *Diffusion in Semiconductors and Non-Metallic Solids*, Landolt-Börnstein New Series, Vol. III/33 (Springer-Verlag, Berlin, 1998).

[Lav04] G. Lavareda, C. Nunes de Carvalho, E. Fortunato, A. Amaral, A. R. Ramos, J. Non-Cryst. Sol. 338-340 (2004), 797.

[Lee96] J. W. Lee, W. Y. Cho, K. S. Lim, SID Int. Symp. (1996), 489.

[Li92] Y. Li, A. Catalano, B. F. Fieselmann, Mat. Res. Soc. Symp. Proc. 258 (1992), 923.

[Lie01] L. A. Liew, W. Zhang, L. An, S. Shah, R. Luo, Y. Liu, T. Cross, M. L. Dunn, V. Bright, J. W. Daily, R. Raj, Am. Cer. Soc. Bull. 80 (2001), 25.

[Lif61] I. M. Lifshitz, V. V. Slyozov, Phys. Chem. Solids 19 (1961), 35.

[Lik99] F. Link, *Untersuchungen zur Phasenbildung mittels Ionenimplantation im Si-C-N-System,* doctoral thesis, (Universität Frankfurt, Germany, 1999).

[Lin97] D. Y. Lin, C. F. Li, Y. S. Huang, Y. C. Jong, Y. F. Chen, L. C. Chen, C. K. Chen, K. H. Chen, D. M. Bhusari, Phys. Rev. B 56 (1997), 6498.

[Lin99] M. K. Linnarsson, M. S. Janson, S. Karlson, A. Schöner, N. Nordell, B. G. Svensson, Mat. Sci. Eng. B 61 (1999), 275.

[Lin04] M. K. Linnarsson, M. S. Janson, J. Zhang, E. Janzen, B. G. Svensson, J. Appl. Phys. 95, (2004), 8469.

[Loe98] H. P. Löbel, M. Huppertz, Thin Solid Films 317 (1998), 153.

[Loe03] J. Löffler, Intermetallics 11 (2003), 529.

[Lus89] N. Lustig, J. Kanicki, J. Appl. Phys. 65 (1989), 3951.

[Lut98] H. Lutz, M. Bruns, F. Link, H. Baumann, Thin Solid Films 332 (1998), 230.

[Lut01] H. Lutz, *Untersuchungen zur Herstellung und Charakterisierung von Siliciumcarbonitriden,* doctoral thesis, (Universität Karlsruhe, Germany, 2001).

[Mac98] R. Machorio, E. C. Samano, G. Soto, L. Cota, Appl. Surf. Sci. 127-129 (1998), 564.

[Mah85] A. H. Mahan, B. von Roedern, D. L. Williamson, A. Madan, J. Appl. Phys. 57 (1985), 2717.

[Mas01] K. Matsunaga, Y. Iwamoto, J. Am. Ceram. Soc. 84 (2001), 2213.

[Mat89] Hj. Matzke in: *The Physics and Chemistry of Carbides and Borides*, R. Freer (ed.), (Kluwer, Dordrecht, 1989), p. 365.

[Mat00] S. Matics, W. Frank, J. Non-Crys. Sol. 266-269 (2000), 830.

[Mat01] S. Matics, W. Frank, Diff. Def. Forum. 194-199 (2001), 947.

[Meh90] H. Mehrer (ed.), *Diffusion in Solid Metals and Alloys*, Landolt-Börnstein New Series, Vol. III/26 (Springer-Verlag, Berlin, 1990).

[Mog75] C. J. Mogab, P. M. Petroff, T. T. Sheng, J. Electrochem. Soc. 122 (1975), 815.

[Mue02] E. Müller, A. Hilbig, R. Wenzel, K. Trommer, G. Roewer, O. Sciurova, J. R. Niklas, Adv. Eng. Mat. 4 (2002), 880.

[Mul00] A. Müller, P. Gerstel, M. Weinmann, J. Bill, F. Aldinger, J. Europ. Ceram. Soc. 20 (2000), 2655.

[Mul01] A. Müller, P. Gerstel, M. Weinmann, J. Bill, F. Aldinger, J. Europ. Ceram. Soc. 21 (2001), 2171.

[Mul02a] A. Müller, P. Gerstel, M. Weinmann, J. Bill, F. Aldinger, Chem. Mater. 14 (2002) 3398.

[Mul02b] A. Müller, J. Peng, H. J. Seifert, J. Bill, F. Aldinger, Chem. Mater. 14 (2002), 3406.

[Mul04] A. Müller, P.Gerstel, E. Butchereit, K. G. Nickel, F. Aldinger, J. Europ. Ceram. Soc. 24 (2004), 3409.

[Nat96] H. Natter, T. Krajewski, R. Hempelmann, Ber. Bunsenges. Phys. Chem. 100 (1996), 55.

[Nis83] S. Nishikawa, H. Kakinuma, T. Watanabe, K. Kaminishi, J. Non-cryst. Sol. 59-60 (1983), 1235.

[Ord00] A. Ordine, C. A. Achete, O. R. Mattos, I. C. P. Margarit, S. S. Camargo Jr., T. Hirsch, Surf. Coat. Technol. 133-134 (2000), 532.

[Pal81] H. D. Palfrey, M. Braun, A. F. W. Willoughby, J. Electrochem. Soc. 128 (1981), 2224.

[Pal93] E. C. Paloura, A. Knop, K. Holldack, U. Döbler, S. Logothetidis, J. Appl. Phys. 73 (1993), 2995.

[Par03] N.-M. Park, S. H. Kim, G. Y. Sung, J. Appl. Phys. 94 (2003), 2725.

[Pat02] S. K. Patra, G. Mohan Rao, Mat. Sci. Eng. B 90 (2002), 90.

[Pat03] S. B. Patil, A. A. Kumbhar, S. Saraseat, R. O. Dusane, Thin Solid Films 430 (2003), 257.

[Pea91] J. Pearton, W. Corbett, M. Stavola, *Hydrogen in Crystalline Semiconductors,* (Springer, Berlin, 1991), 210.

[Pen02] J. Peng, *Thermochemistry and Constitution of Precursor-derived Si-B-C-N Ceramics*, doctoral thesis, (Universität Stuttgart, Germany, 2002).

[Pen03] X. Peng, X. Hu, W. Wang, L. Song, Jpn. J. Appl. Phys. 42 (2003), 620.

[Phi91] J. Philibert, *Atom Movements*, (Les Editions de Physique, Les Ulis, 1991).

[Pla95] R. Platz, D. Fischer, A. Shah, Mat. Res. Soc. Symp. Proc. 258 (1995), 645.

[Pow88] J. A. Powell, L. G. Matus, in: *Springer Proceedings in Physics Vol. 34: Amorphous and Crystalline Silicon Carbide,* G. L. Harris, C. Y.-W. Yang (eds.) (Springer, Berlin, 1988), 2.

[Raj98] R. Raj, L. An, S. Shah, R. Riedel, C. Fasel, H. J. Kleebe, J. Am. Ceram. Soc. 81 (1998), 1803.

[Ram01] P. A. Ramakrishnan, Y. T. Wang, D. Balzar, C. Haluschka, R. Riedel, A. M. Herrmann, Appl. Phys. Lett. 78 (2001), 3076.

[Rea96] L. S. Rea, Mat. Res. Soc. Symp. Proc. 423 (1996), 3.

[Rei98] R. Reitano, P. Baeri, Europhys. Lett. 43 (1998), 565.

[Rei03] K. J. Reichle, *Thermische Entwicklung atomarer freier Volumen und Kristallisation in Si-(B-)C-N Precursor-Keramiken*, doctoral thesis (Universität Stuttgart, Germany, 2003).

[Ric03] C. Ricciardi, G. Fanchini, P. Mandracci, Diamond Rel. Mat. 12 (2003), 1236.

[Rie92] R. Riedel, G. Passing, H. Schönfelder, R. J. Brook, Nature 355 (1992), 714.

[Rie96] R. Riedel, A. Kienzle, W. Dressler, L. Ruwisch, J. Bill, F. Aldinger, Nature 382 (1996), 796.

[Rie97] Riedel, A. Greiner, G. Miehe, W. Dreßler, H. Fueß, J. Bill, F. Aldinger, Angew. Chem. 109 (1997), 657.

[Rie98] R. Riedel, L. Ruwisch, L. An, R. Raj, J. Am. Ceram. Soc., 81 (1998), 3341.

[Ril00] F. L. Riley, J. Am. Ceram. Soc. 83 (2000), 245.

[Riv98] J.–P. Riviere, J. Delafond, P. Misaelides, F. Noli, Surf. Coat. Technol. 100-101 (1998), 243.

[Rob91] J. Robertson, Appl. Phys. Lett. 59 (1991), 3425.

[Rob94] J. Robertson, Phil. Mag. A 69 (1994), 307.

[Rol74] C. Rolfs, W. S. Rodney, Nucl. Phys. A 325 (1974), 450.

[Rus01] K. Rüschenschmidt, H. Bracht, M. Laube, N. A. Stolwijk, G. Pensel, Physica B 308-310 (2001), 734.

[Rus04] K. Rüschenschmidt, H. Bracht, N. A. Stolwijk, M. Laube, G. Pensl, G. R. Brandes, J. Appl. Phys. 96 (2004), 1458.

[Rys86] H. Ryssel, I. Ruge, *Ion Implantation,* (Wiley, Chichester, 1986).

[Sal02] R. Saleh, L. Munisa, W. Beyer, L. Non-Cryst. Solids 299-302 (2002), 891.

[San84] J. M. Sanz, Surf. Interface Anal. 6 (1984), 196.

[Sce98] S. Schempp, J. Dürr, P. Lamparter, J. Bill, F. Aldinger, Z. Naturforsch. 53 A, 127 (1998).

[Sch18] P. Scherrer, Göttinger. Nachr. Math. Phys., 2 (1918), 98.

[Sch94] K. A. Schwetz in: *The Encyclopedia of Advanced Materials,* D. Bloor (ed.) (Pergamon-Elsevier, Oxford, 1994), p. 2455.

[Sch00] H. Schmidt, G. Borchardt, S. Weber, S. Scherrer, H. Baumann, A. Müller, J. Bill, J. Appl. Phys. 88 (2000), 1827.

[Sch01] H. Schmidt, G. Borchardt, H. Baumann, S. Weber, S. Scherrer, A. Müller, J. Bill, Def. Diff. For. 194-199 (2001), 941.

[Sch02a] H. Schmidt, G. Borchardt, S. Weber, H. Scherrer, H. Baumann, A. Müller, J. Bill, J. Non-Cryst. Solids 298 (2002), 232.

[Sch02b] H. Schmidt, W. Gruber, G. Borchardt, H. Baumann, A. Müller, J. Bill in: *Proceedings of the VIII. Seminar on Diffusion and Thermodynamics of Materials*, J. Cermak, J. Vrest'al (eds.) (Masaryk University, Brno, 2002), 131.

[Sch03] H. Schmidt, G. Borchardt, C. Schmalzried, R. Telle, S. Weber, H. Scherrer, J. Appl. Phys. 93 (2003), 907.

[Sch04a] H. Schmidt, W. Gruber, G. Borchardt, M. Bruns, M. Rudolphi, H. Baumann, Thin Solid Films 450 (2004), 344.

[Sch04b] H. Schmidt, G. Borchardt, A. Müller, J. Bill, J. Non-Cryst. Solids 341 (2004), 133.

[Sch05a] H. Schmidt, G. Borchardt, Adv. Eng. Mat. 7 (2005), 221.

[Sch05b] H. Schmidt, W. Gruber, G. Borchardt, P. Gerstel, A. Müller, N. Bunjes, J. Europ. Ceram. Soc. 25 (2005), 227.

[Sch05c] H. Schmidt, E. R. Fotsing, G. Borchardt, R. Chassagnon, S. Chevalier, M. Bruns, Appl. Surf. Sci., in print.

[Scu02] J. Schuhmacher, F. Berger, M. Weinmann, J. Bill, F. Aldinger, K. Müller, Appl. Org. Met. Chem. 15 (2001), 1.

[See68] A. Seeger, K. P. Chik, Phys. Stat. Sol. 29 (1968), 455.

[See71] A. Seeger, Rad. Effects 9 (1971), 15.

[Seh94] M. Seher, J. Bill, F. Aldinger, R. Riedel, J. Cryst. Growth 137 (1994), 452.

[Sei84] T. Seikawa, A. Okamoto, J. Electrochem. Soc. 131 (1984), 2928.

[Sei98] H. J. Seifert, H. L. Lukas, F. Aldinger, Ber. Bunsenges. Phys. Chem. 102 (1998), 1309.

[She86] P. G. Shewmon, *Diffusion in Solids* (The Minerals, Metals & Materials Society,Warrendale,U.S.A., 1986).

[Shi99] J. Shinar, R. Shinar, D. L. Williamson, S. Mitra, H. Kavak, V. L. Dalal, Phys. Rev. B 60 (1999), 15875.

[Sil97] J. P. Silvermann, J. Vac. Sci. Technol. B 15 (1997), 2117.

[Spa77] F. Spaepen, Acta. Met 25 (1977), 507.

[Spe96] J. Speakman, P. Rose, J. A. Hunt, N. Cowlam, R. E. Somekh, A l. Greer, J. Mag. Mag. Mat. 156 (1996), 411.

[Spi98] C. Spinella, S. Lombardo, F. Priolo, J. Appl. Phys. 84 (1998), 5383.

[Sta99] B. Stannowski, H. Meiling, A. M. Brockdorf, R. E. I. Schropp, Mater. Res. Soc. Symp. Proc. 557 (1999), 659.

[Ste94] F. C. Stedile, I. J. R. Baumvol, W. H. Schreiner, F. L. Freire, Jr., J. Vac. Sci. Technol. A 12 (1994), 462.

[Str87] R. A. Street, C. C. Tsai, J. Kakalios, W. B. Jackson, Phil. Mag. B 56 (1987), 305.

[Str91] R. A. Street, Physica B 170 (1991), 69.

[Tan85] T. Y. Tan, U. Goesele, Appl. Phys. A37 (1985), 1.

[Tan02] I. Tanaka, K. Tatsumi, M. Nakano, H. Adachi, F. Oba, J. Am. Ceram. Soc. 85 (2002), 68.

[Taw82] Y. Tawada, K. Tsuge, M. Kondo, H. Okamoto, Y. Hamakawa, J. Appl. Phys. 53 (1982), 5273.

[Tes95] J. R. Tesmer, M. Nastasi (eds.), *Handbook of Modern Ion Beam Materials Analysis,* (Materials Research Society, Pittsburgh, Pennsylvania, USA, 1995).

[The99] E. Theodossiu, H. Baumann, K. Bethge, J. Appl. Phys. 86 (1999), 4703.

[The02] E. Theodossiu, H. Baumann, W. Matz, A. Mücklich, Phys. Stat. Sol. 194 (2002), 47.

[Tra02] S. Trassel, M. Puchinger, E. Rössler, G. Ziegler, J. Europ. Ceram. Soc. 23 (2002), 781.

[Tom01] I. Tomaszkiewicz, J. Therm. Anal. Calorim. 65 (2001), 425.

[Urb02] S. Urban, F. Falk, T. Gorelik, U. Kaiser, Mat. Sci. Forum 389-393 (2002), 871.

[Usl96] C. Uslu, B. Park, D. B. Poker, J. Electron. Mater. 25 (1996), 23.

[Van95] C. G. Van de Walle, R. A. Street, Phys. Rev. B 51 (1995) 10615.

[Vic90] J. C. Vickerman, N. M. Reed, A. Brown, *Secondary Ion Mass Spectrometry: Principles and Applications* (Clarendon Press, Oxford, 1990).

[Vil91] P. Villars, L. D. Calvert, *Pearson's Handbook of Crystallographic Data for Intermetallic Phases*, (ASM International, Materials Park, Ohio, 1991).

[Vlc02] J. Vlcek, M. Kormunda, J. Cizek, V. Perina, J. Zemek, Surf. Coat. Tech. 160 (2002), 74.

[Vog77] W. Vogel, *Structure and Crystallization of Glasses* (Pergamon, Oxford, 1977).

[Vos02] T. Voss, A. Strohm, S. Matics, P. Scharwaechter, W. Frank, Zeitschr. Metallk. 93 (2002), 1077.

[Vos03] T. Voss, A. Strohm, W. Frank, Zeitschr. Metallk. 94 (2003), 419.

[Wai58] T. R. Waite, J. Chem. Phys. 28 (1958), 103.

[Wag61] C. Wagner, Z. Elektrochem., 65 (1961) 581.

[Wag01] R. Wagner, R. Kampmann, P. W. Voorhees in: *Phase Transformations in Materials,* G. Kostorz (ed.), (Whiley-VCH, Weinheim, 2001).

[Wah95] Q. Wahab, L. Hultman, I. P. Ivanov, M. Willander, J.-E. Sundgren, J. Mater. Res. 10 (1995), 1349.

[Wak90] F. Wakai, Y. Kodama, S. Sakaguchi, N. Murayama, K. Izaki, K. Niihara, Nature 344 (1990), 421.

[Wan96] L. Wang, L. Hsu, E. E. Haller, J. W. Erickson, A. Fischer, K. Eberl, M. Cardona, Phys. Rev. Lett. 76 (1996), 2347.

[Wan01] Z. Wang, F. Aldinger, R. Riedel, J. Am. Ceram. Soc. 84 (2001), 2179.

[Wei00] M. Weinmann, J. Schumacher, H. Kummer, S. Prinz, J. Peng, H. J. Seifert, M. Christ, K. Müller, J. Bill, F. Aldinger, Chem. Mat. 12 (2000), 623.

[Wei01] M. Weinmann, A. Zern, F. Aldinger, Adv. Mat. 13 (2001), 1704.

[Wel00] M. Wellen, *Diffusion der stabilen Tracerisotope ^{30}Si und ^{74}Ge in der intermetallischen Phase Fe_3Si im Temperaturbereich von 530 bis 720 °C*, doctoral thesis (Technische Universität Clausthal, 2000).

[Wic03] T. Wichmann, J. Bill, F. Aldinger, J. Mayer, G. Müller, U. Schumacher. Z. Metallkd. 94 (2003), 208.

[Wie56] A. Van Wieringen, N. Warmholtz, Physica 22 (1956), 849.

[Wil53] G. K. Williamson, W. H. Hall, Acta Mater. 1 (1953) 22.

[Wu02] X. C. Wu, R. Q. Cai, P. X. Yan, W. M. Liu, J. Tian, Appl. Surf. Sci. 185 (2002), 262.

[Xia00] X. C. Xiao, Y. W. Li, L. X. Song, X. F. Peng, X. F. Hu, Appl. Surf. Sci. 156 (2000), 155.

[Yam83] T. Yamada, T. Kawahito, T. Iwai, J. Mater. Sci. Lett. 2 (1983), 275.

[Yu02] G. C. Yu, S. K. Yen, Appl. Surf. Sci. 201 (2002), 204.

[Zan85] D. Zanotto, P. F. James, J. Non-Cryst. Solids 74 (1985), 373.

[Zeh94] T. Zehoder, A. Blatler, A. Bachli, Thin Solid Films, 24 (1994), 138.

[Zen52] C. Zener in: *Imperfections in Nearly Perfect Crystals,* W. Shockley (ed.), (Wiley, New York, 1952), 289.

[Zie85] J. Ziegler, J. P. Biersack, U. Littmark, *The Stopping and Range of Ions in Solids,* (Pergamon Press, Oxford, 1985).

[Zie99] G. Ziegler, H.-J. Kleebe, G. Motz, H. Müller, S. Traßel, W. Weibelzahl, Mat. Chem. Phys. 61 (1999), 55.

[Zie03] http:\\www.SRIM.org

[Zim02] A. Zimmermann, A. Bauer, M. Christ, Y. Cai, F. Aldinger, Acta Mater. 50 (2002), 1187.

[Zum00] T. Zumkley, V. Naundorf, M.-P. Macht, Z. Metallkd. 91 (2000), 901.

Appendix:

A. Trap-limited Diffusion

For the numerical simulations of the experimental determined diffusion profiles of hydrogen, the theory of trap-limited diffusion is extensively used (see section 6). In this context, the influence of the implantation damage on hydrogen migration is particularly included into the theory. In the present appendix the concepts of the migration of hydrogen atoms in a solid via a trap-limited diffusion mechanism is described and it is adapted to the special experimental conditions of this study. For a fundamental outline of the theory see Refs. [Pea91, Jan01a, Kem93] and the references cited therein.

The easiest way for a small atom like hydrogen to diffuse in a solid is the direct interstitial mechanism [Phi91]. This mechanism is realized in single crystalline silicon, where the diffuser moves between the adjacent atoms of the lattice with a low migration enthalpy, ΔH_m, of several tenths of electron volt [Wie56]. In contrast to self-diffusion, no point defects are necessary for this motion. The basic idea of a trap-limited mechanism is that the motion of interstitial mobile H atoms is strongly connected with the formation of immobile complexes of the form HR_i at trapping centres R_i intrinsic to the solid (e. g. dangling bonds) with the trapping rate k_i, and subsequent dissociation of these complexes with the dissociation rate ν_i, according to

$$H + R_i \leftrightarrow HR_i. \tag{A.1}$$

For the special experimental conditions of this study where implanted deuterium (^2H) is used as a tracer in a hydrogen (^1H) containing solid, the high dose implantation process may produce a damage of the film structure, leading to extended defect areas which act as additional immobile "deep" trapping centres R_e with a trapping rate k_e and a negligible dissociation rate ($\nu_e \approx 0$). The trapping sites resulting from the implantation process are called extrinsic traps and the trapping sites which are already present in the film like dangling bonds are called intrinsic traps, respectively. The very low constant background content of ^2H in the samples (natural isotope ratio: $^2H/^1H = 1.5 \times 10^{-4}$) is neglected. The corresponding set of differential equations is given by

$$\frac{\partial[^jH]}{\partial t} = D_H \frac{\partial^2[^jH]}{\partial x^2} - \sum_i k_i[^jH][R_i] + \sum_i \nu_i[^jHR_i] - k_e[^jH][R_e], \tag{A.2a}$$

$$\frac{\partial[^jHR_i]}{\partial t} = k_i[^jH][R_i] - \nu_i[^jHR_i], \tag{A.2b}$$

$$\frac{\partial[^jHR_e]}{\partial t} = k_e[^jH][R_e], \tag{A.2c}$$

$$\frac{\partial[\mathrm{R_i}]}{\partial t} = -\frac{\partial[^1\mathrm{HR_i}]}{\partial t} - \frac{\partial[^2\mathrm{HR_i}]}{\partial t}, \tag{A.2d}$$

$$\frac{\partial[\mathrm{R_e}]}{\partial t} = -\frac{\partial[^1\mathrm{HR_e}]}{\partial t} - \frac{\partial[^2\mathrm{HR_e}]}{\partial t}, \tag{A.2e}$$

$$[^j\mathrm{H_{tot}}] = [^j\mathrm{H}] + \sum_i [^j\mathrm{HR_i}] + [^j\mathrm{HR_e}] \tag{A.2f}$$

for j = 1 and 2. Here, $[^1\mathrm{H}]$ and $[^2\mathrm{H}]$ are the concentrations of free hydrogen and deuterium, $[^1\mathrm{HR_i}]$ and $[^2\mathrm{HR_i}]$ are the concentrations of hydrogen and deuterium trapped to intrinsic traps of type i, $[^1\mathrm{HR_e}]$ and $[^2\mathrm{HR_e}]$ are the concentrations of hydrogen and deuterium trapped to extrinsic traps, $[\mathrm{R_i}]$ and $[\mathrm{R_e}]$ are the concentrations of open intrinsic and extrinsic trapping sites, $[^j\mathrm{H_{tot}}]$ is the total concentration of a hydrogen isotope (a quantity which can be measured by SIMS), and D_H is the diffusivity of hydrogen. The total concentration of intrinsic traps is given by $[\mathrm{R_{tot}}] = \sum_i [^j\mathrm{HR_i}] + [\mathrm{R_i}]$.

The solution of Eqs. (A.2) with a given set of boundary conditions can in general be accomplished only numerically, as carried out in section 6 for the Si_3N_4 system. For the gas exchange experiments $R_e = 0$ is used. Nevertheless, in some special cases analytical solutions can be found. If only one type of intrinsic traps R is present or active in the system and if in first approximation the influence of the implantation damage on the diffusion process can be neglected $[R_e] \approx 0$ (for justification of that assumption see section 6.3.), an analytical solution of Eqs. (A.2) can be achieved in a limited regime. Under the assumption of local equilibrium in reaction (A.1), which means that the process of complex formation and dissociation is much faster than the spatial concentration change of any of the constituents, the condition $\partial\,[^2\mathrm{HR}]/\partial\, t = 0$ is obtained. If the concentration of open traps is constant in space and time $[\mathrm{R}] = R_0$, we get from Eq. (A.2b)

$$[^2\mathrm{HR}] = \frac{k\ R_0}{\nu}[^2\mathrm{H}]\ . \tag{A.3}$$

Now the differential equations and especially the motion of $^1\mathrm{H}$ and $^2\mathrm{H}$ can be decoupled and Eq. (A.2a) can be simplified to

$$\frac{\partial[^2\mathrm{H_{tot}}]}{\partial t} = D_\mathrm{eff}\,\frac{\partial^2[^2\mathrm{H_{tot}}]}{\partial x^2}\ . \tag{A.4}$$

$[^2\mathrm{H_{tot}}]$ is thus expected to diffuse according to Fick's second law with a constant effective diffusivity

$$D_{\mathrm{eff}} = D_{\mathrm{H}} \frac{1}{1 + k\ R_0/\nu}\ . \tag{A.5}$$

Identical or similar expressions are also obtained in Ref. [Kem93, Koi74, Kir82]. A consequence of Eqs. (A.4) and (A.5) is that the intrinsic hydrogen diffusivity D_{H} cannot be extracted from the measurement data, only an effective value D_{eff}, which might be orders of magnitudes lower compared to D_{H}, depending on the values of ν, k, and R_0. The complex dissociation frequency ν is expected to follow an Arrhenius temperature dependence of the form

$$\nu = \nu_0\ \exp\left(-\frac{\Delta H_d}{k_{\mathrm{B}} T}\right), \tag{A.6}$$

where ΔH_{d} is the dissociation enthalpy of the HR complexes, ν_0 the so called attempt frequency, which is in the same order of magnitude as the Debye frequency of the material and k_{B} is the Boltzmann constant. The trapping rate k is given by [Pea91]

$$k = 4\pi\ R_{\mathrm{c}} D_{\mathrm{H}}\,, \tag{A.7}$$

where R_{c} is the effective capture radius of a trap. In case of $\nu/(k\ \mathrm{R}_0) < 1$, but still for sufficient high dissociation rates (moderate high dissociation limit), the effective diffusivity becomes entirely determined by the trapping/de-trapping process, and follows an Arrhenius behaviour. We obtain from Eqs. (A.5), (A.6), and (A.7)

$$D = \frac{\nu_0}{4\pi\ R_{\mathrm{c}}\ R_0}\ \exp\left(-\frac{\Delta H_{\mathrm{d}}}{k_{\mathrm{B}} T}\right) = D_0\ \exp\left(-\frac{\Delta H^{\mathrm{D}}}{k_{\mathrm{B}} T}\right). \tag{A.8}$$

The effective diffusivity is now determined by the dissociation enthalpy of trapped hydrogen, which is a sum of the binding enthalpy of the HR complexes, ΔH_{b}, and the migration enthalpy of the free hydrogen atoms, ΔH_{m}, $\Delta H^{\mathrm{D}} = \Delta H_{\mathrm{d}} = \Delta H_{\mathrm{b}} + \Delta H_{\mathrm{m}}$.

In contrast, for very high complex dissociation rates ($\nu/(k\ R_0)$) >> 1 we expect from Eq. (A.5) a diffusivity identical to the intrinsic diffusivity in the trap free case $D_{\mathrm{eff}} = D_{\mathrm{H}}$, with a low overall activation enthalpy $\Delta H^{\mathrm{D}} = \Delta H_{\mathrm{m}}$.

It has to be noted that the present model is valid only in case of a high “dilution” of the system, meaning the concentration of hydrogen is low compared to the concentration of traps. For this case, diffusing hydrogen atoms always see not occupied traps.

B. Tables

Table B.1 Activation enthalpies and pre-exponential factors for the diffusion of various elements in amorphous Si-(B)-C-N.

Material	Pre-annealing temperature (°C)	Isotope	ΔH^D (eV)	$\log(D_0/m^2 s^{-1})$
T21	1700	^{15}N	7.2 ± 1.3	0.8 ± 3.3
T21	1700	^{30}Si	5.7 ± 1.0	-3.0 ± 3.0
T21	1700	$^{15}N + ^{30}Si$	5.8 ± 0.6	-2.8 ± 1.5
T21	1700	^{10}B	7.3 ± 1.3	0.2 ± 3.5
VT50	1460 + 1350	^{30}Si	6.2 ± 0.7	-0.6 ± 2.3

Table B.2 Activation enthalpies and pre-exponential factors for the diffusion of ^{30}Si and ^{15}N in amorphous and polycrystalline Si_3N_4. Data where the diffusivities of Si_3N_4 films and Si-C-N ceramics (VT50) were fitted with a unique Arrhenius line for each element separately are marked with an *.

State	Diffuser	ΔH^D (eV)	$\log(D_0/m^2 s^{-1})$
polycrystalline $\alpha + \beta$	N	4.9 ± 0.4	-6.0 ± 1.2
polycrystalline α	N	5.2 ± 0.4	-4.6 ± 1.3
polycrystalline α	N + Si	5.0 ± 0.3	-5.2 ± 0.9
amorphous	N + Si	4.5 ± 1.0	-6.4 ± 3.5
amorphous*	N	4.9 ± 0.5	-5.0 ± 1.9
amorphous*	Si	5.6 ± 0.4	-2.7 ± 1.1
amorphous*	N + Si	5.5 ± 0.3	-2.8 ± 0.8

Table B.3 Pre-annealing parameters and hydrogen concentration as determined by NRRA as well as activation enthalpies and pre-exponential factors of hydrogen diffusion in amorphous Si-C-N based materials.

Material	Pre-annealing parameters	H concentration (at. %)	ΔH^D (eV)	$\log(D_0/m^2s^{-1})$	Method
Si_3N_4	cast	0.2 ± 0.1	3.4 ± 0.2	-3.3 ± 1.4	ion-implantation
Si_3N_4	1000 °C/N_2	0.4 ± 0.1	3.4 ± 0.2	-3.3 ± 1.1	ion-implantation
Si_3N_4	1200 °C/N_2	0.5 ± 0.1	3.5 ± 0.2	-3.0[5] ± 1.4	ion-implantation
Si_3N_4	1000 °C/ N_2-6 % H_2	2.6 ± 0.2	2.7 ± 0.2	-5.5 ± 1.2	ion-implantation
Si_3N_4	1000 °C/ N_2-6 % H_2	2.6 ± 0.2	2.6 ± 0.3	-5.5 ± 1.3	gas exchange
Si_3N_4	1500 °C/ N_2	0.5 ± 0.1	4.0 ± 0.8	-1.8 ± 3.0	ion-implantation
SiC	1000 °C/Ar	0.4 ± 0.1	3.2 ± 0.2	-4.1[5] ± 1.0	ion-implantation
SiC	1000 °C/ N_2-6 % H_2	1.0 ± 0.2	2.6 ± 0.3	-6.1[5] ± 1.5	gas exchange
Si_2CN_4	1000 °C/N_2	0.5 ± 0.1	3.0 ± 0.2	-4.8 ± 1.0	ion implantation
T21	cast	0.2 ± 0.1*	2.2 ± 0.2	-7.5 ± 0.6	gas exchange
T21	cast	-	2.5 ± 0.4	-7.0 ± 1.6	ion implantation
T21	1460 °C/N_2	0.1 ± 0.1	2.2 ± 0.3	-7.5 ± 0.6	gas exchange
T21	1600 °C/N_2	0.2 ± 0.1	2.2 ± 0.3	-6.8[5] ± 0.6	gas exchange
MW33	1460 °C/N_2	0.2 ± 0.1	2.4 ± 0.2	-7.5 ± 1.1	gas exchange
VT50	1460 °C/N_2	0.6 ± 0.1	2.2 ± 0.2	-7.5 ± 0.8	gas exchange
AM26	1000 °C/ N_2-6 % H_2	3.9 ± 0.2	0.3 ± 0.2	-13.4 ± 1.6	gas exchange
$B_{50}N_{28}C_{22}$	1000 °C/ N_2-6 % H_2	2.8 ± 0.2	0.7 ± 0.1	-11.4 ± 1.0	gas exchange
Glassy carbon I	1000 °C/ N_2-6 % H_2	0.2 ± 0.1	0.6[5] ± 0.2	-11.6 ± 1.0	gas exchange
Glassy carbon II	1000 °C/ N_2-6 % H_2	0.2 ± 0.1	1.0 ± 0.2	-10.9 ± 1.0	gas exchange

* The hydrogen concentration given here is a value which remains after desorption from pores (see Sec. 6.3.3).

Table B.4 Typical hydrogen concentration as determined by NRRA for several types of Si-(B-)C-N ceramics as a function of annealing conditions. The annealing time is 2 h.

Material	Annealing temp. (°C)	Atmosphere	H concentration (at.%)
VT50	as-thermolyzed	Ar	5.0 ± 0.3
VT50	900	N_2	1.6 ± 0.2
VT50	1460	N_2	0.8 ± 0.2
T21	as-thermolyzed	Ar	5.5 ± 0.2
T21	900	N_2	0.2 ± 0.1
T21	1460	N_2	0.1 ± 0.1
T21	1600	N_2	0.1 ± 0.1
T21	1700	N_2	0.2 ± 0.1
T21	1800	N_2	0.6 ± 0.1
MW33	as-thermolyzed	Ar	7.0 ± 0.3
MW33	1460	N_2	0.3 ± 0.1
AM26	as-thermolyzed	Ar	2.5 ± 0.2
AM26	800	N_2 / 6% H_2	3.9 ± 0.2
AM26	1460	N_2	0.6 ± 0.2

Table B.5 Activation enthalpies and pre-exponential factors for the rate constants of crystallization in amorphous SiC, Si_3N_4, and Si-C-N.

Material	ΔH^{NG} (eV)	$\log(k_0{}^{NG}\,(s^{-1}))$
SiC/Si	4.1 ± 0.7	8.7 ± 2.5
SiC/gc	8.9 ± 0.9	20.8 ± 3.0
Si_3N_4	5.5 ± 0.5	12.6 ± 1.5
VT50	12.5 ± 1.0	30 ± 2
NCP200	12.8 ± 1.2	31 ± 3

Table B.6 Activation enthalpies and pre-exponential factors for the rate constants of coarsening of SiC in amorphous Si-B-C-N.

Material	ΔH^{C} (eV)	$\log(k_0{}^{C}\,T\,(K\,m^3/s))$
AM26	7.2 ± 0.6	-7.1 ± 1.7
T21	8.4 ± 0.7	-4.1 ± 1.9
MW33	8.3 ± 1.3	-4.8 ± 3.0